Ocean-atmosphere feedbacks in two tropical atmospheric regimes: the inter-tropical convergence zone and the trade winds

Suneil Iyer

A dissertation
submitted in partial fulfillment of the
requirements for the degree of

Doctor of Philosophy

University of Washington

2022

Reading Committee:
Kyla Drushka, Chair
Jim Thomson
Luc Rainville

Program Authorized to Offer Degree:
School of Oceanography

University of Washington

Abstract

Ocean-atmosphere feedbacks in two tropical atmospheric regimes: the inter-tropical convergence zone and the trade winds

Suneil Iyer

Chair of the Supervisory Committee:
Dr. Kyla Drushka
School of Oceanography

Air-sea interactions are a critical component of the global climate system. Despite this, uncertainty remains in our understanding of air-sea interaction across spatial scales, particularly on small scales, which are not observable by remote sensing and often not explicitly represented in models due to computational limitations. This dissertation provides insight into the key processes that drive air-sea interaction in two tropical regions that are important for modulating synoptic to global-scale weather and climate: the inter-tropical convergence zone and the trade winds.

The first chapter uses a series of model experiments based on observations from the rainy eastern tropical Pacific to evaluate the influence of preexisting ocean stratification and tropical rain modes on the upper ocean salinity response to rainfall, a process that modulates how freshwater is incorporated into the ocean structure. Differences in the timing of convective and stratiform components of rain events can modify the duration which surface salinity anomalies persist following rain for over two hours, while strong preexisting stratification can allow near-surface salinity anomalies produced by rain to persist for over seven hours longer compared to when rain falls on a well-mixed ocean. Similar differences in salinity structure can exist at deeper depths of up to 20 m in the mixed layer. This work provides insight into the limitations of using low-resolution satellite rain observations in the context of physical

oceanographic studies and examines a critical component of the global water cycle.

The second and third chapters use observations from surface drifters and autonomous vehicles that measure the atmosphere and near-surface ocean in the tropical Atlantic trade wind region to evaluate the spatial variability of ocean surface waves and bulk air-sea fluxes. While previous research has mostly been limited to areas having particularly strong submesoscale activity, this work provides insight into the spatial variability present in a less energetic region representative of larger areas of the global ocean. Surface current variability in the trade winds influence wave slope and air-sea momentum flux due to changes in the relative wind speed and wave-current interactions. Wave-current interactions specifically modify momentum flux by as much as 10%. Across scales of tens of kilometers, air-sea sensible heat, latent heat, and upward buoyancy fluxes vary by 10, 50, and 10 Wm^{-2}. Sensible heat and upward buoyancy fluxes are significantly influenced by spatial sea surface temperature variability, while latent heat flux variability is primarily driven by changes in the atmosphere. The findings from this work could ultimately be used to guide the development of fully coupled atmosphere-wave-ocean models or quantify the limitations of using lower-resolution remote observations or models.

Collectively, the following work serves to elucidate the physics of the dominant small-scale air-sea processes in two regions of the tropical ocean, quantify the influence of these processes on air-sea interaction and upper-ocean mixing, and suggest hypotheses on the implications of neglecting small-scale processes in regional or global studies of the coupled air-sea system.

TABLE OF CONTENTS

Page

List of Figures iii

List of Tables xi

Introduction 1

Chapter 1: The influence of preexisting stratification and tropical rain modes on the mixed layer salinity response to rainfall 8

1.1 Introduction and Background 9

1.2 Rain modes in the eastern tropical Pacific 14

1.3 Model and validation 15

1.4 Model experiments and evaluation criteria 19

1.5 Salinity response to convective and stratiform rain 24

1.6 Influence of preexisting stratification on the salinity response to rain 27

1.7 Salinity response to predominant rain modes 29

1.8 Discussion and conclusions 32

1.9 Summary and Conclusions 36

Chapter 2: Variations in wave slope and momentum flux from wave-current interactions in the tropical trade winds 37

2.1 Introduction 38

2.2 Methods 47

2.3 Results 54

2.4 Discussion and Conclusions 65

2.5 Conclusions 73

Chapter 3: Small-scale spatial variations of air-sea heat, moisture, and buoyancy fluxes in the tropical trade winds 75

3.1 Introduction 76
3.2 Data 79
3.3 Methods 82
3.4 Results 86
3.5 Discussion and Conclusions 102

Conclusion 111

Bibliography 116

LIST OF FIGURES

Figure Number Page

A (a) Rain rate and wind speed measured by the R/V Roger Revelle, (b) salinity, (c) temperature and (d) 37 cm turbulent kinetic energy dissipation rate (ϵ_{37cm}) during Surface Salinity Profiler (SSP) Deployment 18, September 17, 2016 (Drushka et al., 2019). The shaded grey area denotes the uncertainty in estimates of ϵ_{37cm} as explained by Iyer et al. (2021). The bottom x-axis shows local time. The top axis shows horizontal SSP transect distance. Reproduced from Figure 5 of Iyer and Drushka (2021b). 4

B Same as Figure A for SSP Deployment 15, November 9, 2017. Reproduced from Figure 6 of Iyer and Drushka (2021b). 5

1.1 Observed and modeled rain events in the SPURS-2 region. (a) Shipboard rain rate (black) and wind speed (pink) on September 11, 2016. (b) Central mooring rain rate (black) and wind speed (pink) on October 3, 2016. (c) Salinity observed from the SSP (light) and predicted from GOTM (dark) using the forcing in (a). (d) Salinity observed at the central mooring (light) and predicted from GOTM (dark) from the forcing in (b). (e) Turbulent kinetic energy dissipation rate (ϵ) observed from the SSP (pink with shaded uncertainty limits) and predicted from GOTM (black) at 37 cm depth from the forcing in (a). (f) ϵ observed at the central mooring (pink circles) and predicted from GOTM (black) at 7 m depth from the forcing in (b). Labeled time is in UTC (Local time is UTC-8). 12

1.2 Density difference ($\Delta\rho$) between 6 m and 18 m depth observed by Argo profiling floats between January 2000 and December 2020. Weak stratification is defined as 0.04 $kg\ m^{-3} < \Delta\rho < 0.15\ kg\ m^{-3}$ and strong stratification as $\Delta\rho > 0.15\ kg\ m^{-3}$. Proportion of all profiles, within 5° latitude by 5° longitude bins, with (a) weak stratification; (b) strong stratification. The pink dot denotes the location of the SPURS-2 site. Proportion of profiles from June-November with (c) weak stratification; (d) strong stratification. Proportion of profiles per month and value of $\Delta\rho$ (e) at locations within 2.5°latitude and 2.5°longitude of the SPURS-2 site; (f) at all locations. In the SPURS-2 region, where salinity dominates the density stratification, the 0.04 $kg\ m^{-3}$ and 0.15 $kg\ m^{-3}$ density stratification thresholds are roughly consistent with the 0.05 psu and 0.20 psu salinity stratification thresholds discussed in section 4. . . . 13

1.3 Observed rain rate (grey) in $mm\ hr^{-1}$ at points in time relative to the maximum rain rate for all rain events classified as (a) isolated convective (n = 196), (b) convective with trailing stratiform (n = 76), (c) convective with leading stratiform (n = 31), and (d) convective with leading and trailing stratiform (n = 39). Black lines show the average rain rate at times when at least 25% of values were nonzero. Pink circles show the mean variations in wind speed relative to the average wind speed before the peak rain rate, computed across data within binned time intervals during and after rainfall. From earliest to latest, pink circles represent the mean wind speed immediately before the rain peak, immediately after the rain peak, and during 2 hour intervals following the rain. Green (pink) lines denote idealized rain (wind) forcing prescribed in the GOTM simulations; each idealized mode has a total rain accumulation of 20 mm and a wind speed centered at 5 $m\ s^{-1}$. 16

1.4 Salinity profiles collected with an underway CTD during the October-November 2017 SPURS-2 cruise classified based on the difference between salinity at 6 m (S_{6m}) and 18 m (S_{18m}) depth. Grey lines show profiles classified into (a) well-mixed ($\Delta S < 0.05$ psu, where ΔS is defined as $S_{18m} - S_{6m}$); (b) weakly stratified (0.05 psu $< \Delta S < 0.2$ psu); and (c) strongly stratified ($\Delta S > 0.2$ psu) categories. Black lines show representative profiles used as initial conditions in GOTM experiments. Plotted profiles were adjusted to have a surface salinity of 33 psu to highlight differences in stratification between the classifications. 23

1.5 Level 1 simulations. (a) Wind speed (red) and rain rate prescribed in idealized convective (green) and stratiform (dark blue) GOTM experiments. The x-axis shows time since 0:00. Salinity difference between the (b) convective and (c) stratiform experiment and a no-rain experiment (dS). Pink shading represents when either rain case was fresher than the no-rain case. (d) Salinity difference between the convective and stratiform experiments. Green shading represents when the convective case was fresher and blue shading represents when the stratiform case was fresher. Green (blue) points show the times when dS was maximum for the convective (stratiform) experiment at 0, 5, 10, 15, and 20 m. Contours in (b), (c), and (d) represent 0.10 (dark solid), 0.03 (pink/blue/green dashed), and 0.01 (pink/blue/green solid) psu. 26

1.6 Level 2 experiments: Salinity response to isolated convective rain. (a) Prescribed wind speed for model experiments C-WM (well-mixed), C-WS (weakly stratified), and C-SS (strongly stratified). (b) Salinity difference (dS) between experiment C-WM and a no-rain experiment. Pink shading represents when/where experiment C-WM was fresher, and black shading represents when/where the no-rain experiment was fresher. The solid line shows rain rate (scale on right-hand side). Points show the times of maximum dS. (c),(d) Same as (b), for experiments C-WS and C-SS. Contours in (b), (c), and (d) are 0.10 (dark solid), 0.03 (pink dashed), and 0.01 (pink solid) psu dS contours. 30

1.7 Same as Figure 1.6 for the Level 3 experiments, showing the salinity response to rain on a well-mixed ocean. (a) Prescribed wind speed for model experiments C-WM (light green; isolated convective), LS-WM (blue; convective with leading stratiform), TS-WM (dark green; convective with trailing stratiform), and LTS-WM (purple; convective with leading and trailing stratiform). (b) Salinity difference between experiment C-WM and a no-rain experiment. (c),(d),(e) Same as (b) for experiments TS-WM, LS-WM, and LTS-WM. . . 33

2.1 (a) Expected variation in u_* due to the direct effect of currents, assuming C_D from Large and Pond (1981) (current-relative wind, equation 2); (b) Expected variation in u_* due to wave-current interactions (equations 5,8,9). 46

2.2 Eddy kinetic energy calculated from Copernicus Marine Environment Monitoring Service (CMEMS) satellite sea level anomalies on February 1, 2020. The rectangular box denotes the study area where SWIFTs were deployed and recovered. Inset images picture the two types of SWIFTs deployed during ATOMIC. 48

2.3 (a) Wave spectra observed from v4 SWIFT drifters during both legs of ATOMIC. Energy at individual frequencies was smoothed over a 3-hour time period and in frequency space over 0.059 s^{-1} (grey; n=1156). Colored lines denote average spectra within 1 ms^{-1}-wide wind speed categories. Spectra with a wave direction of $< 0°$or $> 150°$had significant swell input and are excluded. (b) Histograms of significant wave height and wave centroid period from all drifters. (c) Binned scatter plot of wave centroid period vs fitted equilibrium range spectral slope for all drifters. 54

2.4 (a) Drift tracks of all SWIFT drifters during both legs of ATOMIC. Colors represent the component of the current vector aligned with the waves. Histograms of data from all drifters: (b) wind (v3 only), wave, and current direction (note that green-gray indicates overlap of wind and wave directions, dark blue indicates overlap of wind and current directions, light blue-green indicates overlap of wind and wave directions, and dark blue-green indicates overlap of wind, wave, and current directions); (c) current and wave-relative current speed; (d) wind speed 56

2.5 SWIFT observations from Case 1. (a) Drift tracks. Colors represent the component of the current vector aligned with the waves, black quivers represent the current direction, and cyan quivers represent the wave direction. (b) mss vs. wind speed for four SWIFT drifters from 2 Feb 2020 0000 UTC to 5 Feb 2020 0000 UTC during leg 2 of ATOMIC. Lines denote averages in 1 ms^{-1}-wide wind speed bins, separated by the wave-relative current ($Ucos\theta$). Points are colored by the wave-relative current, with point outlines denoting whether $Ucos\theta < 0$ (black) or $Ucos\theta > 0$ (pink). All plotted bins contain a minimum of 10 data points. 58

2.6 SWIFT observations from Case 2, collected from 15 Jan 2020 0800 UTC to 17 Jan 0800 UTC during leg 1 of ATOMIC. (a) Drift tracks. Colors represent the component of the current vector aligned with the waves, black quivers represent the current direction, and cyan quivers represent the wave direction. For clarity, quivers are only plotted every 2 points (hours). (b) Drift tracks. Colors represent near-surface ocean temperature in the top 0.5 m. 60

2.7 Histograms of SWIFT observations from Case 2: (a,e) wind speed, (b,f) wave-relative current, (c,g) mss, and (d,h) ocean temperature for three SWIFT drifters from 15 Jan 2020 0800 UTC to 17 Jan 0800 UTC during leg 1 of ATOMIC. Colors represent categories of the wave-relative current: black denotes wave-opposing currents ($Ucos\theta < 0\ ms^{-1}$; n=69) and pink denotes wave-following currents ($Ucos\theta > 0\ ms^{-1}$; n=77). 61

2.8 Equilibrium u_* and mss versus wind speed for all SWIFT data during both legs of ATOMIC. Lines denote averages in 1 ms^{-1}-wide wind speed bins, colored by the wave-relative current ($Ucos\theta$). Error bars represent 95% confidence intervals around the mean of each bin. Blue shading represents the number of observations near a given wind speed and mss or u_*. All plotted bins contain a minimum of 10 data points. The dotted purple line shows expected values of u_* calculated from the relationship in Large and Pond (1981). 66

2.9 Momentum flux vs. wind speed calculated from (a) equilibrium u_* inferred from wave spectra for all SWIFT data and (b-d) version 3.6 of the COARE algorithm for v4 SWIFT data, during both legs of ATOMIC. COARE 3.6 inputs included (b) observed surface currents and waves, (c) observed surface currents but not waves, and (d) observed waves but not surface currents. Lines denote averages in 1 ms^{-1}-wide wind speed bins, colored by the wave-relative current ($Ucos\theta$). Error bars represent 95% confidence intervals around the mean of each bin. All plotted bins contain a minimum of 10 data points. Grey points represent wind speed and momentum flux observations, smoothed over a 3-hour period. The dotted purple line shows expected values calculated using Equation 1, with u_* determined by the relationship in Large and Pond (1981) and using the mean ρ_a observed by the Ronald H. Brown. 67

3.1 GHRSST-OSTIA satellite SST at 09:00 UTC on Feb 3 2020 near the ATOMIC study area. Cyan and green lines denote SWIFT and Wave Glider tracks during ATOMIC (14 Jan to 11 Feb 2020). 80

3.2 SWIFT observations from 14 Jan 2020 to 11 Feb 2020 during ATOMIC (a) Map of SST (observed at 0.3 m depth) (b) Histograms of nighttime and daytime SST (c) Histograms of nighttime and daytime 0.5 m air temperatures (d) 0.5 m air specific humidity and ocean surface saturation specific humidity (e) Wind speed corrected to 10 m height. 87

3.3 Distance from the SST front vs (a) observed SST, (b) air temperature, (c) sea minus air temperature difference, and (d) wind speed from Wave Glider tracks from 2-6 Feb 2020. Colors denote SST and error bars denote averages and standard deviations within 5 km distance increments. Thin horizontal orange and blue lines represent averages and standard deviations on the warm and cold side of the SST front. (e) SST observed by Wave Glider 245 (pink track) and Wave Glider 247 (green track). The green and pink text denote the starting and ending times of the plotted tracks. Only nighttime data are shown. The SST front is shown by the black line. Orange and blue quivers denote the average wind speed and direction on the warm and cold side of the front. Inset: Front location, Wave Glider tracks, and GHRSST-OSTIA satellite SST observations (corrected for -0.2°C offset) from 4 Feb 2020. . . . 89

3.4 Distance from the SST front vs (a) observed sensible heat flux, (b) "atmosphere variability only" (AV) sensible heat flux, and (c) "ocean variability only" (OV) sensible heat flux. As with Figure 3.3a-d, colors denote SST, error bars denote averages and standard deviations within distance bins, and thin horizontal lines represent averages and standard deviations on the warm and cold side of the SST front. (d) Map of Wave Glider tracks with colors denoting nighttime observed sensible heat flux. Lines, text, and quivers denote the same parameters as in Figure 3.3e. 90

3.5 Same as Figure 3.3 for case study 2 (30 Jan to 2 Feb 2020). GHRSST-OSTIA satellite SST observations in Figure 3.5a are from 1 Feb 2020 and are offset by +0.4°C to match in situ observations. The red line denotes the position of the second (southwestern) SST front. Orange and blue quivers in the northern and southern part of the domain denote the average wind speed and direction on the warm and cold side of the eastern (black) and southwestern (red) front, respectively. Error bars and open circles in panels (a)-(d) represent binned-averages, mean, and standard deviation of the front of the same color in (e). 93

3.6 Same as Figure 3.4 for case study 2 (30 Jan to 2 Feb 2020). The red line denotes the position of the second (southwestern) SST front. Error bars and open circles in panels (a)-(c) represent binned-averages, mean, and standard deviation of the front of the same color in (d). 94

3.7 Time series of hourly average and standard deviation (error bars) of (a) SST, (b) 0.5 m air temperature, (c) sea minus air temperature, (d) ocean surface saturation specific humidity, (e) 0.5 m air specific humidity, (f) ocean minus air specific humidity, and (h) wind speed corrected to 10 m in areas with warm water (SST > 26.4°C; orange) and cold water (SST < 26.4°C; blue) observed by v4 SWIFTs from 15-17 Jan 2020. (g) Map of SST observed by v4 SWIFTs. 96

3.8 Time series of hourly average and standard deviation (error bars) of (a) sensible heat flux, (b) "atmosphere-variability-only" (AV) sensible heat flux, (c) "ocean-variability-only" (OV) sensible heat flux, (d) latent heat flux, (e) AV latent heat flux, (f) OV latent heat flux, (g) upward buoyancy flux, (h) AV upward buoyancy flux, and (i) OV upward buoyancy flux in areas with warm water (SST > 26.4°C; orange) and cold water (SST < 26.4°C; blue) observed by v4 SWIFTs from 15-17 Jan 2020. (j) Map of sensible plus latent heat flux observed by v4 SWIFTs. 97

3.9 Observed SST plotted on a background of GHRSST-OSTIA satellite SST taken midway through each a time period during which a persistent SST gradient was observed on (a) 14-18 Jan 2020, (b) 31 Jan - 2 Feb 2020, and (c) 3-10 Feb 2020. 103

3.10 Change in ocean parameters, atmospheric parameters, and air-sea differences across three persistent gradients during ATOMIC. Contour lines show expected change in (a,b,c) sensible heat flux or (d,e,f) latent heat flux based on values on the x- and y-axes assuming average conditions observed during ATOMIC. Marker shapes indicate gradient number (circle: gradient 2, Jan 14-18; square: gradient 3, Jan 31-Feb 1; diamond: gradient 3 Feb 3-10). Pink error bars denote mean and standard deviations of changes across all of the three time periods. 104

3.11 Change in (a,i) SST, (e) sea surface saturation specific humidity, (b,h) air temperature, (f,k) air specific humidity, (c,g) wind speed, (d,m) air-sea temperature difference, or (h,l) air-sea humidity difference vs. change in air-sea (a,b,c,d) sensible heat, (e,f,g,h) latent heat, and (i,j,k,l,m) upward buoyancy flux across three persistent gradients during ATOMIC. Marker colors denote distance between plotted observations and marker shapes indicate gradient number (circle: gradient 2, Jan 14-18; square: gradient 3, Jan 31-Feb 1; diamond: gradient 3 Feb 3-10). Black error bars denote average and standard deviations of observations within data binned by the property denoted on the x-axis. "R" values shown on the bottom right of represent linear correlation coefficients of property (x-axis) vs. flux (y-axis) for each panel. 105

3.12 Histograms of "ocean variability only" (OV) (a) sensible heat flux, (b) latent heat flux, and (c) upward buoyancy flux in areas with warm SST (> 26.4°C; orange bars) and cold SST (< 26.4°C; blue bars) observed by v4 SWIFTs from 15-17 Jan 2020. (d-f) are the same as (a-c), except using interpolated GHRSST OSTIA Level 4 satellite SST instead of SWIFT observations as inputs into COARE to calculate fluxes. (g) Map of observed SWIFT SST (15-17 Jan 2020) and GHRSST OSTIA Level 4 satellite SST (16 Jan 2020). . 108

C Schematics representing the mixed layer salinity structure following (a) convective with leading stratiform rain, (b) convective with trailing stratiform rain, (c) rain on a well-mixed ocean, and (d) rain on an ocean with preexisting stratification. 112

LIST OF TABLES

Table Number — Page

1.1 Duration (hours:minutes) when significant salinity differences (dS) are observed between GOTM experiments and a no-rain test case at 0 m, 10 m, and 20 m depth. Significant salinity differences were defined with dS thresholds of 0.10 psu at 0 m, 0.03 psu at 10 m, and 0.01 psu at 20 m. No value indicates that dS was always less than the threshold value. A greater-than symbol ($>$) indicates that a significant salinity anomaly was present at the end of the 24-hour model simulation, i.e., the anomaly would have persisted longer if the model was run for longer than 24 hours. 25

1.2 Time, relative to the center of the rain event, of maximum dS at each given depth in GOTM experiments 27

2.1 Mean observed and expected momentum flux (τ, in Nm^{-2}) within wind speed bins, as shown in Figure 2.9a and Figure 2.9c. "Current effect" refers to the percent difference between mean values of τ in the $Ucos\theta < 0$ vs $Ucos\theta > 0.2$ ms^{-1} wave-relative current bins 72

ACKNOWLEDGMENTS

I would first like to acknowledge my adviser, Kyla Drushka for mentorship, advice, and support during my time at the University of Washington. I'm especially grateful for the time we spent out in the field, our many discussions of methods and results, and the countless hours of working through drafts of my papers. Because of these experiences and discussions, I've learned and grown a lot as a researcher over the past six years. I also greatly appreciate Elizabeth Thompson, Jim Thomson, and Luc Rainville for insightful discussions and significant contributions to parts of this dissertation as well as my committee members, Kyla, Jim, Luc, Steve Riser, Mark Warner, and Shuyi Chen, for always ensuring that I maintained good progress. In addition to my committee members, I appreciate all of the faculty, staff, and students at the UW School of Oceanography and Applied Physics Laboratory who I've had conversations with over the past six years and would like to give a special mention to the Physical Oceanography graduate students, 2016 Oceanography graduate cohort, Environmental Fluid Mechanics group, and (Sub)mesoscale Group for their support. Finally, I wish to acknowledge my parents, Ram and Linda Iyer, and my brother, Eswar Iyer, for their continued encouragement and support.

The work in this dissertation would not have been possible without funding from National Science Foundation (NSF) grant OCE-1458759, National Aeronautics and Space Administration (NASA) grants NNX15AF68G and 80NSSC18K1499, and National Oceanic and Atmospheric Administration (NOAA) Climate Program Office (CPO) Climate Variability & Predictability (CVP) Award NA19OAR4310374.

INTRODUCTION

A comprehensive understanding of the transfer of heat, moisture, freshwater, buoyancy, and momentum between the atmosphere and the ocean is crucial for understanding the global climate system. These atmosphere-ocean interactions are a driving force behind creating synoptic to basin-scale weather and climate patterns, which have relevance to human activities on both short and longer timescales. Near-surface ocean properties, which are directly influenced by atmospheric forcing, can also provide insight into long-term climate variability (Pierce et al., 2012; Durack, 2015). Most existing parameterizations of air-sea interactions were developed using observations from the Coupled Ocean Atmosphere Response Experiment (COARE), which included shipboard observations and moorings spaced hundreds of kilometers apart (Webster and Lukas, 1992; Fairall et al., 1996). While refinements to these parameterizations have been made in more recent years (Fairall et al., 2003; Edson et al., 2013), uncertainty remains in our understanding of air-sea interaction primarily on relatively short temporal scales of hours and spatial scales of tens of kilometers and smaller. As higher-resolution climate models which resolve some mesoscale features have been shown to perform better than lower-resolution models (Seo et al., 2006; Bryan et al., 2010; Small et al., 2014; Su et al., 2018), gaining a better understanding of even smaller-scale processes is critically important. This dissertation uses a 1-dimensional ocean model and a unique suite of in situ observations to gain insight into the dominant physical processes that control air-sea interaction and near-surface ocean dynamics on short temporal and small spatial scales in two areas of the tropical ocean with distinct atmospheric regimes.

Rain impacts on stratification and mixing in the inter-tropical convergence zone

Chapter 1 of this dissertation (Iyer and Drushka, 2021a) examines the salinity response to rainfall in the eastern Pacific inter-tropical convergence zone (ITCZ). The ITCZ is characterized by weak winds and frequent intermittent rain events which transfer freshwater from the atmosphere to the ocean and create transient near-surface salinity anomalies (Drushka et al., 2019; Iyer and Drushka, 2021b) and barrier layers (Bingham et al., 2020; Katsura and Sprintall, 2020; Katsura et al., 2021). Eventually, these salinity anomalies are mixed into the upper ocean and create large-scale regions with low near-surface salinity, such as the Eastern Pacific Fresh Pool. Because salinity can be used as a proxy for changes in the global water cycle (Boyer et al., 2005; Durack et al., 2012; Durack, 2015), understanding the link between rain events, which can occur on spatial scales of under tens of kilometers, and larger-scale regions of low salinity that ultimately result from rainfall is critically important.

The second Salinity Processes in the Upper Ocean Regional Study (SPURS-2) consisted of two research cruises in 2016 and 2017 to the eastern tropical Pacific with the broad objective of better understanding air-sea interactions in this region of strong precipitation and near-surface stratification. As a precursor to the research presented in Chapter 1, in situ observations from SPURS-2 presented by Iyer et al. (2021) and Iyer and Drushka (2021b) demonstrated that wind speed was the dominant control of the persistence of fresh anomalies following rain through near-surface turbulent mixing. Figure A shows salinity, temperature, and near-surface turbulence during and after multiple rain events: because wind speeds were generally low ($< 5\ ms^{-1}$), stratification from rain suppressed near-surface turbulent kinetic energy dissipation rates ($< 10^{-5}\ m^2 s^{-3}$) and low salinity water to remain near the surface even when rainfall was weak or zero. However, because the influence of wind speed was dominant, high wind speeds ($> 7\ ms^{-1}$) during and after rainfall elevated near-surface turbulence and prevented freshwater anomalies from forming (Figure B). These results are generally consistent with other previous studies that have looked at the influence of

atmospheric variables (e.g., Drushka et al., 2016; Thompson et al., 2019b) and stratification (e.g., Smyth et al., 1997; ten Doeschate et al., 2019) in other regions in situ. While these findings do provide significant insight into the mixing of freshwater following rain, in situ observations are highly variable making it difficult to isolate the influence of individual processes, such as patterns of rainfall and stratification, responsible for these dynamics.

The limitations of the aforementioned and other in situ observations served as motivation for the research presented in Chapter 1: to gain a more systematic understanding of the physics controlling how freshwater from rain is mixed into the upper ocean in the eastern Pacific ITCZ. A first objective is to make connections between the patterns of rainfall produced by atmospheric convection and larger-scale dynamics and the salinity response to rain. To do this, observations of rainfall are synthesized with the characteristics of convective and stratiform rain presented by previous studies (e.g., Tokay and Short, 1996; Parker and Johnson, 2000; Schumacher and Johnson, 2005; Thompson et al., 2015) to identify the predominant atmospheric modes of rain in the region. Representative idealized rain modes are prescribed as initial conditions in the General Ocean Turbulence Model (GOTM), a 1-dimensional atmosphere-forced ocean model. The modeled salinity response to rain is then compared between different rain modes to determine the dominant modes responsible for near-surface salinity anomalies in the region. A second related objective is to evaluate the influence of preexisting upper ocean stratification on the salinity response to rainfall, as stratification has not been considered in most previous predictions of the salinity response to rainfall (e.g., Santos-Garcia et al., 2014). Because upper ocean stratification is frequent in the ITCZ, rain commonly falls over both a stratified and a well-mixed surface layer. Prescribing stratification based on observed profiles from SPURS-2 as initial conditions in GOTM allows for comparisons to be made between the salinity response to rain under different conditions of preexisting stratification. Collectively, these two series of model experiments provide insight into the influence of two variables which have not previously been analyzed in the context of the mixing of freshwater following rain and provide a more complete understanding of the processes that modulate the transfer of freshwater from the atmosphere to the larger-scale

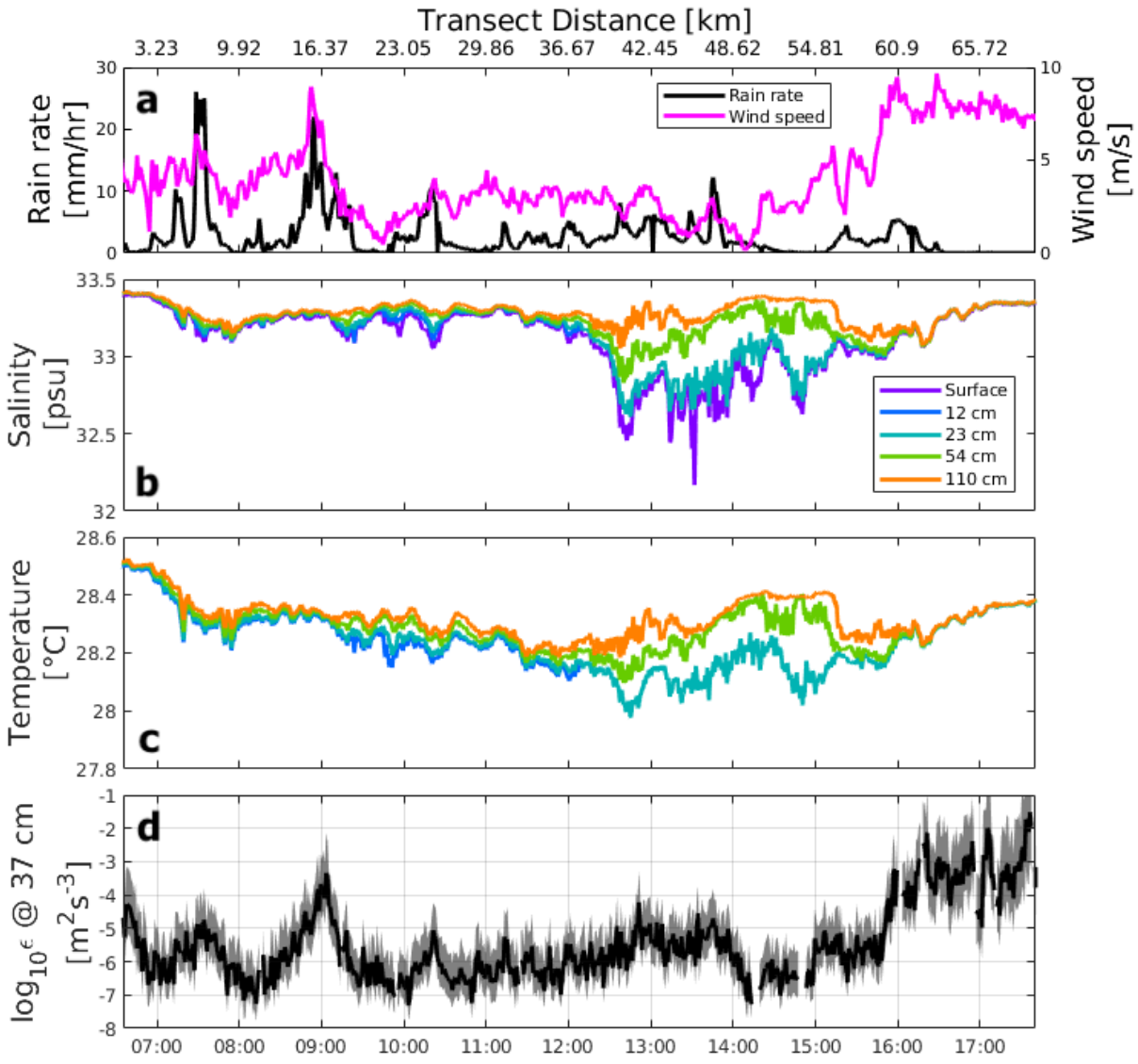

Figure A: (a) Rain rate and wind speed measured by the R/V Roger Revelle, (b) salinity, (c) temperature and (d) 37 cm turbulent kinetic energy dissipation rate (ϵ_{37cm}) during Surface Salinity Profiler (SSP) Deployment 18, September 17, 2016 (Drushka et al., 2019). The shaded grey area denotes the uncertainty in estimates of ϵ_{37cm} as explained by Iyer et al. (2021). The bottom x-axis shows local time. The top axis shows horizontal SSP transect distance. Reproduced from Figure 5 of Iyer and Drushka (2021b).

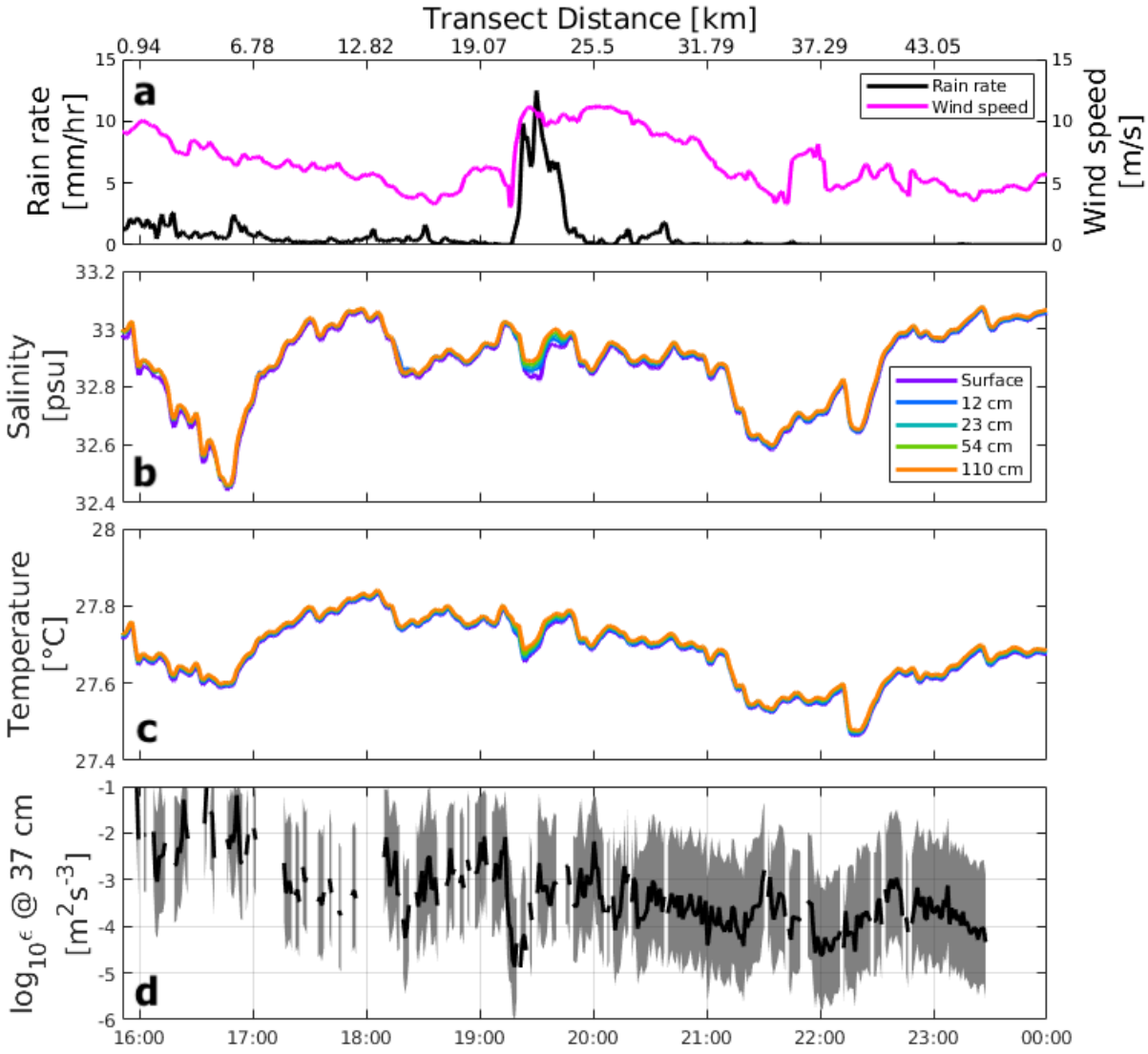

Figure B: Same as Figure A for SSP Deployment 15, November 9, 2017. Reproduced from Figure 6 of Iyer and Drushka (2021b).

salinity structure.

Spatial variability of air-sea interaction in the tropical trade winds

Chapters 2 (Iyer et al., 2022) and 3 examine air-sea interaction in a different regime of the tropics: the trade wind region of the northwestern tropical Atlantic. Rain and wind are highly variable and play a first-order role in modulating the spatial and temporal variability in ocean properties in the ITCZ. The trade wind region, stretching from the ITCZ to 30°north and south, is instead characterized by infrequent rainfall and relatively invariant easterly winds, resulting in minimal near-surface salinity stratification and a deeper mixed layer. Ocean structure in the trade winds is instead influenced by eddies and submesoscale features, which are present throughout much of the world ocean. In the northwest tropical Atlantic, submesoscale and mesoscale activity is ultimately generated by the North Brazil Current (Fratantoni and Glickson, 2002; Ffield, 2005; Fratantoni and Richardson, 2006) and outflow from the Amazon and Orinoco Rivers (Coles et al., 2013). Understanding air-sea interaction in this region, particularly at small scales that are not resolved by satellite observations or incorporated into global-scale models, is critically important because the trade wind region is an important source of synoptic-scale weather and climate phenomena including tropical cyclones and modulates teleconnections between lower and higher latitudes including the El Nino Southern Oscillation (ENSO) and the Pacific Decadal Oscillation (PDO).

The Atlantic Tradewind Ocean-atmosphere Mesoscale Interaction Campaign (ATOMIC) consisted of two research cruises in January-February 2020 and focused on observing small-scale air-sea interaction and atmospheric dynamics in this region. Chapters 2 and 3 utilize observations from Lagrangian Surface Wave Instrument Float with Tracking (SWIFT) drifters (Thomson, 2012) and autonomous Wave Gliders (Hine et al., 2009) deployed as part of ATOMIC. Chapter 2 evaluates the influence of surface ocean current variability on wave slope and momentum flux. In short, parameters derived from wave spectral estimates are compared with theoretical and empirical expectations and across different observed surface current conditions. Previous observations in coastal areas (e.g., Thomson et al., 2014;

Gemmrich and Pawlowicz, 2020) and in the vicinity of western boundary currents (e.g., Holthuijsen and Tolman, 1991; Romero et al., 2017; Hegermiller et al., 2019) demonstrate that wave slopes and momentum flux are elevated when current and wave directions are in opposition due to wave-current interactions, but this effect has not previously been shown in areas of weaker current variability. Furthermore, wave-current interactions are not typically incorporated into model parameterizations including the current version of the COARE bulk flux algorithm (Fairall et al., 1996, 2003; Edson et al., 2013). The research presented in Chapter 2 serves to assess the role of surface current variability in modulating air-sea interaction and demonstrate that non-negligible uncertainty would result from using model parameterizations which do not consider these physical processes.

Chapter 3 examines the spatial variability of air-sea heat, moisture, and buoyancy fluxes near the ATOMIC study site in northwestern tropical Atlantic. Utilizing SWIFT and Wave Glider observations, it was possible to evaluate how air-sea sensible heat, latent heat, and buoyancy fluxes varied across sea surface temperature (SST) gradients on scales of ones to tens of kilometers in the region and determine whether the atmosphere responds to small-scale variability as shown by previous larger-scale observations (e.g., Chelton et al., 2001; Chelton and Xie, 2010) and numerical models (e.g., Samelson et al., 2006; Sullivan et al., 2020). Like the aforementioned previous studies on waves and momentum fluxes, a majority of the work on the co-variability of SST gradients with air-sea heat or moisture flux gradients has been done in areas with strong gradients including boundary currents (e.g., Friehe et al., 1991; Seo, 2017; Shao et al., 2019) and tropical instability waves (e.g., Hayes et al., 1989; Thum et al., 2002; Seo et al., 2007). Because SST frontal activity in the northwestern tropical Atlantic is relatively weak compared to these areas and thus similar to a large percentage of the tropical and subtropical ocean (Figure 1 of Mauzole, 2022), understanding the variability of air-sea fluxes associated with SST fronts in the ATOMIC region provides insight into the importance of small-scale variability in the context of global-scale processes; i.e., whether small-scale variability collectively contributes to larger-scale air-sea interactions and ultimately to global climate.

Chapter 1

THE INFLUENCE OF PREEXISTING STRATIFICATION AND TROPICAL RAIN MODES ON THE MIXED LAYER SALINITY RESPONSE TO RAINFALL

This chapter is published in *Journal of Geophysical Research: Oceans* as **Iyer, S. and K. Drushka, 2021. The influence of preexisting stratification and tropical rain modes on the mixed layer salinity response to rainfall. Journal of Geophysical Research-Oceans 126 (10), e2021JC017574, doi.org/10.1029/2021JC017574**.

Abstract

The freshwater input from rain to the surface ocean is a key component of the global water cycle. Frequent rainfall in the inter-tropical convergence zone creates regions of strong surface stratification and low salinity, which vary seasonally. We evaluate how variations in rain type and preexisting upper ocean stratification influence the timing and duration of the salinity response to rainfall using the General Ocean Turbulence Model (GOTM). A series of model simulations was run by prescribing three typical background stratification conditions and idealized rain and wind forcing that was consistent with observed convective, stratiform, and mixed convective and stratiform rainfall. Background stratification was assessed using underway CTD observations and rain forcing was identified from mooring observations collected in the eastern tropical Pacific during the second Salinity Processes in the Upper Ocean Regional Study (SPURS-2). Model results show that strong stratification, whether preexisting or from convective rainfall, inhibits downward mixing of freshwater and allows near-surface salinity anomalies to persist following rain. In contrast, when stratiform rain precedes convective rain, salinity anomalies are quickly mixed downward and longer lasting

deeper in the mixed layer. This implies that accurately quantifying the salinity structure following rain should consider preexisting stratification and the type of rainfall. Furthermore, patterns of rainfall and stratification likely affect the bias between salinity observations at the surface and deeper in the mixed layer. Because satellite rain data do not correctly represent the small scales of rain forcing, the small-scale surface salinity response to rain cannot be predicted from satellite data.

1.1 Introduction and Background

The inter-tropical convergence zone (ITCZ) is characterized by frequent rain events, which produce intermittent near-surface salinity anomalies (Asher et al., 2014; Walesby et al., 2015; Drushka et al., 2016; Reverdin et al., 2020; Iyer and Drushka, 2021b). The salinity and depth of fresh anomalies vary on timescales of minutes (e.g., Figure 1.1); when winds are high, freshwater mixes downward quickly. Eventually, rainfall creates a region of relatively low near-surface salinity throughout the tropics. It has been shown from large-scale studies that near-surface salinity is correlated with and directly responds to anthropogenic changes in precipitation patterns (Boyer et al., 2005; Durack et al., 2012). Understanding how freshwater from rain is incorporated into the mixed layer may provide insight into the connections between salinity and climate patterns. Here we focus on the short-lived salinity anomalies generated by rainfall, which are an intermediate step between precipitation and the larger-scale ocean structure.

The magnitude and duration of near-surface salinity anomalies depend on rain and wind, so it is probable that different rain modes will produce differing salinity responses. Rain cells in the tropics typically vary in size from roughly 1 to tens of kilometers (Thompson et al., 2019a), depending on the type of rain. Convective rain in the tropics generally occurs as short, small-scale and intense bursts, with rain rates as high as tens to hundreds of $mm\ hr^{-1}$ (Tokay and Short, 1996; Tokay et al., 1999; Thompson et al., 2015). Stratiform rain is less intense and generally lasts for a longer period of time, as individual events cover tens of kilometers or more (Tokay and Short, 1996; Tokay et al., 1999). These characteristics are the

result of dynamical atmospheric differences: convective rainfall is produced by localized convection, while stratiform rain is generated by remote convection and larger-scale atmospheric dynamics. Convective and stratiform rain often occur as part of the same mesoscale convective system (Houze Jr, 2004; Xu and Rutledge, 2014) and are commonly classified based on vertical air velocities, with convective rain events being associated with rapid upward movement. This results in differences in drop size distribution, with larger raindrops observed during stratiform rainfall (Tokay and Short, 1996; Houze Jr, 1997). Patterns of rainfall vary within convective, stratiform, and mixed systems: Rickenbach and Rutledge (1998) found that rainfall in the western tropical Pacific was associated with several modes including linear convective bands, squall lines, and individual cells with small amounts of associated stratiform precipitation. Other studies have also noted considerable differences in the spatial and temporal structure of tropical convective and stratiform rain events (Thompson et al., 2015). Parker and Johnson (2000) and Schumacher and Johnson (2005) investigated the organizational structure of convective and stratiform rain events and determined that several modes of rainfall often exist in mixed systems, depending on wind shear at different altitudes. These include trailing stratiform events, where an area of stratiform precipitation occurs after a leading line of convective rainfall, and leading stratiform events, where stratiform precipitation occurs first. Differences in the patterns of convective and stratiform rain exist, but to our knowledge the connections to the ocean salinity structure have not been studied. Previous studies have determined that salinity stratification is proportional to rain rate (Boutin et al., 2016; Drucker and Riser, 2014; Drushka et al., 2016), but the timing and duration of salinity anomalies following rain has not been a focus. Investigating this issue will provide insight into how regions of low near-surface salinity are created and will improve our understanding of this linkage in the global water cycle.

In addition to atmospheric forcing, stratification greatly influences physical processes in the near-surface ocean: turbulence can be enhanced within and suppressed below stratified layers created by rainfall (Smyth et al., 1997; Walesby et al., 2015; ten Doeschate et al., 2019; Iyer and Drushka, 2021b). Similarly, stratification caused by solar radiation can enhance

near-surface turbulence and intensify surface currents in diurnal warm layers (Brainerd and Gregg, 1993; Callaghan et al., 2014; Sutherland et al., 2016; Moulin et al., 2018). This results from the trapping of momentum in an upper layer, which leads to elevated turbulence levels and faster surface currents in that layer but weaker turbulence below it (Wijesekera et al., 1999; Sutherland et al., 2016). It thus may be important to consider preexisting stratification when investigating the impacts of rainfall on the upper ocean.

We used in situ atmospheric and oceanic observations from the second Salinity Processes in the Upper Ocean Regional Study (SPURS-2) to design 1-D General Ocean Turbulence Model (GOTM) experiments to investigate the influence of different rain modes and preexisting stratification conditions common in the ITCZ on the mixed layer salinity structure. Ship-based radar and in situ observations from SPURS-2, which took place during 2016-2017 in the eastern tropical Pacific Ocean, show significant variations in the patterns of convective and stratiform rain (Rutledge et al., 2019; Thompson et al., 2019a). As a result of rainfall, stratified layers were commonly observed near the surface during the SPURS-2 field campaign (Bingham et al., 2020; Katsura and Sprintall, 2020; Katsura et al., 2021). Hence, a wide-range of preexisting stratification conditions are present in this region (Figure 1.2e). Figure 1.2 shows that SPURS-2 site is representative of typical conditions in the ITCZ and therefore is an ideal location for investigating the effects of varying rain modes and stratification on the salinity response to rain. Initial stratification in GOTM experiments was varied, consistent with observed salinity profiles, in order to evaluate impacts of preexisting stratification. Observed rain and wind conditions were used to construct idealized model experiments that simulated the dominant modes of rainfall in the eastern Pacific ITCZ. Model results were extended by considering the observed regional rain and stratification conditions to identify the primary atmospheric and oceanic factors that influence how freshwater is incorporated into the large-scale salinity structure in the ITCZ.

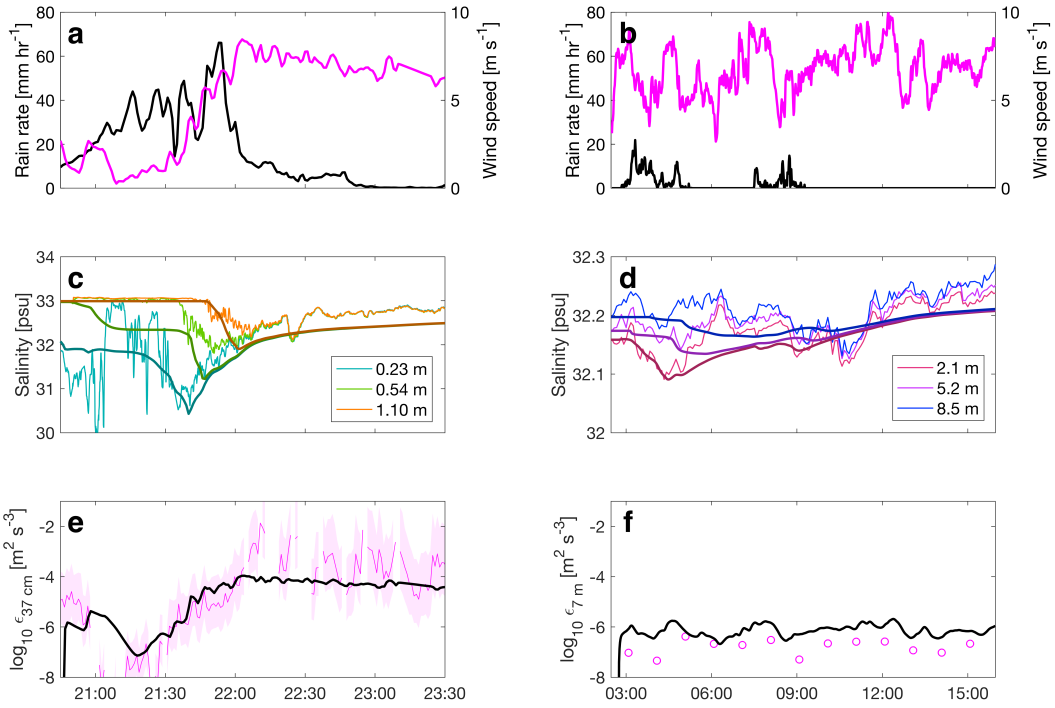

Figure 1.1: Observed and modeled rain events in the SPURS-2 region. (a) Shipboard rain rate (black) and wind speed (pink) on September 11, 2016. (b) Central mooring rain rate (black) and wind speed (pink) on October 3, 2016. (c) Salinity observed from the SSP (light) and predicted from GOTM (dark) using the forcing in (a). (d) Salinity observed at the central mooring (light) and predicted from GOTM (dark) from the forcing in (b). (e) Turbulent kinetic energy dissipation rate (ϵ) observed from the SSP (pink with shaded uncertainty limits) and predicted from GOTM (black) at 37 cm depth from the forcing in (a). (f) ϵ observed at the central mooring (pink circles) and predicted from GOTM (black) at 7 m depth from the forcing in (b). Labeled time is in UTC (Local time is UTC-8).

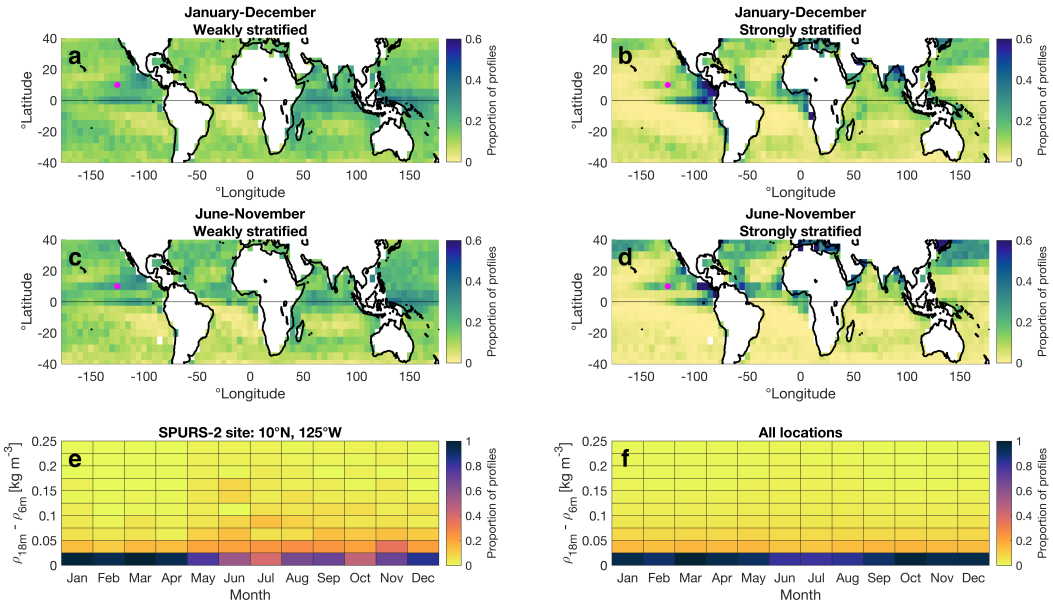

Figure 1.2: Density difference ($\Delta\rho$) between 6 m and 18 m depth observed by Argo profiling floats between January 2000 and December 2020. Weak stratification is defined as 0.04 $kg\ m^{-3} < \Delta\rho < 0.15\ kg\ m^{-3}$ and strong stratification as $\Delta\rho > 0.15\ kg\ m^{-3}$. Proportion of all profiles, within 5° latitude by 5° longitude bins, with (a) weak stratification; (b) strong stratification. The pink dot denotes the location of the SPURS-2 site. Proportion of profiles from June-November with (c) weak stratification; (d) strong stratification. Proportion of profiles per month and value of $\Delta\rho$ (e) at locations within 2.5°latitude and 2.5°longitude of the SPURS-2 site; (f) at all locations. In the SPURS-2 region, where salinity dominates the density stratification, the 0.04 $kg\ m^{-3}$ and 0.15 $kg\ m^{-3}$ density stratification thresholds are roughly consistent with the 0.05 psu and 0.20 psu salinity stratification thresholds discussed in section 4.

1.2 Rain modes in the eastern tropical Pacific

Observations of rain rate and wind speed were made from the SPURS-2 central mooring (10°N, 125°W) using a R.M. Young 5103 Wind Monitor and a R.M. Young 50202 Self-siphoning Rain Gauge between August 2016 and October 2017 (Clayson et al., 2019; Farrar and Plueddemann, 2019; Farrar, 2020). Sensors have specified accuracies of 0.3 ms^{-1} and 1 mm, respectively. One observation was made per minute. Central mooring observations are described in greater detail by Farrar and Plueddemann (Farrar and Plueddemann, 2019). To determine the dominant modes of rainfall, 757 individual rain events were identified as periods of time when rain rates exceeded 0.1 $mm\ hr^{-1}$ before and after 30 minutes without rain. This time spacing was chosen so repeated bursts of rain were classified as a single event. Rain events had a mean accumulation of 5.2 mm with a standard deviation of 11.4 mm. Events were classified into modes based on the presence of high-intensity rain (> 10 $mm\ hr^{-1}$), which is usually observed during convective rainfall (Thompson et al., 2015), and low-intensity rain (< 10 $mm\ hr^{-1}$), which can be observed during convective or stratiform rainfall. Events with a maximum rain rate under 10 $mm\ hr^{-1}$ were classified as stratiform. Events with a maximum rain rate over 10 $mm\ hr^{-1}$ were classified as either isolated convective ("C"; Figure 1.3a), convective with trailing stratiform precipitation ("TS"; Figure 1.3b), convective with leading stratiform precipitation ("LS"; Figure 1.3c), or convective with leading and trailing stratiform precipitation ("LTS"; Figure 1.3d). Events with leading (trailing) stratiform precipitation were identified as having at least 30 minutes of low-intensity rain before (after) the peak in rainfall. An event with fewer than 30 minutes of low-intensity rain before and after high-intensity rain was classified as isolated convective. All of the above categories are mutually exclusive.

This rain rate-based classification scheme is not equivalent to classifying stratiform and convective rain using drop size distributions or radar observations (Tokay and Short, 1996; Tokay et al., 1999; Thompson et al., 2015). Our technique cannot distinguish low-intensity convective rain from stratiform rain or identify periods where convective and stratiform rain

are falling at the same time. In other words, our classification scheme distinguishes rain rates consistent with convective rain from rain rates consistent with stratiform rain, rather than definitively separating the two rain types. Nonetheless, the classification scheme provides insight into the statistics of rainfall at the SPURS-2 study site and informs realistic idealized rain forcing for the model experiments.

The majority (415; 55%) of observed rain events were exclusively stratiform, but these events accounted for little (4%) of the total rain accumulation. C events comprised 26% (196) of rain events, followed by TS (76; 10%), LTS (39; 5%), and LS (31; 4%) rain events. Convective events with leading and/or trailing stratiform rain all contributed significantly to the total freshwater input to the ocean: TS events contributed to 32% of the total rainfall accumulation, followed by LTS (27%) and LS (16%) events. C events accounted for the remaining 21% of the total rain accumulation. We assume that C, LS, TS, and LTS events, which collectively account for 96% of the rain accumulation in this region, will have a dominant influence on the near-surface salinity structure. To investigate the salinity response to rain, we ran model experiments with rain and wind forcing based on these four rain modes.

1.3 Model and validation

GOTM (Burchard et al., 1999; Burchard and Bolding, 2001; Umlauf and Burchard, 2003) is a one-dimensional forced ocean model that has been shown to accurately model variability in ocean temperature (Pimentel et al., 2008), salinity (Drushka et al., 2016), and turbulent kinetic energy (TKE) dissipation rate (ϵ) near the surface (Stips et al., 2002). GOTM uses the Coupled Ocean Atmosphere Response Experiment (COARE) bulk flux algorithm (Fairall et al., 1996; Edson et al., 2013) to calculate air-sea fluxes from specified atmospheric forcing conditions. Individual model experiments were run for 24 hours with a time step of one minute and a minimum spin-up time of one hour before rain was prescribed. A telescoping vertical grid spacing scheme with 500 levels was used to simulate the top 100 m of the ocean. This scheme had a vertical resolution between 0.03 and 0.17 m in the top 20 m.

A second-order turbulence closure scheme with a dynamic k-ϵ TKE equation, dynamic

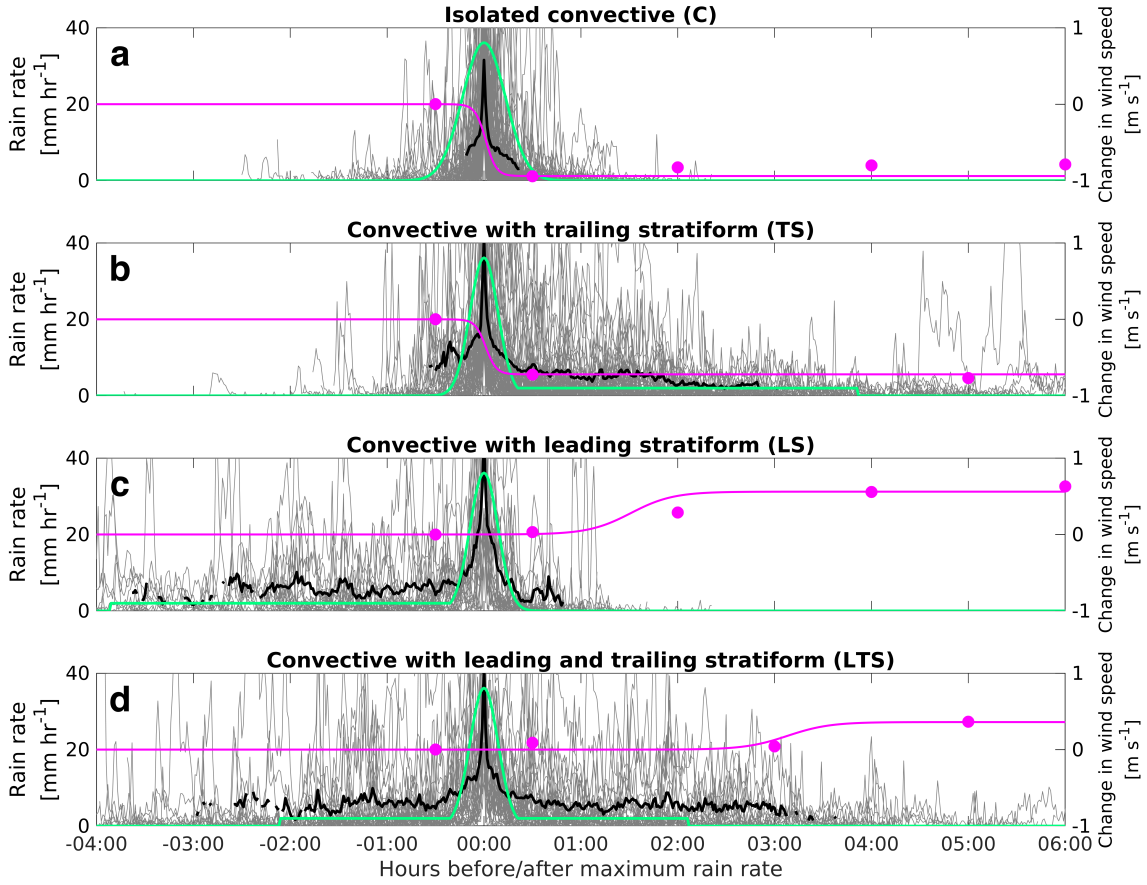

Figure 1.3: Observed rain rate (grey) in $mm\ hr^{-1}$ at points in time relative to the maximum rain rate for all rain events classified as (a) isolated convective (n = 196), (b) convective with trailing stratiform (n = 76), (c) convective with leading stratiform (n = 31), and (d) convective with leading and trailing stratiform (n = 39). Black lines show the average rain rate at times when at least 25% of values were nonzero. Pink circles show the mean variations in wind speed relative to the average wind speed before the peak rain rate, computed across data within binned time intervals during and after rainfall. From earliest to latest, pink circles represent the mean wind speed immediately before the rain peak, immediately after the rain peak, and during 2 hour intervals following the rain. Green (pink) lines denote idealized rain (wind) forcing prescribed in the GOTM simulations; each idealized mode has a total rain accumulation of 20 mm and a wind speed centered at 5 $m\ s^{-1}$.

dissipation rate length scale, and TKE injection surface wave breaking parameterization (Burchard and Bolding, 2001) was used. These model settings are consistent with previous near-surface studies utilizing GOTM (Stips et al., 2002; Pimentel et al., 2008; Jeffery et al., 2010) and identical to those used by Drushka et al. (2016), except without an internal wave breaking parameterization; we found that applying the parameterization of Mellor (1989) overestimated mixing in low-wind conditions. We used the surface wave breaking parameterization of Burchard and Bolding (2001) because ϵ was in better agreement with in situ observations from SPURS-2 in model validation simulations, which are discussed in greater detail in the next section. Modeled ϵ was roughly half of an order of magnitude lower using the surface wave breaking parameterization of Craig and Banner (1994) than the parameterization of Burchard and Bolding (2001). Additional sensitivity tests indicated that modeled salinity and ϵ were otherwise insensitive to the choice of model parameterizations (not shown).

Observations of rain rate, wind speed, atmospheric pressure, and relative humidity from SPURS-2 were used to force the model to validate it for conditions observed in the eastern Pacific ITCZ. The first set of simulations utilized observations from the ship-towed Surface Salinity Profiler (SSP), which measured salinity at 0.12, 0.23, 0.54, and 1.10 m depth and ϵ at 0.37 m depth (Drushka et al., 2019; Iyer et al., 2021; Iyer and Drushka, 2021b). GOTM simulations were forced with rain rate, wind speed, atmospheric pressure, air temperature, and relative humidity observed at the ship available with a one-minute timestamp (Clayson et al., 2019). Figures 1.1a, c, and e compare observations and model output for a large rain event, with an intense convective peak and trailing stratiform rain, sampled with the SSP. Observed and modeled salinities and ϵ in the top meter agree well. Observed and modeled ϵ were almost always consistent within uncertainty limits (uncertainty estimates are described in detail by Iyer et al. (2021)), though observed ϵ appears to exceed modeled ϵ towards the end of the time period when winds are high and salinity stratification is weak. This may be a result of periodic intense wave breaking that is not simulated by the TKE-injection parameterization in GOTM, a potential source of uncertainty near the surface in model sim-

ulations. The maximum modeled salinity difference between 0.23 and 1.10 m after 21:30 was 2.56 psu, while the maximum observed difference was 2.53 psu, an error of 1.2%. The model slightly underestimates salinity at 0.54 and 1.1 m, possibly due to small-scale horizontal processes such as lateral advection that are not resolved by the model; that is, lateral mixing increased salinity in the observations. The second set of model validation simulations used atmospheric and oceanic observations from the SPURS-2 central mooring, which measured salinity at 2.1, 5.2, 8.5, 11 and 14 m (Farrar and Plueddemann, 2019) and ϵ at 7 m (Zippel et al., 2021), during a mixed convective and stratiform rain event (Figures 1.1b, d, and f). During this event, the magnitude of modeled and observed salinity fluctuations within the mixed layer agree well: The maximum observed and modeled salinity differences between 2.1 and 8.5 m are 0.12 and 0.10 psu, respectively, an error of 17%. The error in the salinity gradient between 2.1 and 5.2 m is only 2%. ϵ is generally consistent but elevated in the model compared to the observations (Figure 1.1f). This may be because GOTM underestimates near-surface salinity stratification between 2.1 and 8.5 m by an average of 0.01 psu compared to the observations during the entire period (Figure 1.1d); near-surface stratification is expected to suppress deeper turbulence levels (e.g., Brainerd and Gregg, 1993; Smyth et al., 1997; ten Doeschate et al., 2019; Iyer and Drushka, 2021b). Additional simulations were run by forcing the model with observations from several other SSP and central mooring rain events that had a wider range of wind and rain conditions; these model simulations were also generally consistent with observations (not shown). Furthermore, Drushka et al. (2016) compared GOTM and observed salinities following rain and found no significant fresh or salty bias in the model simulations. Even though rain-induced salinity anomalies are affected by 3-D ocean dynamics (Soloviev et al., 2015) and model parameterizations of wave breaking and turbulence are imperfect, the consistency between modeled and observed salinity and ϵ indicates that 1-D dynamics often dominate the mixing of freshwater following rainfall; hence, GOTM can be used to study this process.

1.4 Model experiments and evaluation criteria

1.4.1 Description of model simulations

A series of idealized model experiments was conducted to investigate the impact of rainfall in the ITCZ on the mixed layer salinity structure. Level 1 model experiments compared the salinity responses of convective and stratiform rain under initially well-mixed stratification conditions (Figure 1.4a). The total accumulation of rain in both experiments was 20 mm. This large total accumulation was prescribed in Level 1 experiments to identify trends in freshwater mixing rather than simulate realistic rain forcing, particularly in the stratiform case: stratiform-only rain events had a maximum total observed accumulation of 9 mm and stratiform components of mixed rain events had a maximum accumulation of 27 mm. Using the same accumulation for both cases allowed for unbiased comparisons between the convective and stratiform simulations. Stratiform rain was simulated by a 10 hour period of constant 2 $mm\ hr^{-1}$ rain, similar to average tropical stratiform rain rates (Tokay et al., 1999) and to those observed during SPURS-2 (mean of 1.5 $mmhr^{-1}$). Convective rain was simulated using a 91 minute long Gaussian pulse with a peak rain rate of 36.1 $mm\ hr^{-1}$, the average peak rain rate of convective and mixed rain events observed from the central mooring during SPURS-2. While observed convective rain was not strictly Gaussian (Figure 1.3a), sensitivity tests indicated that forcing the model with the average rain rate (which has a much more pronounced peak) produces a similar salinity response to idealized Gaussian forcing (not shown). Wind speed was kept steady at 5 $m\ s^{-1}$ to isolate the influence of rain forcing on the salinity structure. Sensitivity tests were run by varying the relative humidity, air temperature, and atmospheric pressure, in addition to prescribing a diurnal cycle in those variables. When the timing of rainfall was varied with respect to the diurnal cycle, freshwater mixed downward faster when rain fell during the night, because of nighttime convection. Air and raindrop temperatures, relative to the ocean temperature, influence near-surface buoyancy and stratification through the air-sea heat flux (Fairall et al., 1996). Sensitivity tests with warmer air temperatures were associated with slightly stronger stratification and

slower downward freshwater propagation. Similarly, cooler air temperatures were associated with faster downward freshwater propagation. However, the difference between the salinity responses of convective and stratiform rain were generally consistent regardless of the timing of rainfall or prescribed air temperature. Modifying the timing or magnitude of relative humidity and atmospheric pressure (within realistic values) had a negligible effect on the salinity response to rain. Prescribing a decrease in air temperature coincident with the rain peak, as often observed during rain events, also did not significantly influence the results. Relative humidity, air temperature, and atmospheric pressure were thus held constant at near the mean observed values during rain in the SPURS-2 region for all experiments. Specifically, 100% relative humidity, 26°C air temperature, and 1013 mb atmospheric pressure, and 100% cloud cover were prescribed. Initially prescribed surface ocean temperature and salinity were consistent with SPURS-2 observations as 28°C and 33 psu.

Level 2 model experiments tested the hypothesis that preexisting stratification has an influence on the near-surface salinity response to rain. Initial salinity and temperature profiles were prescribed based on underway CTD observations made during the SPURS-2 experiment (Sprintall, 2019): well-mixed conditions, when the difference between salinities at 18 m (S_{18m}) and 6 m (S_{6m}) depth ($S_{18m} - S_{6m}$, hereinafter defined as ΔS) was small ($\Delta S < 0.05$ psu), were observed in 46% of 493 profiles made during the October-November 2017 SPURS-2 cruise. Weak salinity stratification in the top 18 m (0.05 psu $< \Delta S < 0.2$ psu) was observed in 32% of the profiles, and strong salinity stratification in the top 18 m ($\Delta S > 0.2$ psu) was observed in 22% of the profiles. These classifications corresponded to halocline depths of roughly > 30 m, 15-25 m, and < 15 m, respectively (Figure 1.4). The ratio of strongly stratified, weakly stratified, and well-mixed underway CTD profiles was generally consistent with Argo observations from 2000-2020 (Figure 1.2): Stratification in the top 20 m is often observed year-round in the tropical ocean (Figure 1.2a), with the strongest stratification most frequently observed in the rainy summer-autumn season (Figure 1.2d). We note that observed stratification in the tropics is not necessarily driven by rainfall: in areas of significant river discharge, such as the Bay of Bengal, near-surface

stratification is generated by fresh river water and varies seasonally with precipitation over land (e.g., Sengupta et al., 2016). Well-mixed conditions are typically observed in the winter and spring and year-round at higher latitudes (Figure 1.2a,b,f). Model experiments with idealized C rain were run three times, each with a representative set of initial salinity and temperature profiles corresponding to one of the three stratification criteria. Representative profiles were chosen to conform to the characteristics of each stratification classification (bold lines in Figure 1.4). A sensitivity test was run by classifying stratification conditions based on density instead of salinity and yielded very similar results. This suggests that density is primarily controlled by salinity in summer-autumn in the SPURS-2 region, and that using a salinity-based scheme is reasonable. As in the Level 1 experiments, C rain was simulated by a 91 minute long Gaussian pulse with a peak rain rate of 36.1 $mm\ hr^{-1}$ (Figure 1.3). Consistent with the Level 1 experiments, a total rain accumulation of 20 mm was prescribed in Level 2 experiments to be representative of large rain events: Rain events with a total accumulation of 20 mm or greater were responsible for 59% of the observed rain accumulation and presumably had the most significant influence on the near-surface salinity structure. We note that forcing and initial conditions are identical in the Level 1 convective experiment and Level 2 experiment with well-mixed conditions, and minor differences result from slight differences in model spin-up time.

Level 3 of the idealized model experiments investigated the salinity response to C, LS, TS, and LTS rain. We did not model exclusively stratiform rain events in the Level 3 experiments since these event only comprised 4% of the total rain accumulation. To isolate the influence of rain, simulations were performed with preexisting well-mixed conditions (the Level 3 experiment with C rain is identical to the well-mixed Level 2 experiment). Rain forcing for mixed convective and stratiform events was prescribed using a combination of a Gaussian pulse preceded and/or followed by a period of constant rainfall, representing leading and/or trailing stratiform rain. These idealized rain forcing conditions were representative of observed average rain conditions for each mode of rainfall (Figure 1.3). As in the other experiments, a total rain accumulation of 20 mm with a peak rain rate of 36.1 $mm\ hr^{-1}$ was

prescribed in each Level 3 experiment. On average, 65% of the rain accumulation observed in LS, TS and LTS rain events was due to convective high intensity ($> 10\ mm\ hr^{-1}$) rain. To reflect this, the width of each Gaussian in LS, TS and LTS experiments was adjusted so the convective (Gaussian) component comprised 65% of the total rain accumulation and the stratiform component (defined as having a constant rate of 2 $mm\ hr^{-1}$) comprised 35% of the total. Idealized rain forcing is shown by the green lines in Figure 1.3.

Figure 1.3 also shows observed and mean variations in wind speed during and after rainfall for individual rain modes. On average, wind speeds were 5.81 $m\ s^{-1}$ with a standard deviation of 2.30 $m\ s^{-1}$ between August 2016 and October 2017 at the central mooring. During rain events, wind speeds had a mean of 5.73 $m\ s^{-1}$ and standard deviation of 2.44 $m\ s^{-1}$. A clear decrease in wind speed was observed following the rain peak during C and TS rain (Figure 1.3a,b), while LS and LTS rain were associated with an increase in wind speed roughly 2 hours after rainfall ended (Figure 1.3c,d). The purpose of the experiments was to investigate the effects of rain on salinity, rather than assess the salinity response over a range of wind speeds, so wind forcing was prescribed in Level 2 and 3 experiments based on average wind conditions observed at the SPURS-2 central mooring during and following rain events. Because wind speeds were variable during rain events, prescribed wind speeds were adjusted from a baseline of 5 $m\ s^{-1}$ using a hyperbolic tangent function to represent increases or decreases in wind speed, which were estimated from mean temporal variations in wind during or immediately after rainfall. For example, the average drop in wind speed after the peak rain rate in TS rain was 0.72 $m\ s^{-1}$, so wind speeds were prescribed as 5.36 $m\ s^{-1}$ before the rain peak and 4.64 $m\ s^{-1}$ after the rain peak (Figure 1.3b). Negligible mean variations in wind speed were observed at other times, so only a single wind change was prescribed for each rain type.

1.4.2 Metrics for evaluating the salinity response to rainfall

The salinity response to different forcing scenarios was evaluated with two metrics: (1) the length of time a rain event produced significant salinity anomalies, and (2) the time at which

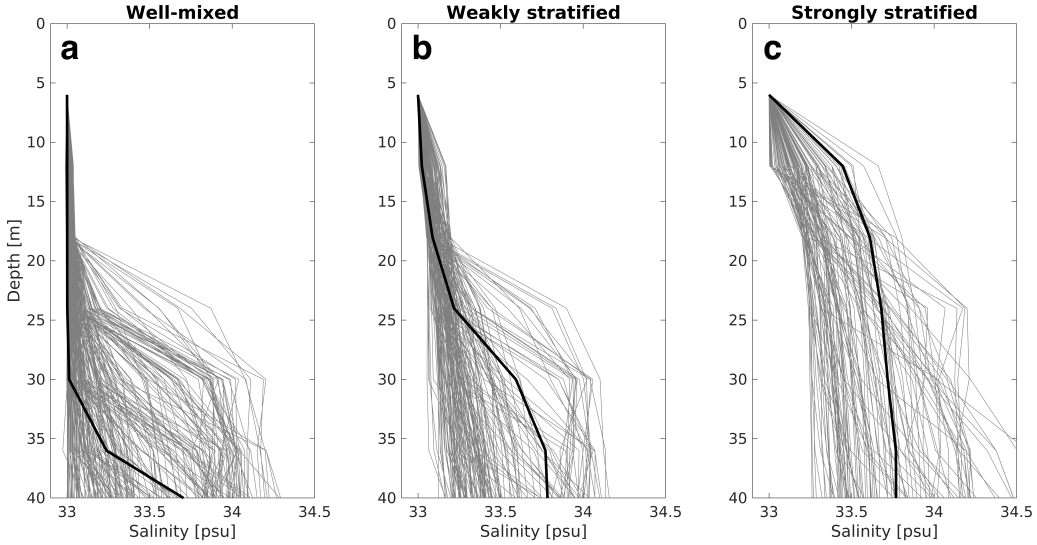

Figure 1.4: Salinity profiles collected with an underway CTD during the October-November 2017 SPURS-2 cruise classified based on the difference between salinity at 6 m (S_{6m}) and 18 m (S_{18m}) depth. Grey lines show profiles classified into (a) well-mixed ($\Delta S < 0.05$ psu, where ΔS is defined as $S_{18m} - S_{6m}$); (b) weakly stratified (0.05 psu $< \Delta S < 0.2$ psu); and (c) strongly stratified ($\Delta S > 0.2$ psu) categories. Black lines show representative profiles used as initial conditions in GOTM experiments. Plotted profiles were adjusted to have a surface salinity of 33 psu to highlight differences in stratification between the classifications.

a maximum salinity anomaly was observed. Metrics (1) and (2) were estimated at several depths and were computed from the point of time when 50% of the total accumulated rain had fallen during a given rain event, hereinafter referred to as time 0:00 (the center of the rain event). Comparing the salinity response relative to time 0:00 removes the bias that would exist if measuring from the beginning or end of the rain event due to asymmetric rain forcing in LS and TS rain events. Model simulations with no rain forcing but otherwise identical oceanic and atmospheric forcing conditions were also run; salinity anomalies (dS) were defined as the salinity differences between the results from the rain and no-rain simulations.

To compute metric (1), points in time were identified when salinity anomalies at 0.015 m (the top model level, referred to as 0 m for simplicity), 10 m, and 20 m depth were at least 0.10, 0.03, and 0.01 psu, respectively. Hereinafter, significant salinity anomalies at 0 m, 10 m, and 20 m depth will be referred to as $dS_{0m} > 0.10$ psu, $dS_{10m} > 0.03$ psu, and $dS_{20m} > 0.01$ psu. These values were chosen to represent typical strong salinity anomalies at the respective depths following rain (Anderson and Riser, 2014); 0.01 psu is a rough lower limit to what is observable in the field. To compute metric (2), the maximum value of dS was determined at 0 m, 5 m, 10 m, 15 m and 20 m depth: estimating maximum salinity anomalies at multiple depths allows us to assess how quickly freshwater propagates downward in the mixed layer.

1.5 Salinity response to convective and stratiform rain

Figure 1.5 shows the results of the Level 1 GOTM simulations, which investigate the differences in salinity structure following convective and stratiform rain. Below roughly 10 m, the salinity decrease following rain is generally similar for the convective and stratiform cases. However, the timing of the salinity response differs significantly between the two rain types: maximum salinity anomalies are observed one to two hours earlier following stratiform rain at 10 m and 15 m depth, with a much greater difference at 20 m depth (Table 1.2, Figure 1.5b,c). This implies that freshwater from stratiform rain mixes downward more efficiently than freshwater from convective rain. Stratiform rain thus generates a longer-lasting salinity anomaly below the surface (Table 1.1). In contrast, a stronger and longer-duration surface

Table 1.1: Duration (hours:minutes) when significant salinity differences (dS) are observed between GOTM experiments and a no-rain test case at 0 m, 10 m, and 20 m depth. Significant salinity differences were defined with dS thresholds of 0.10 psu at 0 m, 0.03 psu at 10 m, and 0.01 psu at 20 m. No value indicates that dS was always less than the threshold value. A greater-than symbol (>) indicates that a significant salinity anomaly was present at the end of the 24-hour model simulation, i.e., the anomaly would have persisted longer if the model was run for longer than 24 hours.

Level	Experiment	0.10 psu at 0 m	0.03 psu at 10 m	0.01 psu at 20 m
1	Convective	3:46	10:28	>8:04
1	Stratiform	-	5:53	>11:06
2,3	C-WM	4:26	10:18	>6:42
2	C-WS	5:10	>11:19	-
2	C-SS	11:42	>3:41	-
3	TS-WM	4:45	9:10	>6:56
3	LS-WM	2:40	6:14	>10:39
3	LTS-WM	3:29	6:32	>9:16

salinity response is observed following convective rain (Figure 1.5b) compared to stratiform rain (Figure 1.5c). At the surface, the difference in salinity between the convective and stratiform experiments exceeds observable limits (defined as being > 0.01 psu) for roughly 10 hours (Figure 1.5d). These differences result from the patterns of rain forcing. In the stratiform case, rain is input over a long period of time, generating only weak near-surface stratification, so freshwater can more efficiently penetrate downward. In contrast, strong stratification immediately following convective rain inhibits mixing and slows downward freshwater propagation.

These findings suggest that large decreases in sea surface salinity result from convective rain, but stratiform rain may cause a disproportionately long salinity response at deeper depths. As discussed in section 2, common modes of rainfall in the eastern Pacific ITCZ often contain both convective and stratiform precipitation, but differ in the timing of the convective and stratiform components. Further analysis of the differences in near-surface salinity response between realistic rain modes is presented in section 7.

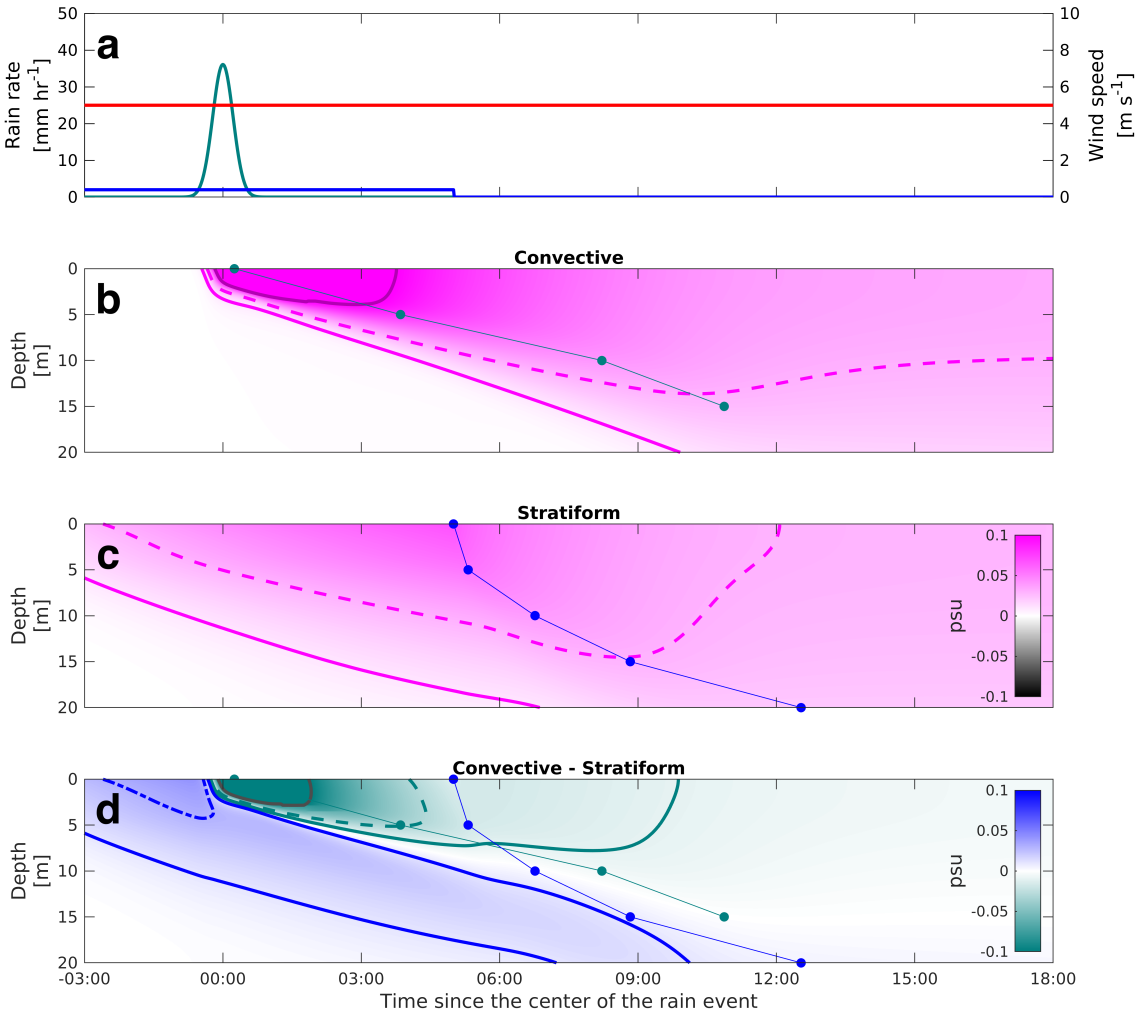

Figure 1.5: Level 1 simulations. (a) Wind speed (red) and rain rate prescribed in idealized convective (green) and stratiform (dark blue) GOTM experiments. The x-axis shows time since 0:00. Salinity difference between the (b) convective and (c) stratiform experiment and a no-rain experiment (dS). Pink shading represents when either rain case was fresher than the no-rain case. (d) Salinity difference between the convective and stratiform experiments. Green shading represents when the convective case was fresher and blue shading represents when the stratiform case was fresher. Green (blue) points show the times when dS was maximum for the convective (stratiform) experiment at 0, 5, 10, 15, and 20 m. Contours in (b), (c), and (d) represent 0.10 (dark solid), 0.03 (pink/blue/green dashed), and 0.01 (pink/blue/green solid) psu.

Table 1.2: Time, relative to the center of the rain event, of maximum dS at each given depth in GOTM experiments

Level	Experiment	0 m	5 m	10 m	15 m	20 m
1	Convective	0:15	3:51	8:13	10:52	>18:00
1	Stratiform	5:00	5:19	6:46	8:50	12:32
2,3	C-WM	0:17	4:33	9:37	12:40	>18:00
2	C-WS	0:17	4:40	10:40	>18:00	>18:00
2	C-SS	0:17	4:53	>18:00	>18:00	>18:00
3	TS-WM	0:04	4:50	9:27	12:29	>18:00
3	LS-WM	0:16	3:04	6:16	9:07	11:53
3	LTS-WM	0:09	3:46	7:26	10:04	>18:00

1.6 Influence of preexisting stratification on the salinity response to rain

Stratification in the mixed layer varies significantly in the eastern tropical Pacific in the rainy summer-autumn season (Figure 1.2c,d,e). Level 2 experiments (Figure 1.6) assess how the salinity response to rain modes varies as a result of preexisting stratification. These experiments will hereinafter be referred to as C-WM (convective rain over a well-mixed ocean), C-WS (convective rain with weak preexisting stratification) and C-SS (convective rain with strong preexisting stratification). Near the surface, the duration of salinity anomalies is lengthened when stronger preexisting stratification is present (Table 1.1; Figure 1.6). For instance, $dS_{0m} > 0.10$ psu following C rain for 4:26 in well-mixed conditions (C-WM), 5:10 in weakly stratified conditions (C-WS), and 11:42 in strongly stratified conditions (C-SS; Figure 1.6b,c,d). This suggests that strong preexisting stratification inhibits mixing and slows the downward propagation of freshwater. Maximum salinity anomalies are observed at the surface and at 5 m depth at roughly the same time regardless of stratification conditions (Table 1.2, columns 1-2). This is likely due to two factors. First, the timing of maximum salinity anomalies near the surface is directly related to the timing of rain forcing: as soon as rain weakens or stops falling, salinity anomalies cannot strengthen. Second, stratification is only prescribed at 6 m depth and below; shallower levels are expected to be well-mixed

in the absence of rainfall or diurnal warming. Therefore, turbulent mixing in the top 5 m is expected to be similar in all cases.

$dS_{10m} > 0.03$ psu for over 11 hours in experiment C-WS (Table 1.1; Figure 1.6c). This is longer than observed in experiment C-WM (Table 1.1) and can be attributed to two factors. First, preexisting stratification in experiment C-WS (Figure 1.4b) is weak enough that freshwater can propagate down to 10 m relatively quickly, on similar timescales as experiment C-WM; Table 1.2 shows that the maximum dS is observed at 10 m depth during experiment C-WS only about one hour later than in experiment C-WM (Figure 1.6b,c). Second, preexisting stratification between 12 and 15 m (Figure 1.4b) prevents freshwater from quickly penetrating deeper than roughly 15 m (depth of pink shading, Figure 1.6c). Hence, when rain falls over a weakly stratified ocean, freshwater reaches 10 m depth quickly but does not efficiently mix much deeper and salinity anomalies at 10 m persist. Experiment C-SS has much stronger preexisting stratification between 5 and 15 m depth than experiment C-WS (Figure 1.4b,c), and thus slows the downward propagation of freshwater by a greater amount (C-WS vs. C-SS; Figure 1.6c,d). Hence, a maximum dS at 10 m depth is not observed by 18:00 in experiment C-SS (Table 1.2, Figure 1.6d). These results also demonstrate the importance of the depth of the stratification in modulating mixing: in experiment C-SS, significantly stronger preexisting stratification is present above 10 m depth (Figure 1.4b,c), so it takes much longer for freshwater to propagate down to 10 m. Because it takes many hours for freshwater to reach 10 m depth, $dS_{10m} > 0.03$ psu for only 3:41 at 10 m depth in contrast to the $>$ 11 hour anomaly in experiment C-WS (Table 1.1). These values are limited by the experimental set-up: we only calculate salinity anomalies up to 18 hours following the center of rain events. If the model runs were extended, these anomalies would be observed for longer. However, it is unrealistic to extend the simulations without considering the mixing generated by nighttime convection, which is beyond the scope of this work.

During the Level 2 experiments with preexisting weak and strong stratification (C-WS and C-SS), maximum salinity anomalies at 15 m and 20 m are not observed until after 18:00 and conditions when $dS_{20m} > 0.01$ psu are never observed (Table 1.1). Figures 1.6c and 1.6d

show that salinity is higher below the fresh layer in experiments C-WS and C-SS compared to the no-rain case. This is because in the no-rain case, freshwater input doesn't strengthen preexisting stratification, leading to stronger turbulent mixing and hence lower salinities at depth.

1.7 Salinity response to predominant rain modes

Level 3 GOTM experiments (C-WM, LS-WM, TS-WM, LTS-WM) compare the salinity responses of the four rain modes that contribute significantly to the total rain accumulation in the eastern tropical Pacific: C, LS, TS, and LTS rain. Preexisting well-mixed upper ocean profiles (Figure 1.4a) are prescribed in these experiments, which will be referred to as experiments C, LS, TS, and LTS in this section for simplicity. In all four experiments, the maximum magnitudes of salinity anomalies are similar (Figure 1.7), consistent with previous studies showing a correlation between maximum salinity anomaly and peak rain rate (Boutin et al., 2014; Drucker and Riser, 2014; Drushka et al., 2016). However, the duration and timing of the salinity response to different rain modes varies. Figure 1.7 illustrates that experiments C (Figure 1.7b) and TS (Figure 1.7c) both have longer salinity responses at the surface than experiments LS (Figure 1.7d) and LTS (Figure 1.7e): $dS_{0m} > 0.10$ psu for 4:26 and 4:45 following C and TS rain, but only for 2:40 and 3:29 following LS and LTS rain (Table 1.1, Figure 1.7). Similar trends are also observed at 10 m depth with larger differences in time: $dS_{10m} > 0.03$ psu for 10:18 and 9:10 in experiments C and TS, but only 6:14 and 6:32 in experiments LS and LTS. The opposite pattern is observed at 20 m depth: $dS_{20m} > 0.01$ psu for 10:39 and 9:16 in experiments LS and LTS and for 6:42 and 6:56 in experiments C and TS, respectively. In other words, salinity anomalies following C and TS rain are surface-intensified, while those following LS and LTS rain have a longer impact at depth. The maximum salinity anomalies at 5 m depth and deeper are observed much earlier in experiments LS and LTS compared to experiments C and TS (Table 1.2; Figure 1.7). For instance, at 5 m depth, the maximum salinity anomaly is observed at 4:33 and 4:50 in experiments C and TS, but 3:04 and 3:46 in experiments LS and LTS. These time differences

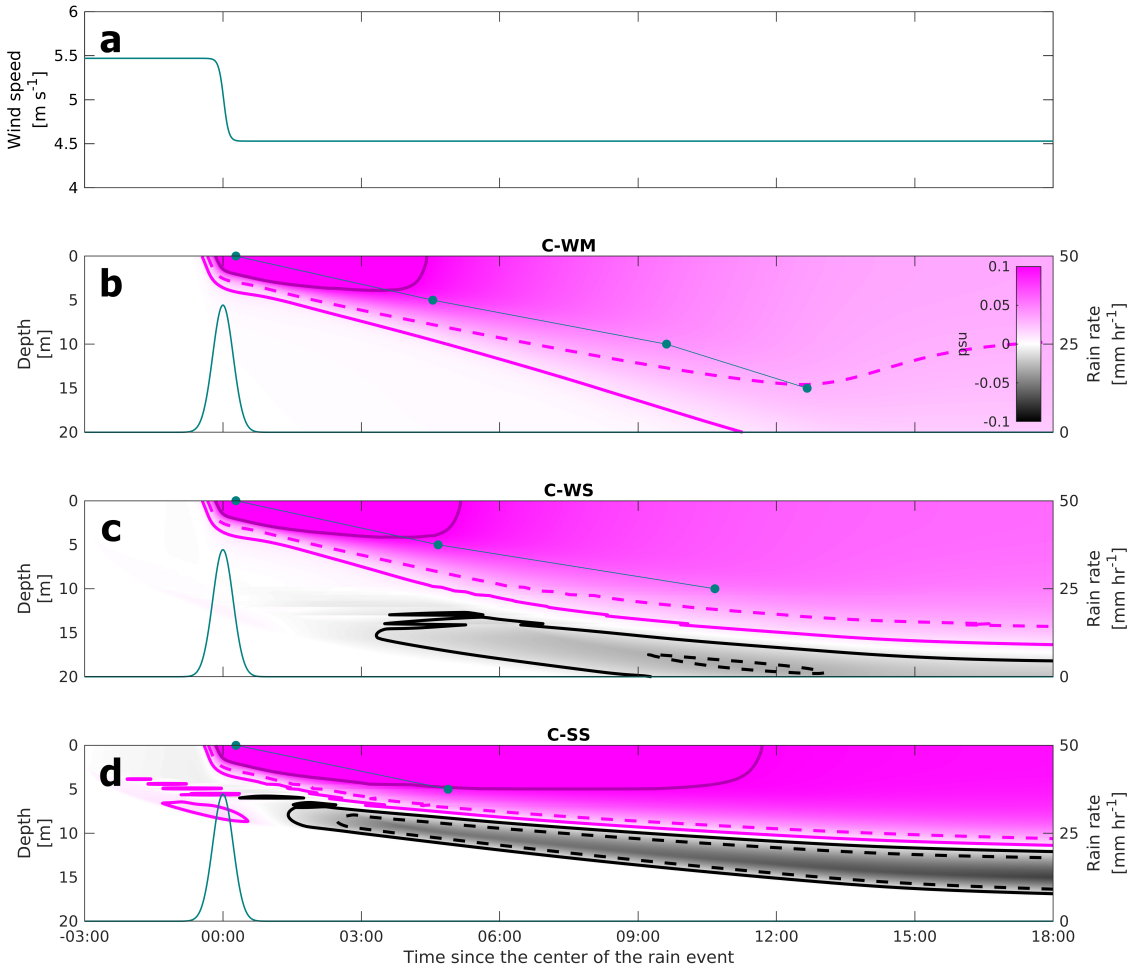

Figure 1.6: Level 2 experiments: Salinity response to isolated convective rain. (a) Prescribed wind speed for model experiments C-WM (well-mixed), C-WS (weakly stratified), and C-SS (strongly stratified). (b) Salinity difference (dS) between experiment C-WM and a no-rain experiment. Pink shading represents when/where experiment C-WM was fresher, and black shading represents when/where the no-rain experiment was fresher. The solid line shows rain rate (scale on right-hand side). Points show the times of maximum dS. (c),(d) Same as (b), for experiments C-WS and C-SS. Contours in (b), (c), and (d) are 0.10 (dark solid), 0.03 (pink dashed), and 0.01 (pink solid) psu dS contours.

increase to 2-4 hours at 10-15 m depth. At 20 m depth, the maximum salinity anomaly is observed at 11:53 in experiment LS, but not observed by 18:00 in the other three Level 3 experiments.

It is evident that the salinity responses of experiments C and TS are similar (Figure 1.7b,c). In both cases, freshwater is first input to the ocean as intense convective rain. This generates strong near-surface stratification, which inhibits freshwater from mixing downward. Freshwater from trailing stratiform rain in experiment TS remains near the surface because it falls over a highly stratified surface layer that was created by the initial convective rain. C and TS rain thus generate similar surface salinity structures. Furthermore, patterns of wind forcing are similar for experiments C and TS: winds are initially higher before decreasing near the peak rain rate.

Unlike C and TS rain, LS and LTS events have stratiform rain falling at the beginning of the rain event, generating weaker near-surface stratification that enables freshwater to penetrate downward more efficiently. This leads to a relatively short surface salinity response. Because freshwater mixes downward quickly, salinity anomalies are observed earlier at deeper depths. Because the freshwater signal in LS and LTS events is observed earlier at 20 m depth, it also lasts longer compared to other rain modes (Table 1.1, Figure 1.7). The pycnocline at 30 m (Figure 1.4a) prevents freshwater from mixing much deeper than that. Freshwater mixes downward most quickly in experiment LS, because this experiment has the largest amount of leading stratiform rain.

Model experiments conducted for LS, TS, and LTS rain with weak and strong preexisting stratification (not shown) suggest that stratification has a similar effect on the salinity response regardless of the mode of rainfall: in all cases, strong preexisting stratification inhibits downward mixing. Stronger stratification magnifies the difference between the duration of the salinity response to different rain modes. For instance, $dS_{0m} > 0.01$ psu for approximately 5 hours longer following C and TS rain compared to LS and LTS rain over a strongly stratified ocean; this difference is only 1-2 hours for the well-mixed experiments shown in Figure 1.7. Because generally similar results are observed for different rain modes, detailed

quantitative results from these simulations are not presented here.

1.8 Discussion and conclusions

While the model experiments provide insight into effects of rain forcing and preexisting stratification on near-surface salinity, it is important to note that several other factors will significantly influence the salinity response to rain. These include variability in ocean, air and raindrop temperatures, short-term fluctuations in wind speed and rain rate, and time of day. Idealized wind speeds that varied by less than a few $m\ s^{-1}$ over the course of a rain event were prescribed in model simulations. Observed wind speeds generally varied between 0 and 15 $m\ s^{-1}$ over the entire data set, although fluctuations during single rain events were typically much smaller than this. Generally, higher wind speeds would generate more turbulence and drive a faster and shorter-duration salinity response. Similarly, lower wind speeds would drive a longer-duration salinity response. During the night, convection in the upper ocean would generate faster downward mixing of freshwater following rain.

The difference in the salinity responses to rain over different preexisting stratification conditions is generally greater than the difference between the salinity responses to different rain modes (Table 1.1). For instance, the surface salinity response to C rain falling on a strongly stratified ocean lasted 7 hours longer than that to C rain falling on a well-mixed ocean (Figures 1.6b,1.6d). This is much greater than the difference in duration of salinity anomalies between rain modes: $dS_{0m} > 0.10$ psu for only 2 hours longer following C rain than following LS rain on a well-mixed ocean (Figures 1.7b,1.7d). We note that these idealized simulations do not represent the variance of atmospheric and ocean conditions present in the real world. For instance, if wind speeds are sufficiently strong, even a strong rain event falling on a stratified ocean may produce only a short surface salinity response as a result of strong near-surface mixing. The timing of rain relative to the diurnal cycle will also affect background oceanic and atmospheric conditions and in turn the downward mixing of freshwater following rain. In any case, the model results suggest that stratification is dominant compared to rain forcing in modulating the salinity response to rain: when preexisting

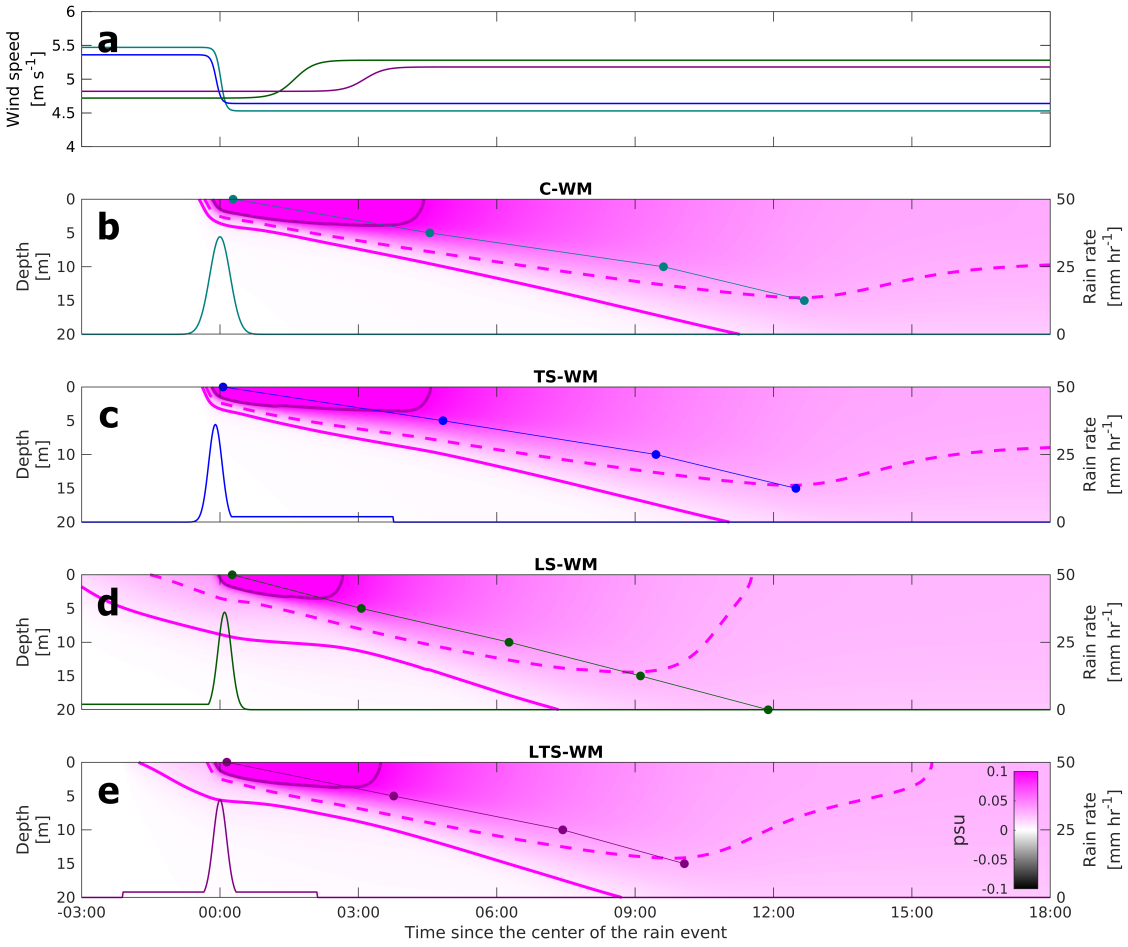

Figure 1.7: Same as Figure 1.6 for the Level 3 experiments, showing the salinity response to rain on a well-mixed ocean. (a) Prescribed wind speed for model experiments C-WM (light green; isolated convective), LS-WM (blue; convective with leading stratiform), TS-WM (dark green; convective with trailing stratiform), and LTS-WM (purple; convective with leading and trailing stratiform). (b) Salinity difference between experiment C-WM and a no-rain experiment. (c),(d),(e) Same as (b) for experiments TS-WM, LS-WM, and LTS-WM.

stratification is present, freshwater from rain is confined near the surface and slowly mixes downward. Preexisting stratification in the eastern tropical Pacific results from longer-term freshwater input from the ITCZ and ocean dynamics (Bingham et al., 2020; Katsura and Sprintall, 2020; Katsura et al., 2021). Stratification is also produced locally by individual rain events (Iyer and Drushka, 2021b). Well-mixed, weakly stratified, and strongly stratified conditions are all frequently observed throughout the tropics and subtropics: stratified conditions are present about 40% of the time year-round with significant seasonal and geographic variability (Figure 1.2a-d). Because stratification, both preexisting and from individual rain events, is responsible for the persistence of freshwater near the surface following rain is and frequently observed in the tropics and subtropics, it should be taken into account in applications that estimate the salinity response to rain. An assumption of well-mixed conditions would greatly underestimate the duration of the freshwater response to rain near the surface and overestimate the speed at which freshwater propagates downward, with the largest error when stratification is strong or winds are weak. Differences in subsurface salinity between Figures 1.6b, c, and d imply that assuming a well-mixed ocean would lead to the greatest error at depths below the surface.

The Level 3 experiments show that the salinity responses to C and TS rain are similar: both are associated with longer-lasting surface salinity anomalies compared to events with leading stratiform rain. As highlighted previously, these findings represent idealized events with moderate winds rather than individual events, and significant variability exists due to background atmospheric and oceanic conditions and variability. Because C and TS rain account for over half (53%) of the total accumulation at the SPURS-2 central mooring, C and TS rain are likely the primary drivers of low sea surface salinity in this region. On the other hand, LS and LTS rain events are associated with relatively short-lived surface salinity anomalies and a smaller fraction (43%) of the total rain accumulation. Because LS and LTS rain are less frequent and associated with a short surface salinity response, those modes are likely a less significant driver of low sea surface salinities in this region. However, at 20 m depth, LS and LTS rain events are associated with long-lasting salinity anomalies (Table

1.1). This suggests that events that begin with stratiform rain may be disproportionately responsible for low salinities in the mixed layer.

Because in situ observations of collocated sea surface salinity and rain are scarce, satellite observations have been widely utilized to study the relationships between rainfall and sea surface salinity (Yu, 2011; Reul et al., 2014; Boutin et al., 2014, 2016; Supply et al., 2018). Microwave satellite rain products typically only resolve rain rates of up to a few $mm\ hr^{-1}$ because of spatial averaging (Wilheit et al., 1991; Chiu et al., 1993; Kummerow, 1998), while radar-based satellite rain estimates can only provide estimates when a satellite is directly overhead and therefore have a limited temporal resolution (Tan et al., 2017; Sun et al., 2018). As a result, rain estimates from gridded satellite products often resemble stratiform rain, regardless of the actual predominant modes of rain. Only 4% of the total rain accumulation in the SPURS-2 region is due to exclusively stratiform events, so satellite rain observations do not represent the dominant modes of rain that create the low sea surface salinities in this region. This is a potential hindrance to studies using satellite measurements of rain and sea surface salinity: the surface salinity structure is primarily created by C, LS, TS, and LTS rain, whose forcing cannot be resolved by satellites. However, because low-intensity rainfall produces a long-lasting subsurface salinity response, satellite rain observations may better represent the rain that generates low salinities deeper in the mixed layer, such as those observed by Argo or ship-based CTDs. Our results also indicate that the duration of the salinity response to rain varies significantly between rain modes that may be indistinguishable based on satellite observations. In addition, the significant effect of preexisting stratification on the salinity response to rain implies that the salinity response to rain cannot be accurately predicted without considering the background stratification. Stratification is particularly important to consider at low latitudes but some stratification is observed throughout the tropics and midlatitudes at least 20% of the time (Figure 1.2). These inconsistencies imply that there are limitations to models utilizing satellite rain data to predict near-surface salinity anomalies, such as the Rain Impact Model (Santos-Garcia et al., 2014; Jacob et al., 2019).

Our results also demonstrate that the depth of observations is of critical importance

for interpreting how freshwater from rain is mixed into the deeper and larger-scale salinity structure. Several previous studies have identified a bias between satellite observations of the surface and Argo observations at 5 m, and have attributed this bias to rain (Boutin et al., 2013; Anderson and Riser, 2014; Boutin et al., 2014; Drucker and Riser, 2014; Lee, 2016). Understanding of this bias could potentially be improved by considering individual rain modes and preexisting stratification. Rain modes with a strong surface salinity response (C and TS), or rain falling on a strongly stratified ocean, would be expected to have a relatively large salinity bias between the surface and 5 m depth. LS and LTS rain, or rain falling on a well-mixed surface layer, would be expected to be associated with a smaller salinity difference in the top 5 m.

1.9 Summary and Conclusions

The results suggest that freshwater mixes away at different time and depth scales following different modes of rainfall. Slightly more than half of the total rain accumulation in the SPURS-2 region is C and TS rain. Freshwater input from these rain modes creates a long-lasting surface salinity anomaly. Slightly less than half of the total rain accumulation is associated with LS and LTS rain, which produces a short-lived surface salinity anomaly and longer-lasting salinity signature at 10-20 m depth in the mixed layer. Preexisting stratification greatly influences the salinity response to rain: in general, when stronger stratification is present, freshwater is confined to the surface for a longer period of time.

Finally, our results provide a means to determine the ocean salinity structure over large spatial areas from high-resolution satellite or ship-based radar observations, such as those made by Thompson et al. (2019a) and Rutledge et al. (2019). The results from the present study could potentially be extended to other regions outside of the ITCZ where different modes of rain are more common. For example, at higher latitudes where stratiform rain comprises a larger part of the total rain accumulation, the salinity response to rain may be more pronounced at deeper depths.

Chapter 2

VARIATIONS IN WAVE SLOPE AND MOMENTUM FLUX FROM WAVE-CURRENT INTERACTIONS IN THE TROPICAL TRADE WINDS

This chapter is published in *Journal of Geophysical Research: Oceans* as **Iyer, S., J. Thomson, E. Thompson, and K. Drushka, 2022. Variations in wave slope and momentum flux from wave-current interactions in the tropical trade winds. Journal of Geophysical Research-Oceans 127 (3), e2021JC018003, doi.org/10.1029/2021JC018003**.

Abstract

Observations from six Lagrangian Surface Wave Instrument Float with Tracking (SWIFT) drifters in January-February 2020 in the northwestern tropical Atlantic during the Atlantic Tradewind Ocean-atmosphere Mesoscale Interaction Campaign (ATOMIC) are used to evaluate the influence of wave-current interactions on wave slope and momentum flux. At observed wind speeds of 4-12 ms^{-1}, wave mean square slopes are positively correlated with wind speed. Wave-relative surface currents varied significantly, from opposing the wave direction at 0.24 ms^{-1} to following the waves at 0.47 ms^{-1}. Wave slopes are 5-10% higher when surface currents oppose the waves compared to when currents strongly follow the waves, consistent with a conservation of wave energy flux across gradients in currents. Assuming an equilibrium frequency range in the wave spectrum, wave slope is proportional to wind friction velocity and momentum flux. The observed variation in wave slope equates to a 10-20% variation in momentum flux over the range of observed wind speeds (4 to 12 ms^{-1}), with larger variations at higher winds. At wind speeds over 8 ms^{-1}, momentum flux varies by at least 6% more than the variation expected from current-relative winds alone, and suggests

that wave-current interactions can generate significant spatial and temporal variability in momentum fluxes in this region of prevailing trade winds. Results and data from this study motivate the continued development of fully coupled atmosphere-ocean-wave models.

2.1 Introduction

2.1.1 Importance and Background

Air-sea interactions are an important component of the global climate system, as they modulate the transfer of heat, buoyancy, momentum, and gases between the atmosphere and the ocean and are a driving force behind creating boundary layer to multidecadal-scale patterns in weather and climate. Surface gravity waves are a key component of the air-sea interface and modulate the transfer of momentum from the atmosphere to the ocean through modification of surface drag (e.g., Janssen, 1989, and others), energy injection from breaking (e.g., Craig and Banner, 1994, and others), and momentum storage in the wave field (e.g., Ardhuin et al., 2004; Fisher et al., 2017, and others). Existing work on the role of waves in air-sea interaction often parameterizes this process using a wind speed-dependent drag coefficient (Smith, 1980; Large and Pond, 1981; Edson et al., 2013), or incorporates waves only through a wave age parameterization, which has been found to produce similar results as parameterizations incorporating wind speed alone (Edson et al., 2013). While these assumptions may be reasonable when waves are modified only by wind and when wind-wave equilibrium (Phillips, 1985) holds, significant uncertainties exist when other processes affect surface waves. A primary objective of the present study is to evaluate the significance of wave-current interactions, which are not typically incorporated into model parameterizations on wave properties and momentum flux at small scales. Another focus is to compare observations with momentum flux calculated using the COARE bulk flux algorithm (Fairall et al., 1996, 2003; Edson et al., 2013), a widely-used scheme which incorporates current and wave effects on stress through current-relative winds and wave age, respectively, but does not parameterize wave-current interactions. It is well documented that surface currents vary at

the mesoscale and smaller scales due to eddies and fronts (e.g., Molinari et al., 1981; Ebuchi and Hanawa, 2000; van Aken, 2002; Kim, 2010; McWilliams, 2016, and others); presumably, these current variations would lead to spatial differences in wave-current interactions and momentum flux.

In theory, when waves propagate over an area with spatially varying surface currents, a Doppler shift will modify the apparent wave frequency and effective rate of wave energy propagation by an amount dependent on the alignment of the surface current and the waves. Because the horizontal wave energy flux is conserved along a ray path, changes in the rate of energy propagation cause changes in the local energy density (much like the shoaling process in shallow water). The net effect is to elevate wave slopes when surface current gradients are opposed to wave propagation, and decrease wave slopes when surface current gradients follow wave propagation. The frequency shift is caused by the projection of the current vector onto the wave direction; this component will hereinafter be referred to as the wave-relative current. In areas where currents are spatially variable such as across fronts, wave slopes would be expected to vary on those same spatial scales. This has been observed in the field (Thomson et al., 2014; Zippel and Thomson, 2017; Branch et al., 2018; Kastner et al., 2018; Gemmrich and Pawlowicz, 2020) and simulated by numerical models (Akan et al., 2017, 2018; Moghimi et al., 2019) in coastal areas where strong spatial current variability exists. Specifically, energy levels, significant wave height, whitecapping, wave breaking, and near-surface turbulent dissipation rates are elevated where currents oppose the waves due to wave steepening. Wave properties can vary on spatial scales of ones to tens of km (e.g. Thomson et al., 2014; Branch et al., 2018) or larger (e.g., Gemmrich and Pawlowicz, 2020), depending on the structure of coastal features associated with current variability, including river plumes (Thomson et al., 2014; Branch et al., 2018), fronts, and upwelling jets (Romero et al., 2017). Near river mouths, currents can even be strong enough to reduce the wave group velocity to zero and block the propagation of waves on the side of a front where currents strongly oppose the waves (Chawla and Kirby, 2002; Chen and Zou, 2018).

Only a limited amount of research on wave-current interactions has focused on the open

ocean, where currents are typically more wind- and wave-following than in localized coastal areas. Romero et al. (2017) quantify current effects on wave properties associated with the Loop Current in the Gulf of Mexico. Strong fronts with surface current gradients of up to 1.5 ms^{-1} over roughly 50 km exhibited variations in wave height and slope of up to 30%, with greater variation in whitecap coverage. At O(100 km) scales, storms and western boundary currents have been shown to modulate wave properties in the presence of strong surface currents (Holthuijsen and Tolman, 1991; Wang and Sheng, 2016; Hegermiller et al., 2019). Wave-current interactions in the open ocean have also been shown to vary temporally due to varying inertial and tidal currents (Gemmrich and Garrett, 2012). Finally, as in coastal areas, current variations on very small scales can occur in the open ocean: Rascle et al. (2017) observed sea surface roughness anomalies across a 50 m-wide submesoscale front and attribute this to strong current gradients of 0.3 ms^{-1}. These results demonstrate that wave-current interactions associated with strong surface current variability are important in the open ocean as well as coastal areas.

Wave-current interactions have been frequently studied using models. Mesoscale features on O(10-100 km scales) cause variations in wave properties through refraction, the advection of energy, the energy exchange between waves and currents, the aforementioned Doppler frequency shift, and the effect of currents on the wind stress between the ocean and atmosphere (Ardhuin et al., 2017). Romero et al. (2020) quantify some of this variability on O(1-10 km scales) with numerical modeling, and demonstrate that wave-current interactions most significantly influence wave-breaking variables including whitecap coverage and energy dissipation, particularly when winds are weak. Wave-current interactions also have a strong influence on significant wave height at scales of tens of kilometers (Ardhuin et al., 2017; Kudryavtsev et al., 2017; Quilfen et al., 2018). Similar effects on significant wave height have been shown at the mesoscale and at larger scales: Quilfen and Chapron (2019) show that current variability on scales of hundreds of kilometers can influence wave heights, and Rapizo et al. (2018) show wave flattening on even larger scales due to wave-following currents. Non-negligible effects of currents have been observed on other bulk wave variables including wave mean

square slope mss (Rascle et al., 2014; Romero et al., 2020). Current effects on waves should theoretically be more significant for wind waves having frequencies above the spectral peak (Phillips, 1984; McWilliams, 2018). While not the focus of the present study, it has been demonstrated that the reverse feedback can occur as well; i.e., waves can cause variations in surface currents (Tang et al., 2007; Suzuki et al., 2016; McWilliams, 2018). However, model results have shown that this effect is only a small contributor to submesoscale and mesoscale variability (Romero et al., 2021). Hereinafter in this manuscript, "wave-current interactions" will refer to current effects on waves, rather than wave effects on currents. A main objective of the present study is to analyze the influence of wave-current interactions on short temporal scales and spatial scales of tens of kilometers with observations. This is of similar scale to several previous modeling studies (e.g., Ardhuin et al., 2017; Romero et al., 2020), but smaller than the focus of large-scale observational studies (e.g., Holthuijsen and Tolman, 1991).

In areas with significant mesoscale or submesoscale activity, spatial gradients in currents are often associated with sea surface temperature (SST) fronts. SST fronts can generate spatial variations in air-sea heat fluxes, which can in turn modify momentum fluxes, wind, and waves. For instance, heating over the warm side of a front destabilizes the atmospheric boundary layer, which induces atmospheric convection and increases surface wind speeds through either downward momentum transfer (Wallace et al., 1989) or horizontal pressure gradients (Lindzen and Nigam, 1987). These increases in wind speed can then influence the high frequency part of the wave spectrum. The modification of air-sea fluxes by SST fronts has been observed and modeled at the submesoscale (Shao et al., 2019; Redelsperger et al., 2019) and at the mesoscale (Businger and Shaw, 1984; Friehe et al., 1991; Chelton et al., 2001, 2004; Gaube et al., 2015). The primary focus of this work will be direct effects of the currents on waves and momentum flux, but it is important to note that indirect effects such as those induced by SST fronts may also be significant.

2.1.2 Theory

We expect mss to vary as a result of currents opposing or following the waves, which will further influence surface stress (i.e., momentum flux). We know that

$$\tau = \rho_a u_*^2, \tag{2.1}$$

where

$$u_* = C_D^{1/2}(U_{10} - Ucos\theta). \tag{2.2}$$

Parameter τ is the surface wind stress, ρ_a is the air density, u_* is the friction velocity, C_D is the drag coefficient, U_{10} is the 10 meter wind speed, U is the surface current, and θ is the angle between the surface current direction and the average wave direction in an equilibrium frequency range ($f_{max} - f_{min}$). Assuming that the source of wave energy (i.e., wind) is balanced by wave breaking and nonlinear effects (Phillips, 1984, 1985), and that the wind energy input is proportional to u_* and mss (Plant, 1982), u_* can be defined as a function of the wave energy spectrum $E(f)$, which scales with f^{-4} (Phillips, 1985; Juszko et al., 1995; Thomson et al., 2013; Voermans et al., 2020). Within the equilibrium frequency range,

$$u_* = \int_{f_{min}}^{f_{max}} \frac{E(f)f^4 2\pi^3}{\beta I(p) g(f_{max} - f_{min})} df. \tag{2.3}$$

Parameter f is the wave frequency, β is an empirically determined constant taken as 0.012, g is gravitational acceleration, and I is the wave directional spreading function with parameter p as defined by Phillips (1985). Following Phillips (1985), we assume a constant p=0.5 and $I(p)$=2.5. By combining the above equation with a version of the relation of Kitaigorodskii (1983) that is normalized by the frequency width,

$$mss = \int_{f_{min}}^{f_{max}} \frac{E(f)f^4 16\pi^4}{g^2(f_{max} - f_{min})} df, \tag{2.4}$$

u_* can be related to mss as

$$\frac{u_*}{mss} = \frac{g}{8\pi\beta I(p)}. \tag{2.5}$$

Hereinafter, mss will refer to this frequency-width-normalized value rather than the unnormalized value to remove dependence on the selected equilibrium range. Equation 5 demonstrates that mss and u_* are directly proportional under the assumptions that β and $I(p)$ are constant and that there is an equilibrium frequency range $f_{max} - f_{min}$. The present study makes these assumptions, so observations presented in terms of mss and u_* are essentially equivalent and differ only by a constant factor. This wave-derived u_* is distinct from estimates based on anemometer measurements (whether bulk or turbulent), but it is meant to be the same dynamic quantity.

When waves encounter a uniform current in the same or opposite direction as the waves, the Doppler shift effect leads to a shift in wave frequency by an amount proportional to wavenumber and the component of the current velocity aligned with the waves (Phillips, 1984). This frequency shift can be defined using

$$\omega = \sigma + \vec{u} \cdot \vec{k} = \sigma + Ukcos(\theta), \tag{2.6}$$

where ω is the absolute frequency of the wave in a fixed reference frame and σ is the intrinsic frequency defined with the deep-water wave dispersion relation,

$$\sigma = 2\pi f = \sqrt{gk}. \tag{2.7}$$

Parameter $\vec{u}$ is the current and $\vec{k}$ is the wavenumber. Currents opposing the direction of wave propagation will cause an increase in wavenumber and decrease in the rate of energy propagation. When a wave-relative current $Ucos\theta$ is imposed, the surface energy flux of the waves F_{waves} is defined as

$$F_{waves} = E(f) \times (c_g(f) + Ucos\theta), \tag{2.8}$$

where E is the local energy density and $c_g(f) = \frac{g}{4\pi f}$ is the deep-water group velocity. To conserve F_{waves} when $Ucos\theta$ is negative, E must increase and the waves will steepen. This process is different for each frequency f in a given spectrum, because $c_g(f)$ is a strong function of frequency. The high-frequency components (which determine mss) have the largest effective change in the rate of energy propagation for a given $Ucos\theta$.

If waves reach a critical steepness, they can break (Phillips, 1984; van der Westhuysen, 2012; Thomson et al., 2014; Romero et al., 2017; Zippel and Thomson, 2017; Gemmrich and Pawlowicz, 2020). Similarly, currents in the same direction as the waves will experience a decrease in wavenumber, increase in wave speed, and flattening. Wave properties are further modified when strong vertical (Choi, 2009; Banihashemi et al., 2017; Ellingsen and Li, 2017; Banihashemi and Kirby, 2019) or horizontal (Haus, 2007) current shear exists. To account for the current effect on wave frequency in a field with variable currents, we substitute the absolute frequency ω (equation 6) for f in equation 4. This yields a relationship between mss, the intrinsic frequency σ, the wavenumber k, and the wave-relative current $Ucos\theta$. Combining this with the dispersion relation (equation 7), we can rewrite σ and k in terms of f and obtain an equation for the frequency width-normalized mss (or equilibrium u_*, using equation 3),

$$mss = \int_{f_{min}}^{f_{max}} \frac{16\pi^4 f^4 E(f)}{g^2(f_{max} - f_{min})} \left(1 + \frac{8\pi f Ucos\theta}{g} + \frac{24\pi^2 f^2 (Ucos\theta)^2}{g^2} + \frac{32\pi^3 f^3 (Ucos\theta)^3}{g^3} + \frac{16\pi^4 f^4 (Ucos\theta)^4}{g^4}\right) df, \quad (2.9)$$

as a function of $Ucos\theta$ and $E(f)$, which is expected to increase at increasing wind speeds (equations 2,3). Using equation 9, we can calculate an expected variation in mss or u_* when a nonzero uniform current U is imposed at an angle θ to the wave direction.

The theory suggests that the relative surface current would also contribute to variability in u_*, both by modifying the current-relative wind speed ($U_{10} - Ucos\theta$ in equation 2; Figure 2.1a) and through wave-current interactions. It is important to note that while these two

mechanisms both result from surface currents, they are physically distinct. Surface currents will influence the current-relative wind speed and u_* regardless of spatial variability. That is, in a hypothetical ocean where surface currents are spatially invariant but nonzero, u_* will still be increased or decreased compared to a case where surface currents are zero. On the other hand, wave-current interactions only occur in the presence of spatial variability: A wave has to propagate across an area of spatially varying surface currents for the Doppler shift and conservation of wave energy flux to alter the wave steepness. The analysis in this manuscript discusses both of these processes and often makes the assumption that because data were collected in a region where winds are consistently from the same direction, deviations in currents from the strongly wind-following direction are associated with spatial variability.

A recent study estimated wind speed from in situ observations of wave spectra and found that observed wind speeds between 3 and 12 ms^{-1} are generally consistent with values predicted from equation 3, with uncertainty resulting from sea state and buoy motion (Voermans et al., 2020). While wave properties vary significantly due to the Doppler shift effect in coastal regions where surface currents are strong and variable (Thomson et al., 2014; Campana et al., 2016; Zippel and Thomson, 2017; Gemmrich and Pawlowicz, 2020), the influence of wave-current interactions on u_* has not been explored in the open ocean using observations, with the exception of areas with strong mesoscale activity and current variations (Holthuijsen and Tolman, 1991; Romero et al., 2017; Hegermiller et al., 2019). The theory suggests that even small spatial changes in surface currents will have non-negligible effects on u_* (Figure 2.1b), so wave-current interactions may still be important in locations away from coastal areas or major western boundary currents. Furthermore, areas without strong mesoscale activity are more representative of the global ocean as a whole. A goal of the present study is to evaluate the impact of wave-current interactions in a region of moderate mesoscale activity (Figure 2.2).

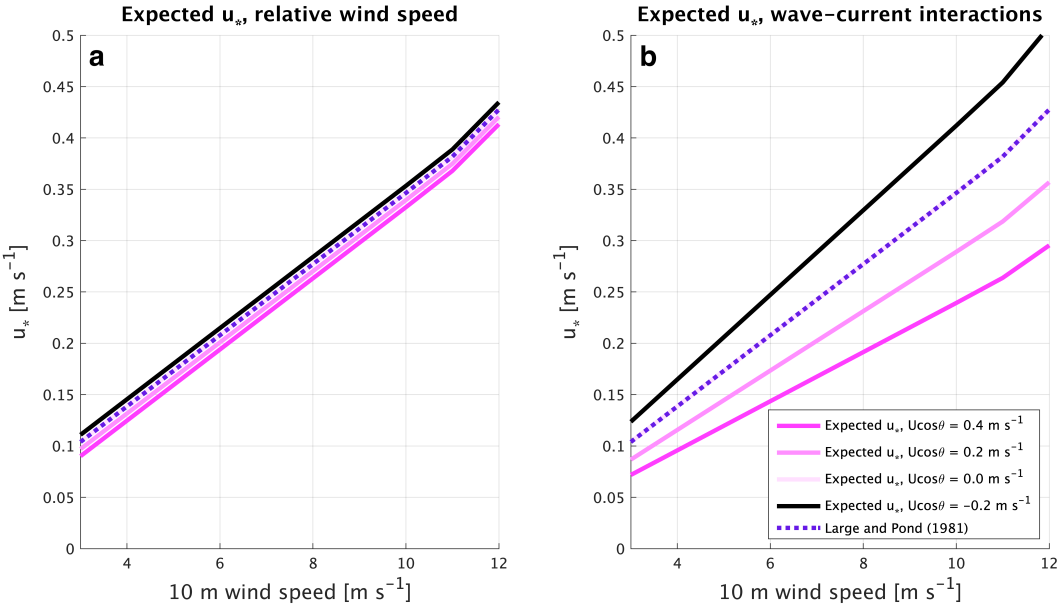

Figure 2.1: (a) Expected variation in u_* due to the direct effect of currents, assuming C_D from Large and Pond (1981) (current-relative wind, equation 2); (b) Expected variation in u_* due to wave-current interactions (equations 5,8,9).

2.2 Methods

2.2.1 Study site

The NOAA Atlantic Tradewind Ocean-atmosphere Mesoscale Interaction Campaign (ATOMIC), part of EUREC^{4}A (Stevens et al., 2021), took place in January-February 2020 in the northwestern tropical Atlantic, east-northeast of Barbados (Figure 2.2). This region is north of the inter-tropical convergence zone and well within the trade wind region. As a result, wind and waves are typically strong and westward following the prevailing trade winds, with minimal directional variation. The ATOMIC study site is also adjacent to a region that has strong oceanic mesoscale activity (Figure 2.2) and spatial variability in ocean temperature and salinity: The outflows of the Amazon and Orinoco Rivers are nearby and large mesoscale ocean eddies are generated by the North Brazil Current (Fratantoni and Glickson, 2002; Ffield, 2005; Fratantoni and Richardson, 2006). Despite this, only moderate eddy kinetic energy was observed during the field campaign (Figure 2.2) because the study site is farther north than the region of highest eddy kinetic energy and freshwater discharge (Reverdin et al., 2021) and the field campaign took place before the boreal spring peak in discharge (Coles et al., 2013). However, river outflow or mesoscale eddies are still likely responsible for the observed submesoscale spatial variability in the ATOMIC study area (Figure 2.2).

2.2.2 SWIFT observations

During the ATOMIC field campaign, two version 3 (v3) Surface Wave Instrument Float with Tracking (SWIFT) drifters (Thomson, 2012) and four version 4 (v4) SWIFT drifters (Thomson et al., 2019) were deployed. The field campaign consisted of two cruise legs on the NOAA Ship Ronald H. Brown (Quinn et al., 2021) and eleven NOAA P-3 aircraft flights (Pincus et al., 2021) from Barbados to the study area shown in Figure 2.2. SWIFT drifters were deployed twice from the NOAA Ship Ronald H. Brown: from 14 Jan 2020 to 22 Jan 2020 during Leg 1 and from 30 Jan 2020 to 11 Feb 2020 during Leg 2. Leg 1 deployments were made in the northeastern part of the study area, and Leg 2 deployments were made in the

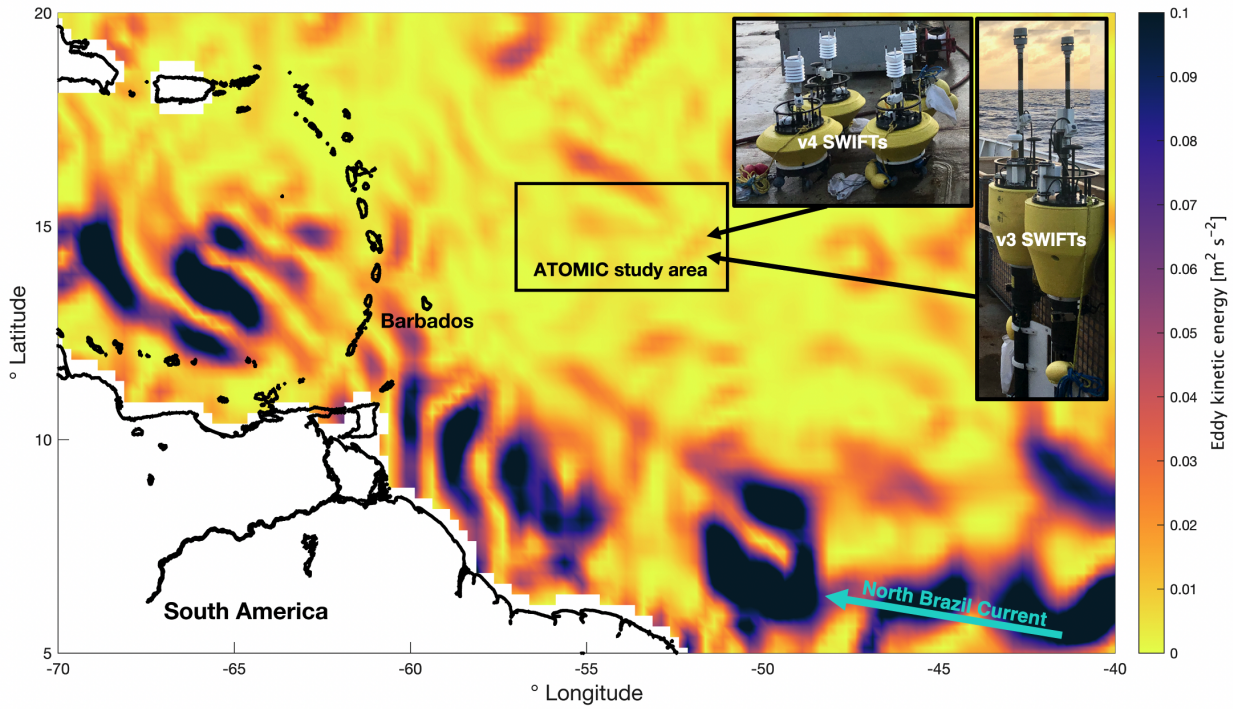

Figure 2.2: Eddy kinetic energy calculated from Copernicus Marine Environment Monitoring Service (CMEMS) satellite sea level anomalies on February 1, 2020. The rectangular box denotes the study area where SWIFTs were deployed and recovered. Inset images picture the two types of SWIFTs deployed during ATOMIC.

southwestern part of the study area. Details of these deployments and other measurements that were made during ATOMIC from the NOAA Ship Ronald H. Brown or other oceanic platforms are included in Quinn et al. (2021).

During both legs of ATOMIC, ocean temperature fronts were identified using satellite measurements and shipboard sensors. SWIFTs were then strategically deployed in a line across the front, with 5-10 km spacing between each drifter's initial deployment position. This strategy ensured that significant spatial variability in ocean temperature and surface currents was observed during the beginning of each deployment. Towards the end of deployments, SWIFT drifters converged to one (leg 1) or two (leg 2) general geographic areas due to currents.

V3 and v4 SWIFTs differed in height and had instrumentation at different heights and depths. V4 SWIFTs were equipped with Vaisala WXT350 meteorological sensors at 0.5 m height, which measured parameters including air temperature, relative humidity, and wind speed and direction. V3 SWIFTs were equipped with Airmar 200WX meteorological sensors at 0.8 m height, which measured the above parameters excluding relative humidity. Aanderaa 4319 sensors measured conductivity and ocean temperature at 0.3 m depth on v4 SWIFTs and at 0.5 m and 1.0 m on v3 SWIFTs. Nortek Signature 1000 (v4) or Nortek Aquadopp (v3) ADCPs measured ocean current velocities between 0.35 m and 20 m depth. Directional wave spectra and bulk wave parameters were estimated from inertial motion observations on both v3 and v4 SWIFTs using a Microstrain 3DM-GX3-35 (v3) or SBG Ellipse (v4) attitude and heading reference system (AHRS). These systems also included GPS measurements, with wave spectral processing as described in Thomson et al. (2018). Raw data were processed onboard, and spectral results were sent via Iridium telemetry once per hour, corresponding to a 10 minute burst of raw data at the top of each hour.

2.2.3 Data processing

Offsets in wind speed measurements were calibrated using shipboard observations made when a drifter was within 5 km of the ship by assuming that ship and drifter observations should be

identical and performing linear regressions for each platform (Thomson et al., 2021). If fewer than 5 collocated data points were available for a given regression, offsets were first corrected using observations from another drifter that was near the ship. For one v4 drifter, a distance limit of 15 km was used because of a lack of data from other drifters closer than that. Root mean square errors in offsets were generally lower than sensor precision specifications; wind speed observations from individual SWIFTs had uncertainties between 0.24 and 0.96 ms^{-1}.

SWIFT drifters are nearly Lagrangian surface-following platforms (Thomson, 2012), which drift with the surface currents. Surface currents are estimated from the drift track of SWIFTs, after subtracting the contributions from Stokes drift (following the methods of Thomson et al. (2019)) and wind slip. Stokes drift corrections are small (cms^{-1}) relative to the surface currents. Drifter slip (i.e., offset between the platform motion of near-Lagrangian drifters and the actual currents) typically is the result of drifter windage and near-surface velocity shear (Niiler and Paduan, 1995; Poulain et al., 2013). As shear was minimal (discussed in detail later in this section), we assume that drifter slip is primarily a result of windage. Following Herrera et al. (2019), slip was calculated using onboard ADCP velocity observations made in the reference frame of the drifter. Because shear was minimal, velocities at 0.85 m depth were representative of the depth-averaged relative platform velocity and were used for this calculation. In theory, onboard velocities should be zero if drifters drift with the near-surface currents. Any nonzero velocity represents the difference between the drift and the current velocity. Moderate correlation (R^2=0.37) between wind speed and ADCP velocities supports the assumption that slip is a result of wind. Wind slip was, on average, 1.09% of the wind speed, with a standard deviation of 0.27%. To correct surface currents for wind slip, a vector with magnitude of 1.09% of the wind speed in the direction of the wind was subtracted from Stokes-corrected drift tracks. When wind data were unavailable, data from the nearest drifter was used. Wind slip corrections were typically a small northeastward adjustment of 0.05 to 0.15 ms^{-1}; this direction for the adjustment is consistent with the prevailing trade winds.

Wave slopes mss and equilibrium u_* are calculated from wave spectra, assuming a con-

stant equilibrium frequency range over which the source and sink of wave energy is balanced (equations 3 and 4). Thomson et al. (2013) define the equilibrium frequency range as between 0.2 and 0.4 s^{-1}. We slightly modify this range and use $f_{min} = 0.25\ s^{-1}$ and $f_{max} = 0.4\ s^{-1}$ since swell is occasionally observed at frequencies between 0.2 and 0.25 s^{-1}. Linear fits to the equilibrium range of the spectra in log-log space have an average slope of -3.89 (Figure 2.3a,c), roughly consistent with the theoretical f^{-4} shape. Minor deviations from the f^{-4} shape are frequently observed, although spectral slopes in the equilibrium range are rarely less steep than f^{-3} or steeper than f^{-5} (Figure 2.3c). Deviations from the f^{-4} shape are likely due to noise combined with the limited amount of data (10 minutes) used to calculate each spectrum.

Spectral shapes at high frequencies may be modulated by swell waves (Vincent et al., 2019) or coupling between the swell and high frequencies (Collins et al., 2018); when swell is strong (high wave centroid periods), spectral slopes are typically steeper than f^{-4} (Figure 2.3c). The transition between the equilibrium (f^{-4}) and saturation (f^{-5}) subranges has also been shown to be shifted to lower frequencies when u_* is high (Lenain and Melville, 2017). Sensitivity tests involving calculating mss and equilibrium u_* using an equilibrium frequency range prescribed based on the wave peak frequency (i.e., as done by Banner (1990), centroid frequency, or wave age produce results negligibly different from the above method (not shown). Removing spectra with significant deviations from the f^{-4} shape (Figure 2.3c) also has minimal influence on the overall results.

Near-surface vertical shear is a potential source of uncertainty in surface wave-relative current estimates. ADCP velocity observations below 0.35 m (not shown) demonstrate that the velocity difference between 0.35 m and 15 m depth is typically only around 0.05 ms^{-1}, which is small compared to the range of surface wave-relative currents observed (Figure 2.4c). Kirby and Chen (1989), Zippel and Thomson (2017) and others showed that wave-current interactions are dependent on the spatial scale of the waves. Waves with a frequency between 0.25 and 0.4 s^{-1} will have a wavelength between 10 and 25 m, assuming deep-water wave dispersion. These waves will thus be sensitive to currents on vertical scales of

5-10 m, approximately half their wavelength (Kirby and Chen, 1989; Zippel and Thomson, 2017). Hence, although significant current shear has previously been observed above 0.35 m (e.g., Laxague et al., 2018), this shear near the surface likely only minimally influences wave-current interactions in the selected frequency range.

Wave directions are calculated using directional moments and the maximum entropy method (Lygre and Krogstad, 1986). For consistency with the mss observations, the averaged value in the equilibrium range is used as the wave direction. An energy-weighted average direction was also calculated, but rarely differed by more than 10°from the average direction and thus was not used. mss, equilibrium u_*, and wave direction data are smoothed over 3-hour periods because each individual spectrum consists of only 10 minutes of data (12 degrees of freedom), which is not enough to obtain robust estimates of wave parameters. For consistency, all other atmospheric and oceanic observations are smoothed over 3-hour periods. In general, when winds are higher, waves are more energetic (Figure 2.3a). This leads to greater mss (equation 4). An objective of the present study is to isolate the dominant effect of wind speed on spectral energy in order to evaluate a secondary effect, in which opposing or following surface currents influence spectra and mss through wave-current interactions.

Data collected during a large swell event that occurred from 19-21 Jan 2020 are excluded from further analysis because of the effect of swell waves on the wave directional spectra in the equilibrium range. First, when swell is strong, high frequency wave directions are shifted away from the wind direction, leading to a much larger directional spread. Because wave energy is spread over a wide directional range, it is difficult to determine the direction aligned with the currents that would be expected to be most significantly influenced by wave-current interactions. Second, swell is associated with elevated energy levels between 0.25 and 0.3 s^{-1}, which leads to spectral slopes that are consistently steeper than f^{-4} (Figure 2.3c) and therefore inconsistent with equilibrium theory. Swell modulation of the mid- to high-frequency portion of the wave spectrum, including shifting the transition frequency between the equilibrium and saturation subranges, has previously been observed (Vincent et al., 2019). To exclude conditions where swell significantly influenced high-frequency energy

levels, we only analyze data where the average wave direction in the equilibrium range is $>$ 0°and $<$ 150°, as high frequency wave directions during the swell event were typically 150°to 300°. This criterion eliminates data almost exclusively from the 19-21 Jan 2020 swell event, which comprise <6% of all observations. Because wind direction does not significantly vary in the ATOMIC region, this technique is analogous to the spectral partitioning method of Portilla et al. (2009).

v3 SWIFTs are larger in size and much taller than v4 SWIFTs (Figure 2.2 inset) and thus susceptible to bias at high frequencies due to tilting at high wind speeds. To account for this, mss observations from each v3 SWIFT are corrected using data from v4 SWIFTs. This is done by comparing mss observations from v3 and v4 SWIFTs when a v4 SWIFT was within 20 km of the v3 SWIFT. Linear regressions of wind speed versus mss are then developed to relate v3 and nearby v4 data, and v3 data are corrected by subtracting the difference between the linear fits at each wind speed. Potential uncertainty in the corrections due to spatial variability in the wave field is further discussed in the following paragraph. On average, this correction decreases mss by 1.5×10^{-3}, or 6.2%, with slightly larger corrections at higher wind speeds. A sensitivity test that involved re-calculating mss and u_* without making this correction (not shown) determined that correcting the tilting bias has little effect on the results presented in subsequent sections.

Data processing techniques used to correct wind speed and v3 mss measurements involved using observations from closely spaced platforms to develop a linear relationship used to make corrections. As highlighted in this manuscript, spatial variations likely exist on small scales, so observations from nearby drifters are not always equivalent for individual data pairs. However, this correction method is reasonable for several reasons: First, many pairs of drifters were much closer together than the stated criterion; for instance, v4 drifters used to correct mss from v3 drifters were only 10.8 km apart on average. Second, large amounts of data (n=598) are used to calculate the relationships used to correct v3 mss. Third, variations in mss due to wave-current interactions or other intermittencies in the wave field are not more frequently observed by v3 or v4 drifters (i.e., steeper waves due to opposing

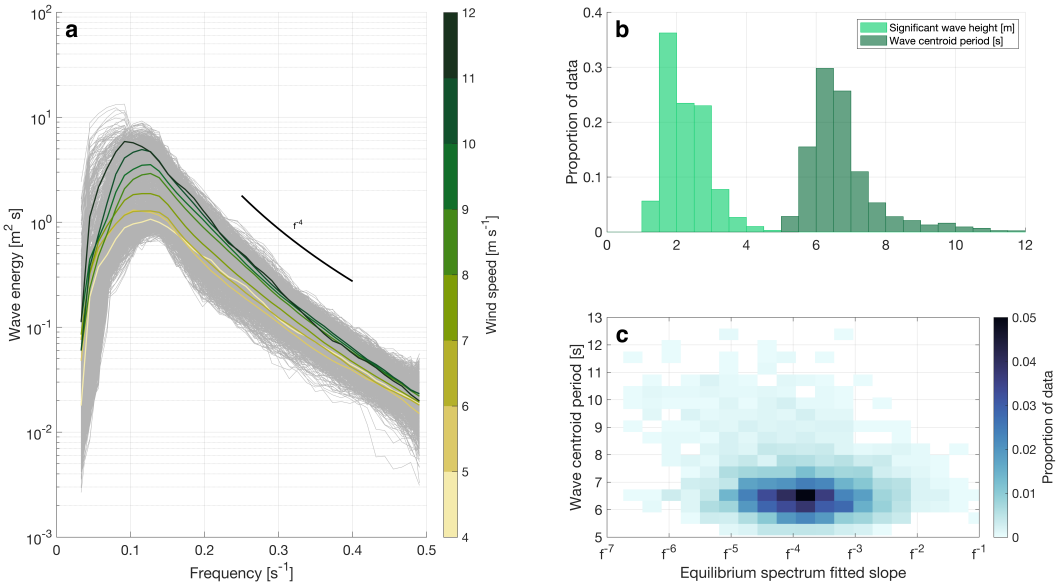

Figure 2.3: (a) Wave spectra observed from v4 SWIFT drifters during both legs of ATOMIC. Energy at individual frequencies was smoothed over a 3-hour time period and in frequency space over 0.059 s^{-1} (grey; n=1156). Colored lines denote average spectra within 1 ms^{-1}-wide wind speed categories. Spectra with a wave direction of $< 0°$or $> 150°$had significant swell input and are excluded. (b) Histograms of significant wave height and wave centroid period from all drifters. (c) Binned scatter plot of wave centroid period vs fitted equilibrium range spectral slope for all drifters.

surface currents would be observed at the same frequency by v3 and v4 drifters). Because of this, the spatial variability between drifters, a source of random error, is smoothed out when constructing regressions. Finally, in the individual case with significant spatial variability highlighted in section 3.2.2, variability is on scales of over 20 km and hence a correction on smaller scales would not influence those results.

2.3 Results

We first evaluate the range of wind, wave, and current conditions observed during ATOMIC (section 3.1). We then evaluate how mss and equilibrium u_* differ across different current

conditions in case studies on varying spatial scales (section 3.2) and collectively in the study area (section 3.3). Results are reported in section 3.2 in terms of mss to highlight the effect of wave current interactions on wave slope, while results are discussed in section 3.3 in terms of u_* to highlight the effects on friction velocity and air-sea momentum flux. We reiterate that reported mss and u_* are directly proportional assuming that an equilibrium spectrum exists: if $f_{max} - f_{min} = 0.15\ s^{-1}$, $\beta = 0.012$, and $I(p) = 2.5$, u_* will be higher than mss (normalized by frequency width) by exactly a factor of 13.0 ms^{-1} (equation 5).

2.3.1 Wind, Wave, and Current Conditions during ATOMIC

Wind directions during ATOMIC were typically from the east or northeast following the prevailing trade winds. Wind speeds were variable: observed values ranged from 3.7 ms^{-1} to 13.0 ms^{-1} with a mean of 8.2 ms^{-1} and a standard deviation of 1.6 ms^{-1} (Figure 2.4d). Variations in wind speed led to variations in significant wave height. Significant wave heights averaged 2.3 m with a standard deviation of 0.6 m (Figure 2.3b), but were elevated to over 4 m during the swell event on 19-21 Jan 2021. Significant wave height was positively correlated with wave period; a mean wave centroid period of 6.8 s was observed, but this value increased to over 9 s during the swell event. As discussed previously, we exclude data from this period of time. Wave directions in the equilibrium frequency range were within $\pm 20^\circ$ of the wind direction 78% of the time (Figure 2.4b). Surface ocean current directions were usually aligned with the wind and waves, but had significantly greater variability. Currents were westward and aligned (within $\pm 90^\circ$) with the waves 68% of the time (Figure 2.4a-c). Currents opposed the waves ($> |90^\circ|$ angle between wind and wave directions) 32% of the time. Current speeds were on average 0.17 ms^{-1}, with a standard deviation of 0.11 ms^{-1}. The vector component of the current aligned with the waves (i.e., the wave-relative current) varied between -0.24 ms^{-1} and 0.47 ms^{-1}, with an average of 0.07 ms^{-1} and a standard deviation of 0.12 ms^{-1}.

As discussed previously, SWIFT drifters are Lagrangian platforms which follow the surface currents (with small additional contributions from wind slip and Stokes drift). Drifters often made loops and turns due to current variability on timescales of under 24 hours (e.g.,

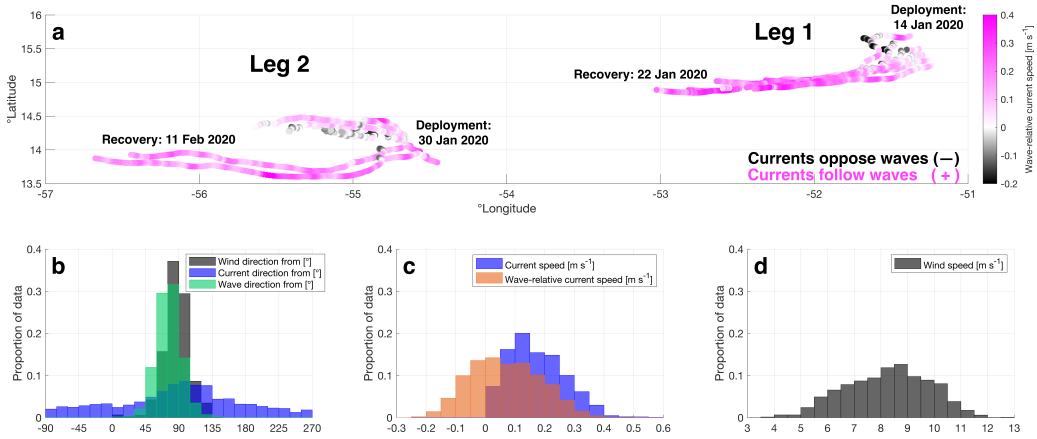

Figure 2.4: (a) Drift tracks of all SWIFT drifters during both legs of ATOMIC. Colors represent the component of the current vector aligned with the waves. Histograms of data from all drifters: (b) wind (v3 only), wave, and current direction (note that green-gray indicates overlap of wind and wave directions, dark blue indicates overlap of wind and current directions, light blue-green indicates overlap of wind and wave directions, and dark blue-green indicates overlap of wind, wave, and current directions); (c) current and wave-relative current speed; (d) wind speed

see Figure 2.5a). This is considerably shorter than the inertial period, so these features are likely fronts or filaments rather than inertial oscillations. Surface current variability is especially apparent during Leg 2: Currents were slower and highly variable in the northern region with four drifters, and faster and aligned with the wind in the southern region with two drifters (Figure 2.4a).

2.3.2 Case studies

Case 1: Small-scale current loop

Two SWIFTs drifted towards the southwest in the southern part of the study region for a 72 hour period from 0000 UTC on 2 February 2020 to 0000 UTC on 5 February 2020, during the second set of drifter deployments. During this period of time, two other drifters made a clockwise reversing turn in an area of cooler water to the north, on the scale of 10

km. While all drifters generally drifted southwestward, shifts in current direction lasting 12-24 hours caused them to briefly drift eastward. This resulted in the observed loops, on scales of less than 10 km, in the drift tracks at 14.25°N and 54.82°W in Figure 2.5a. Wind speeds observed by the southern two drifters steadily decreased from 9 to 4 ms^{-1} throughout most of the 72-hour period. Wind speeds observed by the northern two drifters were steady around 4-6 ms^{-1} for the first 48 hours, before increasing to 7-9 ms^{-1} for the remainder of the time period. Throughout the domain, wind and waves were consistently from the northeast without changing direction (Figure 2.5a). This is expected in a region with prevailing trade winds.

Because wind and wave directions were relatively constant, eastward currents correspond to conditions where the currents and waves were in opposite directions, as seen by the black markers in Figure 2.5. When currents opposed waves, mss was considerably higher than when currents were aligned with the waves during similar wind conditions (Figure 2.5b). Specifically, average mss at wind speeds between 5 and 7 ms^{-1} was 9% higher in opposing current conditions. At wind speeds between 4 and 5 ms^{-1}, this difference was 20%. Differences were much smaller between 7 and 9 ms^{-1}, although mss was still greater in wave-opposing conditions compared to wave-following conditions in all five bins. The small difference in mss between current conditions at wind speeds over 7 ms^{-1} appears to be because wave-opposing currents were much weaker in these bins than below 7 ms^{-1} winds (i.e., the black points in Figure 2.5b are much lighter at higher winds, denoting only very weakly wave-opposing currents). The average difference in wave-relative current between the wave-following and wave-opposing conditions (pink and black lines in Figure 2.5b) was 0.20 ms^{-1}, which at average wind speeds is expected to be associated with a difference in mss of 3.3% due to the difference in relative winds. This is shown by the difference in u_* (assumed to be proportional to the difference in mss) between colored lines in Figure 2.1a. Thus, although differences were not statistically significant at the 95% confidence level except in the 4-5 ms^{-1} bin (Figure 2.5b), the observed mss still differed by a much greater amount between current regimes than expected from relative winds alone. This suggests

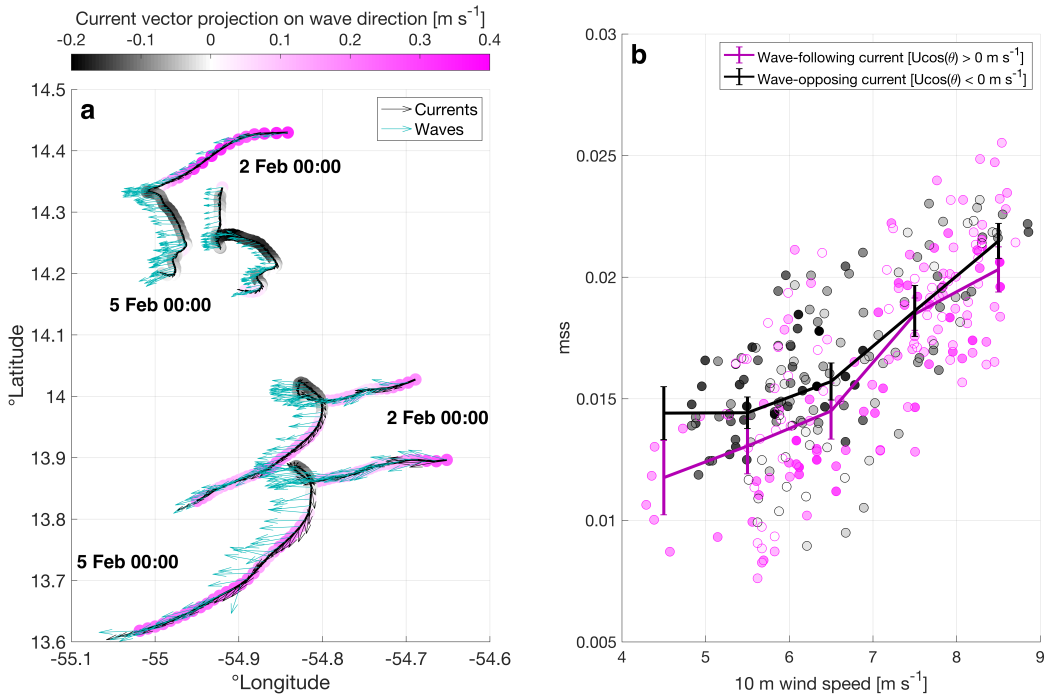

Figure 2.5: SWIFT observations from Case 1. (a) Drift tracks. Colors represent the component of the current vector aligned with the waves, black quivers represent the current direction, and cyan quivers represent the wave direction. (b) mss vs. wind speed for four SWIFT drifters from 2 Feb 2020 0000 UTC to 5 Feb 2020 0000 UTC during leg 2 of ATOMIC. Lines denote averages in 1 ms^{-1}-wide wind speed bins, separated by the wave-relative current ($Ucos\theta$). Points are colored by the wave-relative current, with point outlines denoting whether $Ucos\theta < 0$ (black) or $Ucos\theta > 0$ (pink). All plotted bins contain a minimum of 10 data points.

that wave-current interactions elevated (suppressed) wave slopes while the surface currents were opposing (following) the waves.

Case 2: 30-50 km front

Three SWIFTs drifted southwestward during a 48-hour period from 15 Jan 2020 0800 UTC to 17 Jan 2020 0800 UTC near the start of leg 1 of ATOMIC. A ocean temperature front existed between the southernmost and two northern drifters, as evidenced by a spatial difference

in ocean temperature of about 0.3°C (Figure 2.6b) across 30-50 km. Currents were also considerably faster south of the front, as seen by the long drift track of the southernmost drifter (Figure 2.6a). Unlike the previous case study, wind speeds were steady at 8-10 ms^{-1} throughout the domain.

Because wind speeds only varied by around 2 ms^{-1} during this case study, we evaluate the variability in mss using histograms of wind speed, wave-relative current, mss, and ocean temperature in two wave-relative current regimes: wave-following currents and wave-opposing currents (Figure 2.7). Wind speeds were, on average, slightly higher when currents followed the waves (Figure 2.7e). Despite the stronger winds, average mss was considerably lower in these wave-following current conditions (Figure 2.7g). On the other hand, mss was relatively high, often near 3.0×10^{-2}, when currents opposed the waves (Figure 2.7c). These results demonstrate that in this case with nearly invariant winds, wave-relative currents were the primary driver in modulating mss. However, Figure 2.7g demonstrates that intermittent stronger winds also occasionally elevate mss: several points with wind speeds greater than 10 ms^{-1} and mss greater than 0.03 were observed in wave-following current conditions where currents would not be expected to steepen waves. The near-surface ocean temperatures associated with current regimes (Figures 2.6b, 2.7d,h) show that wave-following currents were almost exclusively observed south of the temperature front, while opposing currents were more commonly observed by the northern two drifters. These results suggest that the mesoscale temperature front coincided with a front in surface currents that led to spatial variability in wave-current interactions.

2.3.3 Synthesis of all data

Figure 2.8 shows the average observed mss and u_*, computed from equation 3 using the equilibrium range of the wave spectra, binned by wind speed and separated by wave-relative current conditions for all SWIFT observations during ATOMIC. u_* derived from wave spectra is generally consistent with the expected values of Large and Pond (1981). This suggests that wind speed and surface stress can be predicted from wave spectra alone and supports the

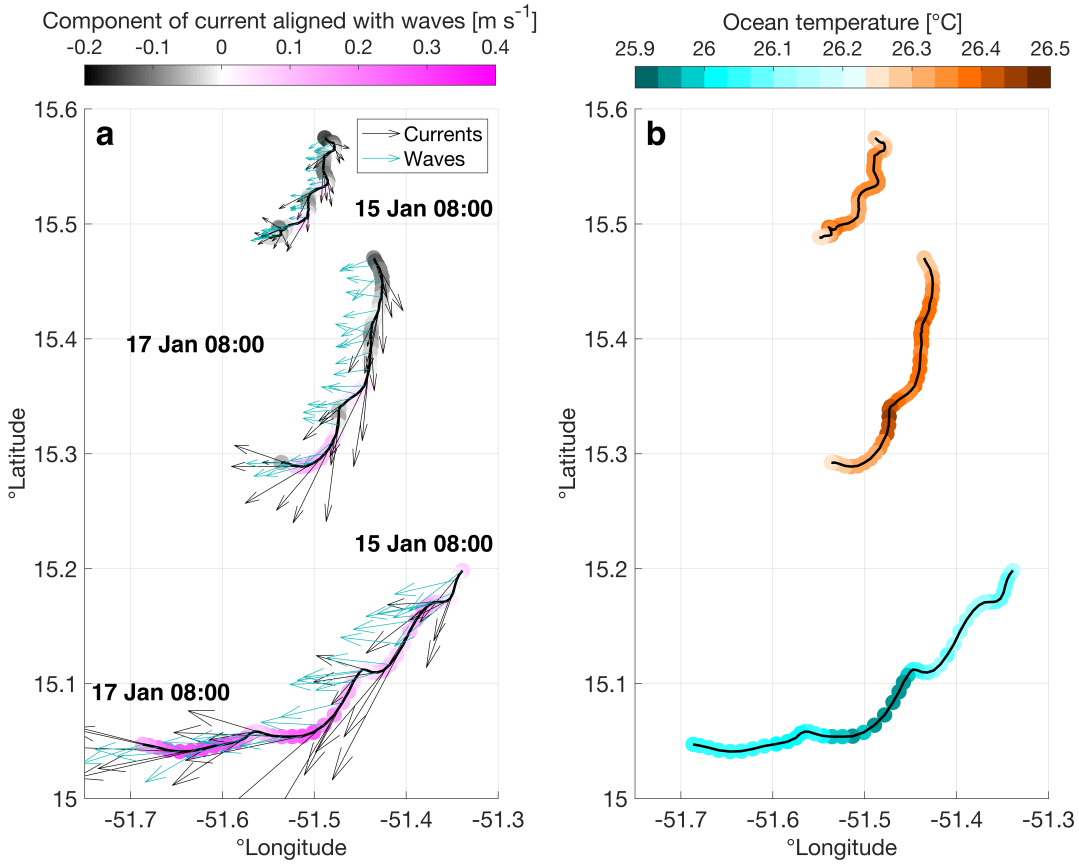

Figure 2.6: SWIFT observations from Case 2, collected from 15 Jan 2020 0800 UTC to 17 Jan 0800 UTC during leg 1 of ATOMIC. (a) Drift tracks. Colors represent the component of the current vector aligned with the waves, black quivers represent the current direction, and cyan quivers represent the wave direction. For clarity, quivers are only plotted every 2 points (hours). (b) Drift tracks. Colors represent near-surface ocean temperature in the top 0.5 m.

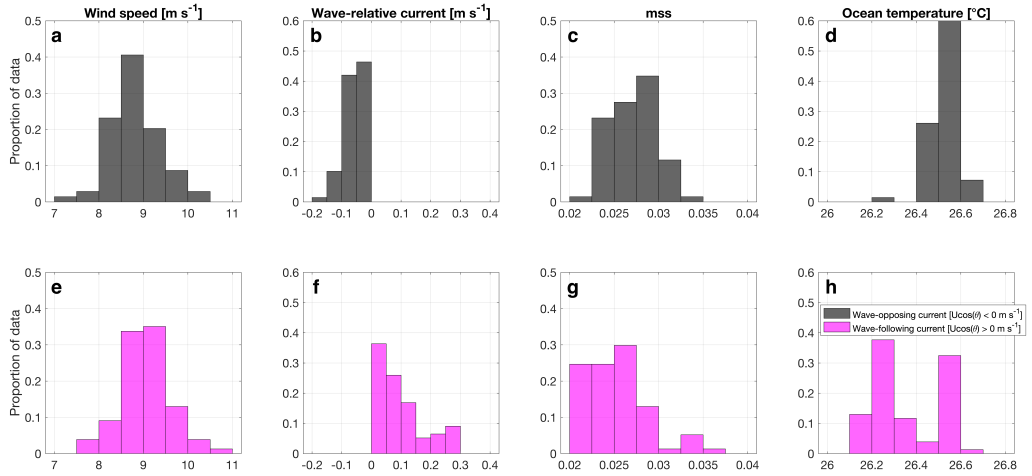

Figure 2.7: Histograms of SWIFT observations from Case 2: (a,e) wind speed, (b,f) wave-relative current, (c,g) mss, and (d,h) ocean temperature for three SWIFT drifters from 15 Jan 2020 0800 UTC to 17 Jan 0800 UTC during leg 1 of ATOMIC. Colors represent categories of the wave-relative current: black denotes wave-opposing currents ($Ucos\theta < 0\ ms^{-1}$; n=69) and pink denotes wave-following currents ($Ucos\theta > 0\ ms^{-1}$; n=77).

findings of Voermans et al. (2020). u_* generally increases as wave-relative currents decrease (i.e., currents are more wave-opposing). The differences in average mss and u_* between wave-relative current conditions were statistically significant at the 95% level at most but not all wind speed bins. This may be due to the fact that wind speeds sometimes differed between current conditions even within bins; i.e., slightly lower wind speeds observed during wave-opposing current conditions may partially cancel out the effect of currents increasing u_*. The variability in u_* between different current conditions generally increases with increasing wind speed, which is consistent with the theoretical predictions based on wave-current interactions shown in Figure 2.1b and equations 8 and 9. There are differences in u_* between different levels of wave-following currents, which suggests that wave-current interactions may be important even when wave-opposing currents are not present, provided that spatial variability exists.

To quantify the effect of wave-current interactions, it is necessary to isolate the effect of

currents from the dominant effect of wind speed on u_*. A multiple linear regression assesses the variability in u_* independent of wind speed: assuming u_* depends only on wind speed and wave-relative current, the effect of currents and wind speed on u_* can be individually quantified. This regression is described by Equation 10,

$$u_* = x + y\ U_{10} - z\ Ucos(\theta), \tag{2.10}$$

which shows the average individual contributions of wind speed (U_{10}) and wave-relative current ($Ucos(\theta)$) to u_*. Using u_* inferred from the wave spectra and U_{10} and $Ucos(\theta)$ from the SWIFT observations, we find that $x = -0.043 \pm 0.006$ (standard error), $y = 0.041 \pm 0.001$, and $z = -0.084 \pm 0.009$ ($R^2 = 0.66$). The method used to obtain u_*, using wave spectra calculated from 10-minute segments of data, is likely responsible for the relatively low R^2 value, as robust wave statistics cannot be obtained from short bursts. Physically, y and z are the contributions of U_{10} and $Ucos(\theta)$ to u_*. The offset x is likely an artifact of the differences between the moderate- and low-wind relationship between U_{10} and u_* (Edson et al., 2013), with additional contribution from the assumption of constant β and $I(p)$ in calculations of u_*. We note that using multiple linear regression to calculate equation 10 inherently assumes that U_{10} and $Ucos(\theta)$ are uncorrelated. A linear regression between these variables shows only a very weak positive correlation ($R^2 = 0.04$), so the use of multiple linear regression to isolate wind speed is reasonable. Equation 10 demonstrates that the variation in u_* across different current conditions is greater than what is expected from the current-relative wind alone. That is, the observed spread in u_* (Figure 2.8) is greater than the prediction shown in Figure 2.1a. A wave-relative current change of 0.1 ms^{-1} was, on average, associated with a change of 0.0084 ms^{-1} in u_* (compared to 0.0035 ms^{-1} expected from equation 2 and Figure 2.1a). Equation 10 suggests that the range of observed values of wave-relative current of approximately 0.7 ms^{-1} will lead to variations in mss and u_* of 20%, at moderate wind speeds of 8-9 ms^{-1} (compared to 8% expected from equation 2 and Figure 2.1a). However, wave-relative currents did not often vary by this amount at constant wind speeds; the middle

80% of observations within wind bins typically had 0.3-0.35 ms^{-1} variability in wave-relative currents. Hence, the true typical variation in mss and u_* is likely around 10%.

Another method of quantifying the influence of surface currents on u_* is to calculate the difference between the observed u_* and predicted value from the Large and Pond (1981) relationship, which doesn't incorporate wave effects, and determine a relationship between this residual u_* and the wave-relative current. This analysis yielded similar results as the multiple linear regression, with a slightly smaller dependence of wave-relative current on u_*: residual u_* decreased by 0.0057 ms^{-1} for every 0.1 ms^{-1} increase in wave-relative current. These analyses demonstrate that in the ATOMIC study area, which has consistent and strong wave-following currents, small-scale spatial variations in surface currents may drive wave-current interactions and cause significant increases or decreases in u_* and mss due to wave steepening or flattening, respectively. This is likely also applicable to other regions of the ocean with similar wind speeds and moderate current variability.

These findings support the hypothesis that wave-current interactions in the open ocean significantly modify u_* when currents strongly follow or oppose the waves. However, the overall variation in observed u_* is less than the expected spread for a single theoretical wave; i.e., there is a greater spread in u_* at a given wind speed in Figure 2.1b than in Figure 2.8. We expect that this discrepancy is primarily due to the directional spread of waves. Calculated from directional moments obtained from SWIFT onboard processing, average wave directional spread in the equilibrium frequency range is around 45°, with typical fluctuations up to 20°. The spread may partially result from scattering effects from submesoscale current velocity variations (Smit and Janssen, 2019), which were commonly observed in this area. The large wave directional spread indicates that a significant portion of the wave spectrum will not be directly aligned with the surface currents when the surface currents oppose or follow the average wave direction. Thus, the net effect of currents on wave steepening or flattening will be lower than expected for a single theoretical wave. The assumption of a constant $I(p)$ in the calculation of u_* (equation 3) may also have contributed to the weaker signal, as directional spreading may co-vary with the alignment and direction of the waves.

In addition, nonlinear interactions and contributions from the lower frequency portion of the spectrum (Vincent et al., 2019) may have smoothed out differences in u_* between current regimes.

To assess the contribution of wave-current interactions to air-sea momentum flux, we calculate momentum flux from equilibrium u_* and ρ_a observations using equation 1. The physical idea is that mss is a proxy for surface roughness, which is directly related to the wind friction velocity and the momentum flux. ρ_a was determined from air temperature, air pressure, and relative humidity observations on the v4 SWIFTs. Because relative humidity observations were not available from the v3 SWIFTs, meteorological observations made on the NOAA Ship Ronald H. Brown (Thompson et al., 2021) were used to estimate ρ_a for these drifters. This approximation had a negligible effect, as ρ_a varied minimally (mean ρ_a on the ship was 1.172 $kg\ m^{-3}$ with a standard deviation of 0.003 $kg\ m^{-3}$). Momentum flux calculated using u_* from wave spectra and equation 1 will hereinafter be referred to as τ_{waves}. We note that using τ_{waves} as a measure of momentum flux is contingent on the assumption that wind-wave equilibrium is valid and spectra follow the theoretical f^{-4} shape; see section 4.3 for a discussion. Figure 2.9a compares wind speed and τ_{waves}: τ_{waves} varies significantly between current conditions for a given wind speed. These differences are statistically significant at moderate wind speeds over 8 ms^{-1}. Equation 11,

$$\tau_{waves} = X + Y\ U_{10} - Z\ Ucos(\theta), \tag{2.11}$$

represents the dependence of τ_{waves} on wind speed and wave-relative current. Performing a multiple linear regression, we find that $X = -0.116 \pm 0.004$ (standard error), $Y = 0.028 \pm 0.001$, and $Z = -0.061 \pm 0.007$ ($R^2 = 0.61$). As with Equation 10, the short 10-minute sampling window likely contributed to uncertainty in these values. X is an offset and Y and Z are the contributions of U_{10} and $Ucos(\theta)$ to τ_{waves}. τ_{waves} varies by 0.0061 Nm^{-2} on average for a 0.1 ms^{-1} change in wave-relative current. This equates to a 40% variation across the entire 0.7 ms^{-1} range of observed wave-relative currents at moderate wind speeds

of 8-9 ms^{-1} (equation 11). However, as mentioned above, the true variability at a given wind speed is likely much less than this value, as wave-relative currents typically only varied by a smaller amount. For instance, if wave-relative currents varied by 0.3 ms^{-1}, τ_{waves} would be expected to vary by approximately 17% at 8-9 ms^{-1} winds. This is comparable to the change in momentum flux that would be associated with a wind increase or decrease of 0.7 ms^{-1}, according to the Large and Pond (1981) relationship.

Previous studies have shown that wave statistics, including mss, are improved when spectra are normalized by the wave directional spread (Banner et al., 2002; Schwendeman and Thomson, 2015). We recalculated mss from the wave spectra after normalizing spectra by the directional spread ($\Delta\theta$), in addition to the aforementioned normalization by the equilibrium frequency range width: normalizing by $\Delta\theta$ had a minimal effect on the magnitude of mss; however, it increased the spread in mss between different wave-relative current conditions slightly (not shown). Normalizing by $\Delta\theta_2$, the directional spread calculated with the second-order moments of the wave spectra (Thomson et al., 2018), increased the magnitude of mss but did not affect the spread in mss between different current conditions. In short, variance in mss across different wave-relative current conditions exists whether or not spectra are normalized by $\Delta\theta$ or $\Delta\theta_2$. Hence, mss only normalized by the frequency width are shown.

2.4 Discussion and Conclusions

2.4.1 Temporal and lateral variations in surface currents

The SWIFT observations demonstrate that both temporal and spatial variations in currents exist in the trade wind region encompassing the ATOMIC study area. For instance, case study 1 (Figure 2.5) shows variations in current speed and direction owing to a combination of increasing or decreasing wind speeds and larger-scale ocean variability, which modified currents throughout the area where drifters were deployed. That is, all drifters observed similar surface current speed and direction at a given time. On the other hand, case study 2 (Figure 2.6) exhibited spatial variations in surface currents, as winds were relatively steady

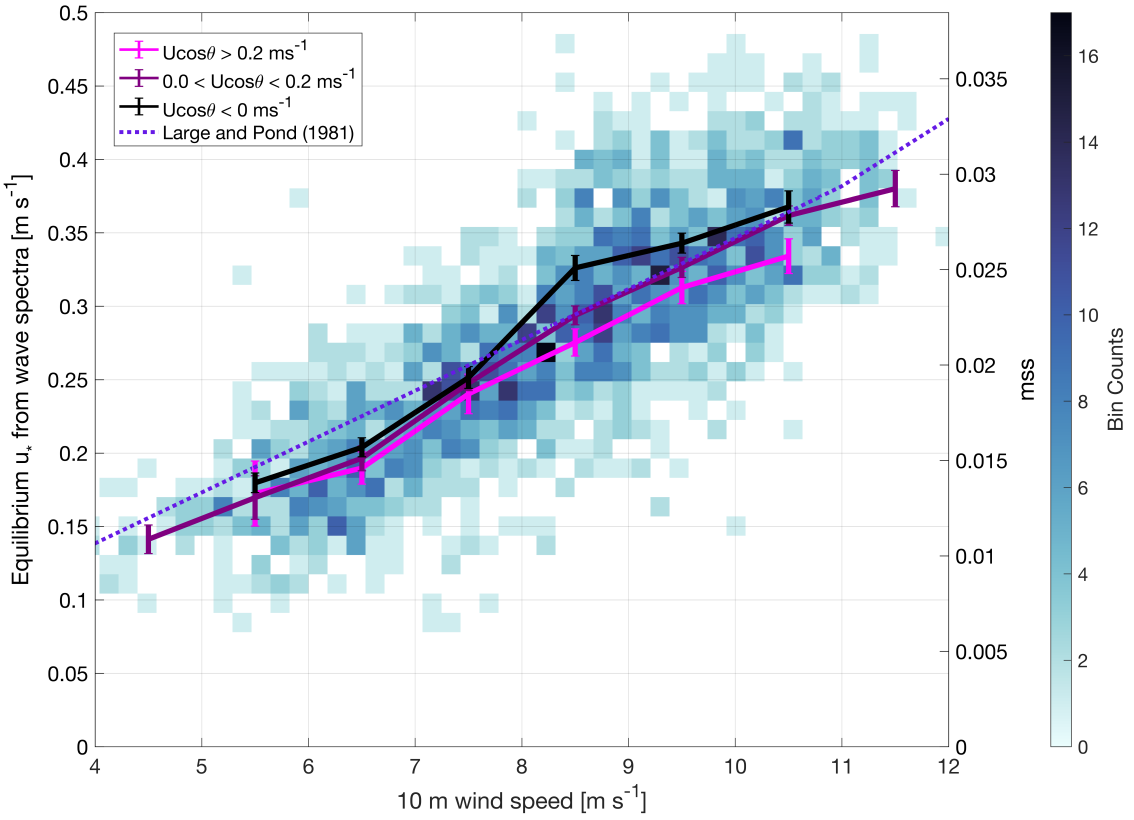

Figure 2.8: Equilibrium u_* and mss versus wind speed for all SWIFT data during both legs of ATOMIC. Lines denote averages in 1 ms^{-1}-wide wind speed bins, colored by the wave-relative current ($Ucos\theta$). Error bars represent 95% confidence intervals around the mean of each bin. Blue shading represents the number of observations near a given wind speed and mss or u_*. All plotted bins contain a minimum of 10 data points. The dotted purple line shows expected values of u_* calculated from the relationship in Large and Pond (1981).

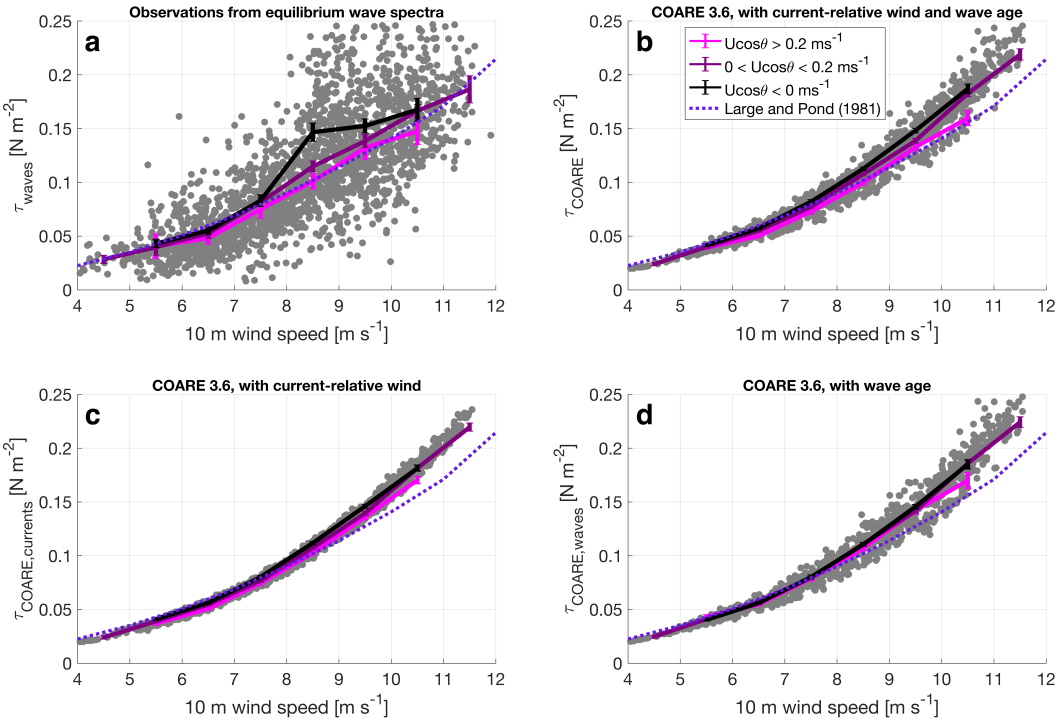

Figure 2.9: Momentum flux vs. wind speed calculated from (a) equilibrium u_* inferred from wave spectra for all SWIFT data and (b-d) version 3.6 of the COARE algorithm for v4 SWIFT data, during both legs of ATOMIC. COARE 3.6 inputs included (b) observed surface currents and waves, (c) observed surface currents but not waves, and (d) observed waves but not surface currents. Lines denote averages in 1 ms^{-1}-wide wind speed bins, colored by the wave-relative current ($Ucos\theta$). Error bars represent 95% confidence intervals around the mean of each bin. All plotted bins contain a minimum of 10 data points. Grey points represent wind speed and momentum flux observations, smoothed over a 3-hour period. The dotted purple line shows expected values calculated using Equation 1, with u_* determined by the relationship in Large and Pond (1981) and using the mean ρ_a observed by the Ronald H. Brown.

throughout the domain but current speed and direction varied between drifters; i.e., drifters at different locations did not observe similar surface currents at the same point in time. This suggests that there is lateral shear in surface currents, which presumably drives lateral variability in waves and air-sea fluxes. For instance, at 1200 UTC on 15 January 2020 near the beginning of case study 2, the southern two drifters are roughly 30 km apart, with wave-relative currents 0.17 ms^{-1} higher (more wave-following) at the location of the southernmost drifter (Figure 2.6). u_* and τ_{waves} are 0.060 ms^{-1} and 0.043 Nm^{-2} larger at the location of the central drifter (not shown). This implies that an average lateral wave-relative current shear of just under 0.006 $ms^{-1}km^{-1}$ is responsible for average lateral variations of 0.002 $ms^{-1}km^{-1}$ and 0.0015 Nm^{-2} in u_* and τ_{waves}. We note that these shear estimates are highly dependent on the scale of the observations; that is, the spacing between SWIFT drifters. For instance, if a temperature front is sharp, shear will be much stronger in the small region near the front and weaker away from it. This is an important caveat in the context of wave-current interactions: these wave-current interactions only will occur if waves propagate across a region with spatial current variations; otherwise, any change in wave properties is likely due to the current-relative wind alone. Nevertheless, the significant variations observed by drifters across fronts imply that shear is present at some locations between the drifters. This, along with the small-scale features highlighted in case 1, demonstrates that spatial variations of wave-current interactions are a major source of uncertainty in studies assuming that currents are uniform on submesoscales or mesoscales. That is, surface currents influence mss, u_*, and momentum flux both when currents are spatially variable and when currents are spatially homogeneous but temporally variable.

2.4.2 Applications to air-sea interaction and fluxes

The latest version (3.6) of the widely-used Coupled Ocean-Atmosphere Response Experiment (COARE) bulk flux algorithm (Fairall et al., 2003; Edson et al., 2013) utilizes a wave model (Banner and Morison, 2010) to parameterize the effect of wave age on surface roughness and stress through the dominant wave phase speed (i.e., speed at the spectral peak),

significant wave height, and wind speed, but does not consider the effects of surface currents on waves other than through changes in the current-relative wind speed (equation 2). Because the results from section 3 indicate that wave-current interactions significantly modulate momentum flux when spatial variability exists, we compare COARE 3.6 output, including and excluding parameterizations of the current-relative wind and wave age, to observations to evaluate the significance of wave-current interactions in modulating fluxes and gain insight into the effectiveness of COARE 3.6 parameterizations of momentum flux when surface currents are variable.

Momentum flux calculated using the COARE algorithm (τ_{COARE}), wind speed, surface current, and wave conditions observed by the SWIFTs and other atmospheric conditions observed at the Ronald H. Brown, is shown in Figure 2.9b. Figure 2.9c shows momentum flux calculated using COARE 3.6 and prescribing observed surface currents but not waves (i.e., identical to 2.9b except without wave height and peak period prescribed as an input). Figure 2.9d shows momentum flux calculated using COARE 3.6 and prescribing observed wave conditions but not surface currents. Wave phase speeds input into COARE were calculated from the observed wave peak period and deep-water wave dispersion relation. Even though centroid period is a more stable parameter that is independent of the frequency spacing of the spectra, we use peak period as the dominant wave period input into COARE because the current version of the COARE algorithm was developed using peak period. v3 and v4 SWIFT peak periods are inconsistent because of the tilting bias discussed earlier, so only v4 SWIFT data were used to calculate momentum flux using COARE.

Figures 2.9b-d indicate that the variability of τ_{COARE} at a given wind speed is due to both variations in current-relative wind (Figure 2.9c) and wave age (Figure 2.9d). At wind speeds under 10 ms^{-1}, there is a larger difference between current conditions when only current-relative wind is prescribed (Figure 2.9c) than when just wave age is prescribed (Figure 2.9d). This indicates that the spread in τ_{COARE} between different wave-relative current conditions (Figure 2.9b) is largely the result of current-relative wind variations rather than waves, although waves do appear to have a significant impact at the highest wind speeds.

The variations in τ are much larger in the observations (gray points in Figure 2.9a) than in COARE (gray points in Figures 2.9b,c,d). This results from both variability in waves and turbulence and the inconsistencies in the assumptions used to calculate τ. Specifically, variations in the wave spectral slope (Figure 2.3c), the short 10-minute duration over which wave spectra were calculated from, and the assumptions of constant β and $I(p)$ all contribute uncertainty to τ estimates and result in inconsistencies between observed τ and COARE estimates or the Large and Pond (1981) parameterization. Furthermore, COARE is designed to represent the mean stress observed under given conditions rather than capture turbulent fluctuations inherent in the real world. However, the variability in bin-averaged τ between current conditions estimated using COARE (spread between lines in Figure 2.9b) is also much smaller than in the observations (spread between lines in Figure 2.9a). Because random error will be averaged out, we conclude that the smaller spread in COARE estimates is likely not due to the sources of uncertainty mentioned above and instead may be a result of current variability.

Table 2.1 shows mean τ within individual wind speed bins in Figures 2.9a and 2.9c. Because Figure 2.9c does not consider waves, the difference in τ between Figures 2.9a and 2.9c is an estimate of the influence of waves on momentum flux. At wind speeds above 8 ms^{-1}, τ_{waves} varies by 12.7% to 36.8%, while τ_{COARE} only varies by 6.3% to 8.6% (Figure 2.9, Table 2.1). At these wind speeds, the difference between τ_{waves} and τ_{COARE} within individual bins is at least 6%, suggesting that wave-current interactions may be responsible for variations in τ of at least 6%. The variability in τ in the 8-9 ms^{-1} wind speed bin suggests significantly greater variability; however, the cause of this is unclear. One possibility is the presence of greater spatial variability in wave-relative currents when winds are moderate.

We note that the wave age parameterization in COARE, which does not incorporate wave-current interactions, reproduces some of the spread between current conditions at wind speeds above 10 ms^{-1} (Figures 2.9b,d). This may imply that wave-current interactions are not solely responsible for this variability. However, the spread is not reproduced at slightly lower wind speeds: τ_{COARE} shown in Figures 2.9b and 2.9c are typically within a few percent

at all wind speeds below 10 ms^{-1} (Table 2.1). At wind speeds below 8 ms^{-1}, τ_{waves} is only associated with a small amount of additional variability compared to τ_{COARE} (Figure 2.9, Table 2.1), which suggests that variations in τ between different wave-relative current conditions at low wind speeds are primarily the result of current-relative winds rather than wave-current interactions.

Wave-current interactions are expected to have a second-order role in modulating the spatial variations of physical processes in addition to the air-sea momentum flux, including near-surface turbulence, gas transfer, and air-sea sensible, latent, buoyancy, and net heat fluxes. As discussed earlier, steeper wave slopes on one side of a front have previously been observed to be associated with enhanced wave breaking (e.g., Romero et al., 2017, 2020, and others), a process which elevates near-surface turbulent kinetic energy (TKE) dissipation rates (e.g., Agrawal et al., 1992; Craig and Banner, 1994; Terray et al., 1996; Thomson, 2012, and others) and air-sea gas transfer velocities (e.g., Keeling, 1993; Asher et al., 1996; Melville, 1996, and others). Thus, the observed submesoscale spatial variations in mss suggest that air-sea gas exchange and near-surface turbulence vary on the same spatial scales of kilometers to tens of kilometers. Air-sea heat fluxes are influenced by momentum fluxes and would also be expected to vary on the same spatial scales: Assuming standard bulk flux relationships between τ, the drag coefficient C_D, the transfer coefficients of heat and moisture, and the surface heat flux (as shown in Fairall et al., 1996), and assuming that only surface stress is modified and other terms remain the same, a 6% uncertainty in bulk momentum flux will lead to an uncertainty of approximately 3%, or 6 Wm^{-2}, of the air-sea sensible plus latent heat flux under average conditions observed during ATOMIC. As mentioned in section 3.3, a direct comparison between τ_{waves} and direct or parameterized flux estimates (i.e., τ_{COARE}) requires assuming that wave spectra used in the calculation of τ_{waves} follow a f^{-4} shape and wind and waves are in equilibrium. Time- and frequency-averaged spectra had a slope close to f^{-4} (Figure 2.3a,c), although small deviations from the expected f^{-4} shape occurred in a considerable number of spectra. Regardless, mss calculated from the spectra (directly proportional to u_* used to calculate τ_{waves}, as seen in equation 5) are indicative of the surface

Table 2.1: Mean observed and expected momentum flux (τ, in Nm^{-2}) within wind speed bins, as shown in Figure 2.9a and Figure 2.9c. "Current effect" refers to the percent difference between mean values of τ in the $Ucos\theta < 0$ vs $Ucos\theta > 0.2$ ms^{-1} wave-relative current bins

Wind speed	5-6 ms^{-1}	6-7 ms^{-1}	7-8 ms^{-1}	8-9 ms^{-1}	9-10 ms^{-1}	10-11 ms^{-1}
τ_{waves}, $Ucos\theta < 0$	0.0431	0.0554	0.0832	0.1469	0.1527	0.1677
τ_{waves}, $0 < Ucos\theta < 0.2$	0.0399	0.0528	0.0815	0.1149	0.1386	0.1667
τ_{waves}, $Ucos\theta > 0.2$	0.0406	0.0483	0.0751	0.1012	0.1324	0.1477
τ_{COARE}, $Ucos\theta < 0$	0.0410	0.0564	0.0802	0.1117	0.1460	0.1814
τ_{COARE}, $0 < Ucos\theta < 0.2$	0.0391	0.0546	0.0766	0.1073	0.1395	0.1814
τ_{COARE}, $Ucos\theta > 0.2$	0.0370	0.0507	0.0745	0.1025	0.1362	0.1703
Current effect in τ_{waves}	6.0%	13.7%	10.2%	36.8%	14.2%	12.7%
Current effect in τ_{COARE}	10.3%	10.6%	7.4%	8.6%	7.0%	6.3%

roughness and thus will modulate air-sea momentum fluxes, even if wind-wave equilibrium is not strictly satisfied.

Wind directions are relatively invariant in the ATOMIC study area. Many other areas of the world ocean have similarly consistent wind directions, including the tropics and midlatitudes with prevailing trade winds and westerlies, respectively. Because of this, the observed influence of current variability on waves and momentum flux in the ATOMIC region, as well as the hypothesized influence of current variability on near-surface turbulence, gas exchange, and heat fluxes, is likely applicable to other areas; i.e., wave-current interactions may be globally significant in modulating small-scale variability in waves and air-sea interaction even outside of locations with large wind or current variations. This finding is of particular relevance to model simulations that do not account for small-scale spatial variations in surface currents, or those that do not incorporate wave-current interactions at all or comprehensively into air-sea flux parameterizations. Due to greater small-scale spatial variability in coastal areas, the influence of wave-current interactions on air-sea fluxes is likely significantly greater here, along with locations that have stronger mesoscale and submesoscale eddy activity such as near strong western boundary currents like the North Brazil Current region to the south of the ATOMIC study area (Figure 2.2).

2.5 Conclusions

Typically, in the northwest tropical Atlantic trade wind region during winter, currents follow the waves at 0 to 0.2 ms^{-1}. Conditions where currents were in the opposite direction as the waves occurred approximately 32% of the time, preferentially when wind speeds were below 8 ms^{-1}. Opposing wave-relative currents were never greater than 0.24 ms^{-1}. The two case studies demonstrate that surface current speed and directional variability exists on a wide range of spatial scales, from a few kilometers (Figure 2.5) to the scales of mesoscale features (Figure 2.6), and produces variations in mss and u_* on the same scales.

In conditions where the currents follow the waves (green and blue lines in Figure 2.8), mss and u_* deviate by 10% from conditions where the currents are neutral or wave-opposing (pink and orange lines in Figure 2.8) in moderate wind conditions. Significant variations in mss and u_* also are present across different levels of wave-following current conditions. Variability in mss and u_* is greater than expected from the current-relative wind speed alone (Figure 2.1a), which implies that variability in u_* at constant wind speeds is the result of a combination of the current-relative wind and wave-current interactions. The Doppler shift changes the waves' slopes when currents vary spatially, and these changes in roughness are used to infer changes in momentum flux.

These findings suggest that wave-current interactions are a source of uncertainty in predictions of mss or u_* from either wind speed or current-relative wind speed alone, and predictions of wind speed from u_* such as those by Voermans et al. (2020). Variations in u_* of 10% roughly equate to variations in momentum flux of 20% at a given wind speed (Equation 1). This significant contribution suggests that the inclusion of current-relative winds and wave-current interactions in models and parameterizations is crucial for obtaining accurate estimates of waves, near-surface turbulence, and air-sea heat, gas, and momentum fluxes. Existing parameterizations of waves and surface currents, such as those from version 3.6 of the COARE bulk flux algorithm, do not comprehensively consider the effect of wave-current interactions. Hence, even though the mean flux is still well represented by

these models, they may underestimate variability in air-sea fluxes in the presence of varying surface currents and waves.

Chapter 3

SMALL-SCALE SPATIAL VARIATIONS OF AIR-SEA HEAT, MOISTURE, AND BUOYANCY FLUXES IN THE TROPICAL TRADE WINDS

This chapter has been submitted to *Journal of Geophysical Research: Oceans* as **Iyer, S., K. Drushka, E. Thompson, and J. Thomson. Small-scale spatial variations of air-sea heat, moisture, and buoyancy fluxes in the tropical trade winds**.

Abstract

Observations from two autonomous Wave Gliders and six Lagrangian Surface Wave Instrument Float with Tracking drifters in the northwestern tropical Atlantic during the January-February 2020 NOAA Atlantic Tradewind Ocean-atmosphere Mesoscale Interaction Campaign are used to evaluate the spatial variability of bulk air-sea heat, moisture, and buoyancy fluxes. Sea surface temperature (SST) gradients of up to 0.7°C across 10-100 kilometers frequently persisted for several days. SST gradients were a leading cause of systematic spatial air-sea sensible heat flux gradients, as variations over 5 Wm^{-2} across under 20 kilometers were observed. Wind speed gradients played no significant role and air temperature adjustments to SST gradients sometimes acted to reduce spatial flux gradients. Wind speed, air temperature, and humidity caused high-frequency spatial and temporal flux variations on both sides of SST gradients. A synthesis of observations demonstrated that fluxes were usually enhanced on the warm SST side of gradients compared to the cold SST side, with variations up to 10 Wm^{-2} in sensible heat and upward buoyancy fluxes and 50 Wm^{-2} in latent heat flux. Sensible heat flux varied due to both persistent spatial SST gradients and high-frequency air temperature variations. Latent heat flux was instead mostly driven by air

humidity variability. Atmospheric variability may result from cold pools or high-frequency turbulent fluctuations. Comparisons with 0.05°-resolution daily satellite SST observations demonstrate that remote sensing observations or lower-resolution models may not capture the small-scale spatial ocean variability present in the Atlantic trade wind region.

3.1 Introduction

3.1.1 Importance and previous studies

Fluxes of heat, moisture, and buoyancy between the ocean and atmosphere modulate synoptic to global-scale weather and climate. Despite this importance, uncertainty remains in our understanding of how air-sea fluxes vary across small spatial scales, which are difficult to observe remotely. Much of the existing research on the atmospheric response to spatial ocean variability has utilized satellite observations to assess the influence of ocean mesoscale features on scales of 25 to hundreds of kilometers (e.g., Chelton et al., 2004; O'Neill et al., 2005; Chelton and Xie, 2010; Small et al., 2008; Gaube et al., 2015). These studies show that sea surface temperature (SST) and air humidity gradients across mesoscale features lead to spatial gradients in air-sea heat and momentum fluxes, which modify atmospheric dynamics. For example, heating over the warm side of an SST front destabilizes the atmospheric boundary layer, increasing surface wind speeds through either downward momentum transfer (Wallace et al., 1989) or pressure differences (Lindzen and Nigam, 1987) and inducing atmospheric convection.

Bulk air-sea sensible and latent heat fluxes are typically defined as functions of the SST, air temperature, air humidity, air density, and wind speed (Fairall et al., 1996, 2003), while the air-sea buoyancy flux into the atmosphere is a weighted sum of both the sensible and latent heat fluxes (Stull, 1988). Thus, spatial variations in ocean properties including SST, stratification, and surface wind stress are expected to create spatial variability in air-sea heat, moisture, and buoyancy fluxes. Spatial flux variability has been associated with eddies, fronts, and boundary currents in the field (e.g., Businger and Shaw, 1984; Sweet et al., 1981;

Minobe et al., 2008; Small et al., 2008; Kwon et al., 2010; Kelly et al., 2010) and in large-scale model analyses (Bishop et al., 2017; Small et al., 2019) on a range of spatial scales, including across strong surface current gradients in the subtropical ocean (Friehe et al., 1991; Seo, 2017; Shao et al., 2019) and tropical instability waves in the equatorial ocean (Hayes et al., 1989; Zhang and Mcphaden, 1995; Thum et al., 2002; Seo et al., 2007).

High-resolution model simulations suggest that SST fronts can influence air-sea fluxes and the dynamics of the atmospheric boundary layer across small horizontal spatial scales of hundreds of meters to ten kilometers (Samelson et al., 2006; Lambaerts et al., 2013; Wenegrat and Arthur, 2018; Redelsperger et al., 2019; Sullivan et al., 2020; Samelson et al., 2020; Sullivan et al., 2021; Strobach et al., 2022). The mechanism by which these connections occur is through air-sea heat fluxes: increases or decreases in the sensible and latent heat fluxes on the warm or cold side of a SST front influence the upward buoyancy flux into the atmosphere. The net effect of this is that increased wind stress and deeper atmospheric boundary layers would be expected on the warm ocean sides of fronts (Samelson et al., 2006) as a result of greater vertical velocities and instability in the atmospheric boundary layer. The atmospheric response to ocean variations is also dependent on the relative alignment of the wind and SST front (Samelson et al., 2020; Sullivan et al., 2020, 2021); for instance, air temperature and SST gradients have been shown to be more strongly coupled when winds blow across SST fronts rather than along fronts (Samelson et al., 2020). Unlike with SST gradients on scales of hundreds of kilometers, the atmosphere does not fully equilibrate to small-scale spatial variations in heat fluxes (Small et al., 2019) and thus small scale ocean features can generate persistent air-sea flux variability which has been hypothesized to influence local atmospheric convection and weather patterns (e.g., Redelsperger et al., 2019; Strobach et al., 2022).

The present study will focus on the trade wind region of the tropical Atlantic (Figure 3.1), where extensive research in the context of spatial variability has not been done. The trade winds are characterized by near-constant winds, ocean currents that either follow the wind and waves or counter them due to submesoscale features (Iyer et al., 2022), and relatively

weak SST frontal activity (Figure 1 of Mauzole, 2022). Atmospheric cold pools generate high-frequency (< 1 hour to several hours) variability in wind speed and air temperature in the trade winds (Zuidema et al., 2012; de Szoeke et al., 2017). We aim to evaluate spatial variations of SST and atmospheric parameters on fluxes at scales of tens of kilometers. Because the atmosphere will not fully respond to these mesoscale and submesoscale changes in SST (Small et al., 2019), these spatial SST variations would be expected to create spatial variations in heat fluxes, persist for long periods of time, and in-turn influence atmospheric stability and drive dynamical changes in the atmospheric boundary layer. Establishing that significant heat flux variability exists in the open-ocean trade winds is particularly important because this is not a region associated with boundary currents or coherent mesoscale features and would provide observational evidence that smaller-scale features may influence atmospheric dynamics even away from energetic ocean features. Furthermore, the trade winds are a region that modulates synoptic- to global-scale weather and climate patterns including storm systems, hurricanes and other hazardous weather phenomena, so any observed spatial heat flux variations would suggest that small-scale ocean structure may interact with these larger-scale processes via air-sea fluxes.

Global and regional climate models that resolve mesoscale ocean features show an stronger influence of ocean variability on air-sea interaction (Laurindo et al., 2022) and have reduced biases compared to lower-resolution models (Bryan et al., 2010; Small et al., 2014; Su et al., 2018), including in the tropical Atlantic (Seo et al., 2006). This further suggests submeso- to mesoscale ocean features play a role in the global climate system. Widely-utilized satellite air-sea flux products differ as a result of different spatial and temporal resolution and differences in bulk parameterizations (Table 1 of Yu, 2019). A secondary objective of the present study is to gain insight into the uncertainty of global flux products or models, which resolve air-sea heat, moisture, and buoyancy fluxes on relatively large scales, in trade wind regions. To this end, we make comparisons between high-resolution in situ bulk flux observations and fluxes estimated from a composite satellite SST product.

3.2 Data

3.2.1 Study site and satellite data

The NOAA Atlantic Tradewind Ocean-atmosphere Mesoscale Interaction Campaign (ATOMIC), part of EUREC^{4}A (Stevens et al., 2021), took place in the trade wind region of the northwest tropical Atlantic in January-February 2020 (Figure 3.1). Quinn et al. (2021) present a detailed synopsis of the ATOMIC ship and autonomous platform instruments used in the field campaign, which included various instrument deployments and two cruise legs on the NOAA Ship *Ronald H. Brown*. Moderate ocean current (Iyer et al., 2022) and SST variability exists in this region on scales of tens of kilometers (Figures 3.1,3.2), ultimately resulting from mesoscale activity associated with North Brazil Current eddies (Fratantoni and Glickson, 2002; Ffield, 2005; Fratantoni and Richardson, 2006), the cascade of mesoscale to submesoscale energy (e.g., Capet et al., 2008), and, in boreal spring through fall, river outflow from the South American continent. The observed distribution of relatively warm and cold water (Figures 3.1,3.2) resulted in conditions where prevailing trade winds blew across the large-scale northwest-southeast aligned SST gradients and fronts.

In the following sections, SWIFT and Wave Glider observations are compared to SST from a composite satellite product, the Group for High Resolution Sea Surface Temperature (GHRSST) Level 4 Operational Sea Surface Temperature and Sea Ice Analysis (OSTIA) Global Foundation Sea Surface Temperature Analysis (UK Met Office, 2005), in order to make qualitative and quantitative comparisons with the in situ data. This product is consistent with observations near the study site with a small (on the order of 0.1°C) varying regional bias (Wick et al., 2022).

3.2.2 SWIFT observations

Surface Wave Instrument Float with Tracking (SWIFT) drifters are nearly Lagrangian surface-following platforms (Thomson, 2012) with a minimal amount of windage (Iyer et al., 2022). Two version 3 (v3) SWIFT drifters (Thomson, 2012) and four version 4 (v4) SWIFT

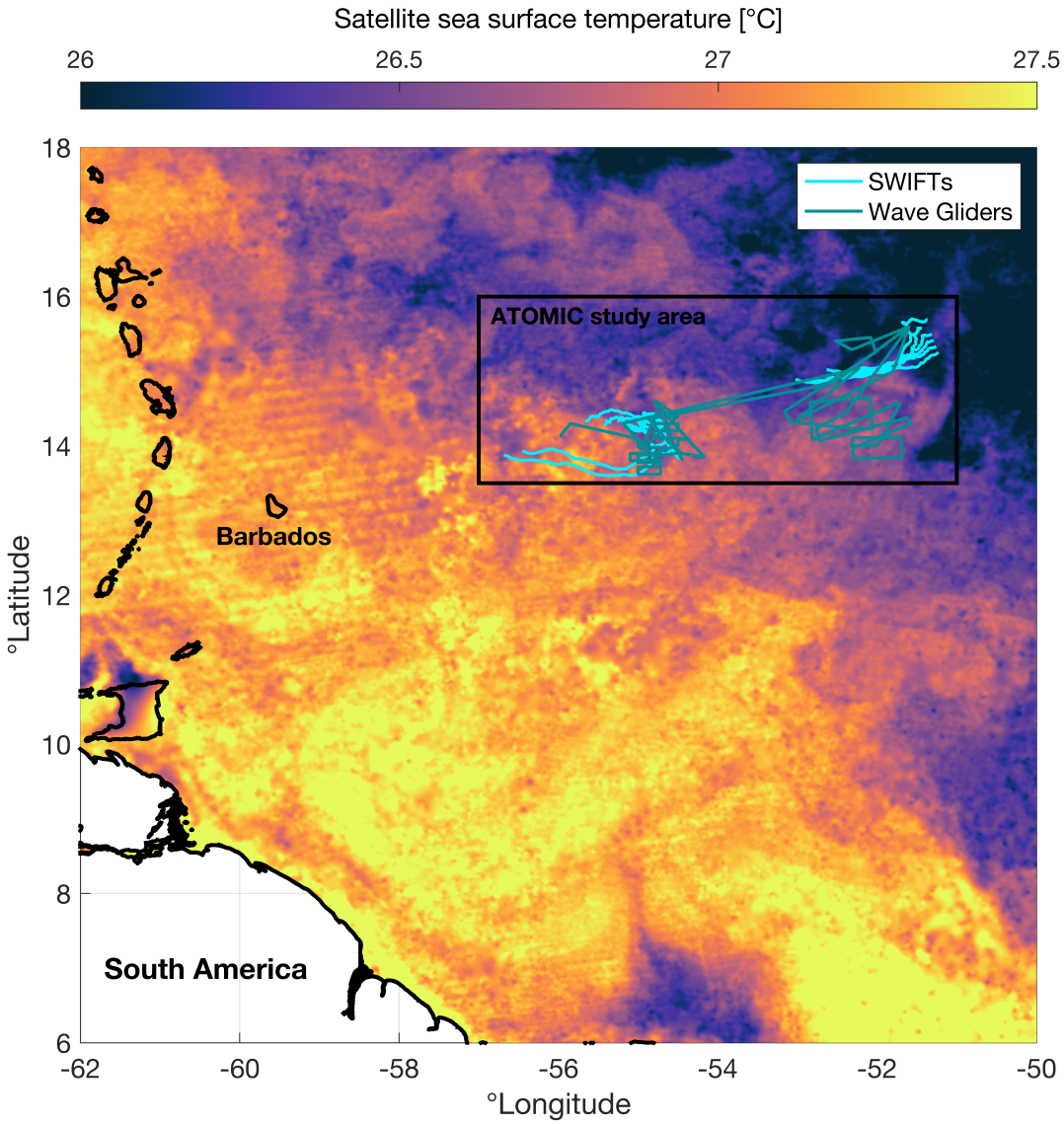

Figure 3.1: GHRSST-OSTIA satellite SST at 09:00 UTC on Feb 3 2020 near the ATOMIC study area. Cyan and green lines denote SWIFT and Wave Glider tracks during ATOMIC (14 Jan to 11 Feb 2020).

drifters (Thomson et al., 2019) were deployed as part of the ATOMIC field campaign from the NOAA Ship *Ronald H. Brown* from 14 Jan 2020 to 22 Jan 2020 and 30 Jan 2020 to 11 Feb 2020 (Figure 3.1). The present study will only analyze observations from v4 drifters, which were equipped with Vaisala 350WX meteorological sensors at 0.5 m height and Aanderaa 4319 conductivity-temperature sensors at 0.3 m depth and thus made the atmosphere and ocean observations necessary to calculate bulk air-sea heat, moisture, and buoyancy fluxes. As minimal near-surface stratification was present, the difference between true SST and 0.3 m ocean temperature is roughly equal to the cool skin correction (Paulson and Simpson, 1981). Though not constant throughout the campaign, the mean correction was 0.2°C at the *Ronald H. Brown*. In this manuscript, ocean temperature measured at 0.3 m depth is taken as SST, but the mean skin correction of 0.2°C is applied when calculating bulk air-sea fluxes. Downwelling radiation data were not measured to estimate the skin SST locally using a bulk cool-skin algorithm (Fairall et al., 1996). V4 SWIFTs were also equipped with a GPS, Nortek Signature 1000 ADCPs to measure near-surface currents, and an SBG Ellipse attitude and heading reference system to measure wave parameters and spectra. Instrumentation, deployment strategy, and additional background on SWIFT drifters is described in detail by Iyer et al. (2022). All SWIFT data shown in the present study are 10-min averages from the top of each hour sent via Iridium telemetry.

3.2.3 Wave Glider observations

Two Liquid Robotics Wave Gliders (Hine et al., 2009) were deployed during ATOMIC on 9 January 2020. One of the Wave Gliders was recovered on 7 February 2020 (30 days deployed) while the other was recovered on 11 February 2020 (34 days). Wave Gliders were equipped with GPS and sensors at several heights and depths used to measure atmospheric and oceanic parameters (Quinn et al., 2021). The present study will utilize atmospheric observations at 1.3 m height from Airmar WX200 meteorological sensors, which measured wind speed as well as air temperature and pressure, in addition to observations from Aanderaa 4319 sensors, which measured ocean temperature and conductivity at 0.24 m depth. The 0.24 m ocean

temperature measurements from the Wave Gliders will hereinafter be referred to as SST. As with the SWIFT measurements, downwelling radiation data were not measured so local skin SST estimates could not be made. Wave Gliders were also equipped with Vaisala WXT530 meteorological sensors at 1.0 m height, which measured the above atmospheric parameters in addition to relative humidity, but these malfunctioned soon after deployment and their data are not shown. Analysis of air-sea fluxes from Wave Gliders will focus only on the bulk sensible heat flux. Wave Glider data shown in the present study have a temporal resolution of 30 minutes, with each data point representing a 20-minute average sent via Iridium telemetry.

Wave Gliders are autonomous vehicles that can be remotely piloted to move at up to 2 $km\ hr^{-1}$. Wave Glider tracks were strategically programmed based on recent observations from SWIFTs, Wave Gliders, the NOAA Ship *Ronald H. Brown*, and satellites. These tracks, shown by straight lines in Figure 3.2a, were preferentially selected to sample significant SST gradients and systematically sample conditions that are difficult to observe with Lagrangian platforms, for instance in directions counter to the wind and/or currents. A specific benefit of using Wave Glider observations to analyze spatial variability is that Wave Gliders have the capability to cross a persistent ocean front multiple times. When a front was identified from observations, Wave Gliders were piloted to repeatedly cross it (e.g., Figure 3.3) and obtained high-resolution measurements of smaller-scale SST fronts. A potential complication to this strategy is that both spatial and temporal variability influence the observations; this is discussed further in section 3.4.

3.3 Methods

3.3.1 Data calibration and corrections

SWIFT and Wave Glider measurements were calibrated using observations from the NOAA Ship *Ronald H. Brown* and the same method as described by Iyer et al. (2022). By assuming that ship and drifter observations should be identical within 5 km distance of each other (or 15 km if insufficient data were available from within 5 km), linear regressions were used

to correct wind speed, relative humidity and air temperature observations (Thomson et al., 2021). To remove the influence of diurnal artifacts, nighttime data were used for air and ocean temperature offset corrections and, for air temperature, only data collected from 22:00 to 10:00 UTC (approximately 18:00 to 06:00 local time) were used in further analysis. Root mean square errors in offsets were lower than sensor precision specifications: SWIFT wind speed, relative humidity and air temperature root mean square uncertainties were 0.24 to 0.96 ms^{-1}, 0.8 to 2.1% and 0.03 to 0.58°C, respectively. Wave Glider wind speed and air temperature uncertainties were 0.75 to 0.87 ms^{-1} and 0.11 to 0.27°C, respectively. SWIFT and Wave Glider ocean temperatures were corrected by subtracting the average of each platform's value from ocean temperatures observed from the ship's sea snake (approximately 0.05 m depth) when a platform was within 2 or 5 km of the ship. These ocean temperature offsets were typically much smaller than those used to correct the air temperature measurements (< 0.1°C).

3.3.2 Bulk flux calculations

Version 3.6 of the COARE bulk flux algorithm (Edson et al., 2013; Fairall et al., 1996, 2003) was used to calculate air-sea fluxes from SWIFT and Wave Glider observations. COARE version 3.6 is similar to COARE version 3.5 (Edson et al., 2013) but utilizes a wave model (Banner and Morison, 2010) to parameterize the effect of wave age on surface roughness and stress. Fluxes were only calculated when all relevant atmospheric or oceanic observations were available, with two exceptions: First, when air pressure and wind speed observations were not available from SWIFTs, measurements from nearby drifters were substituted because those parameters were generally spatially invariant. Second, even though local humidity observations were not made from Wave Gliders, sensible heat fluxes still are reported from these platforms as sensible heat flux is insensitive to humidity. We reiterate that calculations presented here are of bulk fluxes calculated from 10-min mean fields, not direct eddy covariance flux measurements.

3.3.3 Analysis strategy and sensitivity experiments

Several analysis techniques were used to evaluate the spatial variability of air-sea fluxes and its causes. In situ SST observations were used to identify periods of time during ATOMIC when significant SST variability existed across Wave Glider tracks or between different SWIFT drifters. For case studies, a threshold SST was visually identified to separate areas of relatively warm and cold water. SST frontal locations were verified visually with satellite SST maps. In the Wave Glider cases, the orientation of fronts was defined by selecting points in space with observed temperatures within 0.02°C of this threshold and performing a linear regression of latitude versus longitude. Several different methods, including using piecewise functions and SST gradients to define the frontal position, were also tested and produced negligibly different results. Thus, using this method only leads to negligible artificial smoothing even though fronts are likely not completely linear and exhibited temporal variability. This procedure was not used in SWIFT cases because drifters did not typically cross fronts and thus a clear frontal boundary could not be identified. To distinguish cases where the spatial ocean structure was observed directly (Wave Gliders) from cases where gradients were inferred as the difference between two point measurements separated in space (SWIFTs), we hereinafter only use the term "front" to refer to SST fronts observed by Wave Gliders. Fluxes were then compared on both sides of the defined front (Wave Gliders) or between areas with temperatures above and below the threshold (SWIFTs). A combined analysis of all of the periods of time when significant SST gradients existed was then used to evaluate flux variations across these gradients.

A goal of the present study is to evaluate the influence of individual components on air-sea fluxes with a specific emphasis on SST, the primary parameter through which ocean fronts affect air-sea interaction. Two COARE sensitivity tests were conducted for each case study to isolate the effect of ocean (SST) variability from the influence of atmospheric (air humidity, temperature, wind) variations on fluxes. Thus, COARE was run a total of three times to calculate fluxes for each case:

- Observed
- "Ocean-variability-only" (OV) sensitivity tests
- "Atmosphere-variability-only" (AV) sensitivity tests

"Observed" simply refers to air-sea bulk fluxes calculated using the observed ocean and atmospheric parameters from SWIFTs or Wave Gliders as inputs (see section 3.2). The first set of sensitivity tests, OV, involved calculating bulk fluxes using the observed SST but constant regionally-averaged (average value from all SWIFT or Wave Glider observations during a given period of time) atmospheric parameters as inputs into COARE. That is, atmospheric parameters including air temperature, humidity, and wind speed were kept constant. These tests represent the fluxes that would be present if SST gradients exist but the atmosphere was invariant in this region and time period. Similarly, AV fluxes were estimated by calculating fluxes with COARE using observed atmospheric parameters and regionally-averaged ocean parameters. The same method was used in a composite analysis accounting for all of the SWIFT observations during ATOMIC. Using spatially-averaged parameters to isolate the influence of individual or sets of variables on fluxes is analogous to the temporally-smoothed parameters used in sensitivity tests by previous studies to isolate the influence of high-frequency vs. low-frequency SST (Shinoda et al., 1998; DeMott et al., 2016; Gao et al., 2019) or atmospheric variables (Dellaripa and Maloney, 2015) on surface fluxes.

3.3.4 Isolating diurnal and temporal variability from spatial variability

Several techniques were used to isolate the effects of spatial variability from temporal variability in Wave Glider observations. Wave Gliders were programmed to move at near their maximum speed so that measurements can be interpreted as snapshots in time as much as possible. To minimize the influence of temporal nighttime air temperature variability, the two Wave Gliders were strategically directed to obtain simultaneous measurements of both

sides of a gradient. One such technique used frequently during the second leg of ATOMIC such as in case study 1 (Figure 3.3) involved directing the Wave Gliders to follow the same path with a set time lag. For SWIFT drifters, Lagrangian motion ensured that platforms usually stayed in the same general water mass and did not cross fronts. Because of this, observations from multiple drifters located across gradients at the same time were used to assess spatial variability.

3.4 Results

3.4.1 Background conditions during ATOMIC

Figure 3.2 shows histograms of observations from SWIFTs and Wave Gliders during the entirety of the ATOMIC campaign. Averaged over the ATOMIC dataset, the air-sea (sea minus air) temperature and specific humidity differences were 0.86°C and 5.4 $g\ kg^{-1}$, which imply positive upward heat, moisture, and buoyancy fluxes. COARE 3.6 calculations showed that bulk air-sea sensible heat, latent heat, and upward buoyancy fluxes were on average 6.6 Wm^{-2}, 157 Wm^{-2}, and 16.5 Wm^{-2}, respectively. In this paper, positive flux values denote upward fluxes from the ocean to the atmosphere.

3.4.2 Case studies

Case 1: Wave Gliders drive across a persistent front

From 2-6 February 2020, two Wave Gliders repeatedly crossed over a persistent SST front with approximately a 12 hour time lag (Figure 3.3). We define the front's position in space (Figure 3.3e) using linear regression of observations where the SST was near a 26.8°C threshold. The observed SST front is consistent with the SST gradient observed in GHRSST-OSTIA satellite observations (Figure 3.3g inset), although the satellite observations are biased cold by 0.2°C, slightly larger but in the same direction as the average 0.08° cool skin-corrected bias reported by Wick et al. (2022) in the ATOMIC region. Wind speeds and nighttime air temperatures did not show consistent spatial trends and instead exhibited

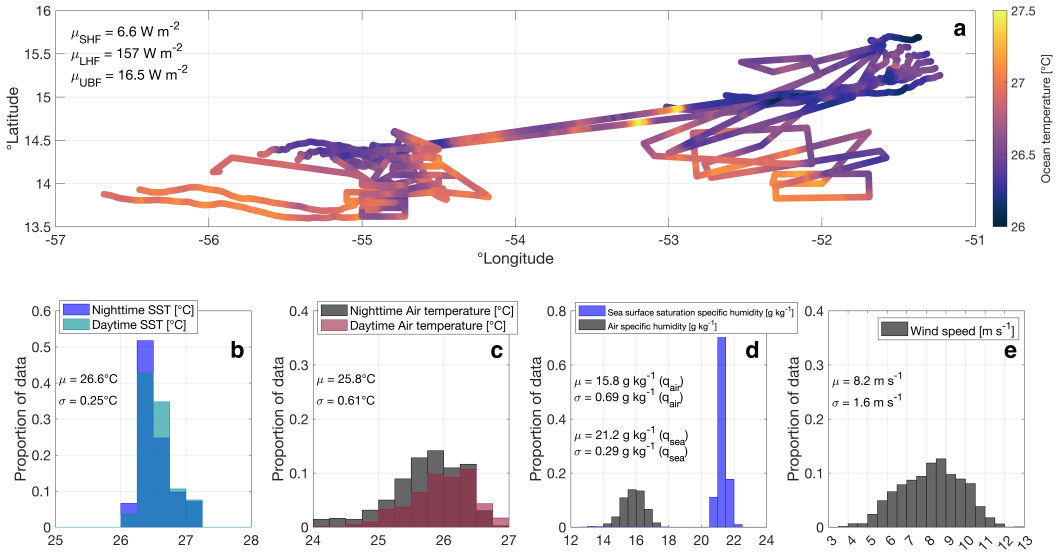

Figure 3.2: SWIFT observations from 14 Jan 2020 to 11 Feb 2020 during ATOMIC (a) Map of SST (observed at 0.3 m depth) (b) Histograms of nighttime and daytime SST (c) Histograms of nighttime and daytime 0.5 m air temperatures (d) 0.5 m air specific humidity and ocean surface saturation specific humidity (e) Wind speed corrected to 10 m height.

high-frequency variability. Wind directions were consistently from the northeast on both the warm (average direction from of 75°) and the cold (68°) sides of the front; thus wind blew across the front from warm to cold water. That is, in contrast to the observations of Shao et al. (2019) and numerical model results (e.g., Sullivan et al., 2020), no clear spatial wind speed or directional response to SST gradients was observed. This may be a result of the small spatial scale or weak magnitude of the observed SST front.

The spatial variability of sensible heat flux estimated from COARE 3.6 (Figure 3.4a) mirrors that of air-sea temperature differences shown in Figure 3.3c, with higher values in warm water east of the front and small-scale variability resulting from variations in air temperature. The average sensible heat flux on the west (cold) side of the front was 4.1 Wm^{-2}, approximately 50% lower than the average sensible heat flux on the warm side (Figure 3.4a). This is a significant difference considering that sensible heat fluxes were only 6.6 Wm^{-2} throughout ATOMIC (Figure 3.2). Correlation between SST and sensible heat flux on spatial scales under 10 km was also observed by Shao et al. (2019) across larger SST gradients. Because the buoyancy flux $B = SHF + (0.61 \times LHF \times c_p \times T_{air}/L_v)$, where c_p is the specific heat of air and L_v is the latent heat of vaporization (Johnson et al., 2001), sensible and latent heat fluxes contribute almost equally to the buoyancy flux in these tropical oceanic conditions and thus it is likely that the buoyancy flux significantly varies across the front as well; however, we cannot quantify this without collocated humidity measurements.

Results from the OV and AV sensitivity tests are shown in Figure 3.4c and 3.4b. The average slope of the OV flux (Figure 3.4c) resembles the average slope in the observed fluxes (Figure 3.4a) within 10 km of the frontal boundary, which suggests that the SST drove the linear increase in fluxes across the front. However, the observed and AV fluxes exhibit high-frequency fluctuations at all locations in space, which implies that the atmosphere has a significant role in modulating variations in air-sea fluxes, both close to and farther away ($>$ 10 km) from the frontal boundary. The sharp sensible heat flux gradient 5 km west of the frontal boundary appears to be driven by a combination of ocean and air temperature variability.

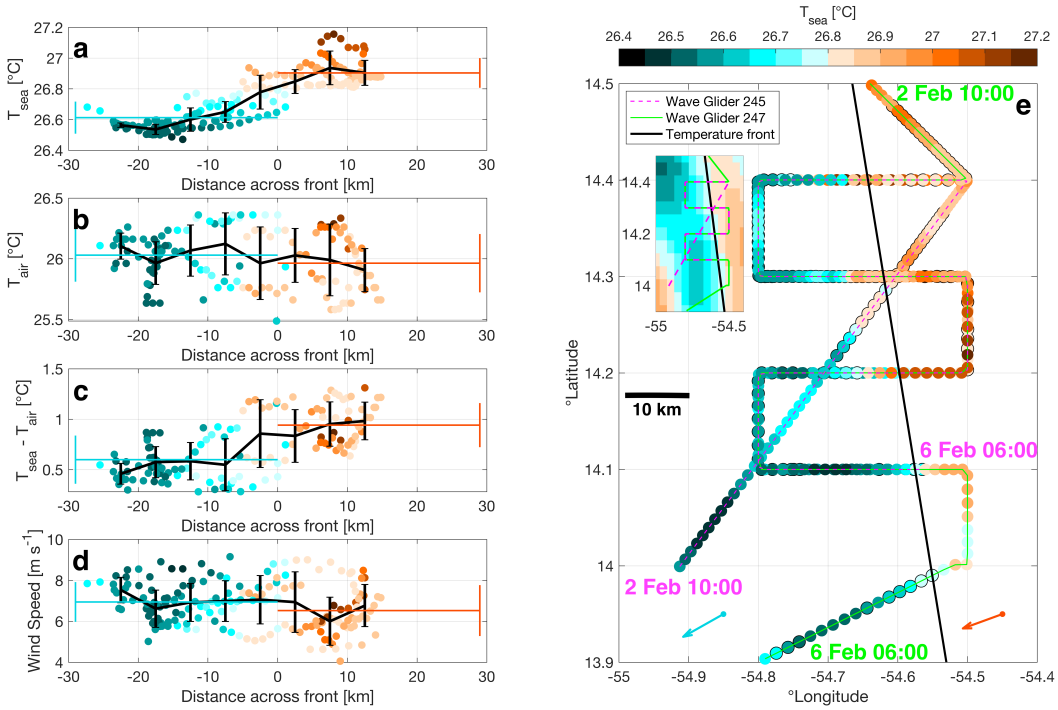

Figure 3.3: Distance from the SST front vs (a) observed SST, (b) air temperature, (c) sea minus air temperature difference, and (d) wind speed from Wave Glider tracks from 2-6 Feb 2020. Colors denote SST and error bars denote averages and standard deviations within 5 km distance increments. Thin horizontal orange and blue lines represent averages and standard deviations on the warm and cold side of the SST front. (e) SST observed by Wave Glider 245 (pink track) and Wave Glider 247 (green track). The green and pink text denote the starting and ending times of the plotted tracks. Only nighttime data are shown. The SST front is shown by the black line. Orange and blue quivers denote the average wind speed and direction on the warm and cold side of the front. Inset: Front location, Wave Glider tracks, and GHRSST-OSTIA satellite SST observations (corrected for -0.2°C offset) from 4 Feb 2020.

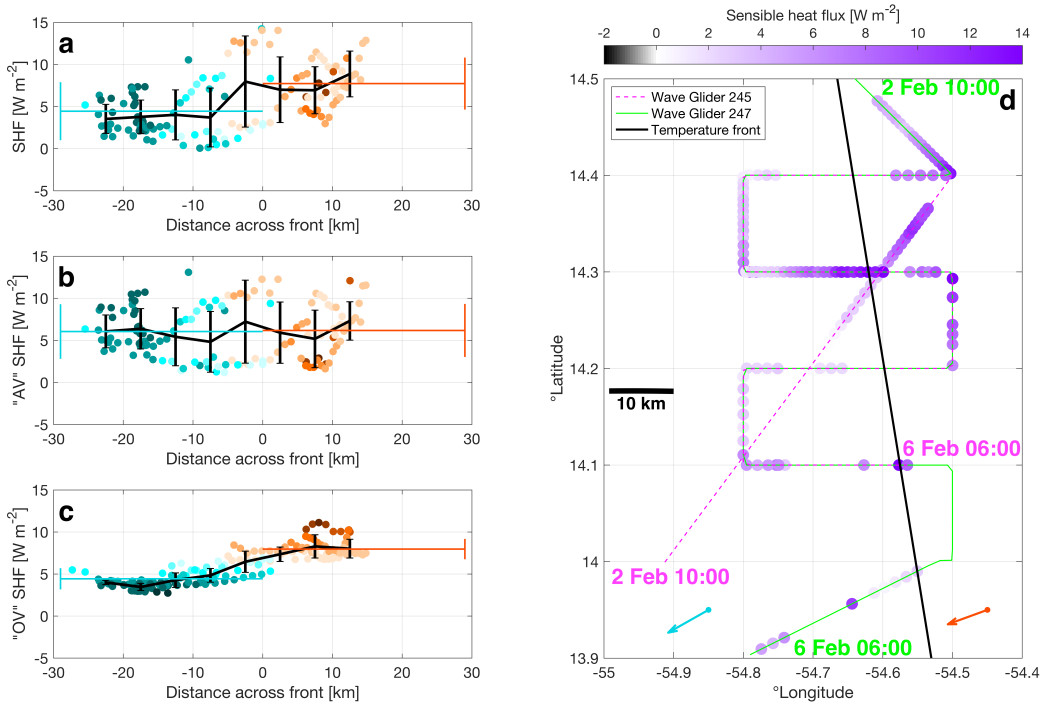

Figure 3.4: Distance from the SST front vs (a) observed sensible heat flux, (b) "atmosphere variability only" (AV) sensible heat flux, and (c) "ocean variability only" (OV) sensible heat flux. As with Figure 3.3a-d, colors denote SST, error bars denote averages and standard deviations within distance bins, and thin horizontal lines represent averages and standard deviations on the warm and cold side of the SST front. (d) Map of Wave Glider tracks with colors denoting nighttime observed sensible heat flux. Lines, text, and quivers denote the same parameters as in Figure 3.3e.

Case 2: Wave Gliders drive across two sharp SST fronts

Two sharp SST fronts were observed from 30 January 2020 to 2 February 2020. SST estimated by satellite was biased cold by 0.4°C, with fronts slightly offset in position, relative to Wave Glider SST. SST varied throughout the domain by 0.7°C (Figure 3.5a) but was mostly constant on both sides of the frontal boundaries. Air temperatures were considerably warmer on average (0.2°C) on the warm ocean sides of both fronts. Thus, SST and air temperature tendencies partially cancel out, so air-sea temperature differences are moderate compared to case study 1 (Figure 3.5c). Wind speeds and directions were very similar on both sides of both fronts and did not show clear evidence of a wind response to the observed SST variability.

Average sensible heat flux was 8.5 Wm^{-2} on the warm side and 7.1 Wm^{-2} on the cold side of the southwestern SST front. These values were 4.0 Wm^{-2} and 1.7 Wm^{-2}, respectively, across the eastern front (Figure 3.6). Fluxes were higher and more variable near the southwestern front because of colder (on average) and more variable air temperatures over this region (Figure 3.5b). In contrast to case 1, OV and AV sensible heat fluxes are elevated on opposite sides of the ocean fronts: OV fluxes are 3.1 Wm^{-2} (southwestern front) and 4.6 Wm^{-2} (eastern front) higher, on average, on the warm sides of the fronts. However, AV fluxes are 2.1 Wm^{-2} (both fronts) lower, on average, on the warm ocean sides of the fronts (Figure 3.6b,c). These values suggest that the influence of SST gradients dominates the spatial variability of the sensible heat flux, but that the atmosphere partially cancels out the influence of SST gradients on the average sensible heat flux across the front. While average sensible heat flux variations were small, strong spatial gradients were observed across both fronts during the night of 1-2 February consisting of abrubt sensible heat flux variations of 4 Wm^{-2} across less than 10 km (Figure 3.5a,b, d inset). OV fluxes also show a strong flux gradient (3-3.5 Wm^{-2}) frontal boundaries, but AV fluxes only show weak gradients ($<= 2$ Wm^{-2}). These findings suggest that, in the vicinity of the frontal boundaries, SST gradients create the region of strongest sensible heat flux gradients, while atmospheric vari-

ability (spatial and/or temporal variations in air temperature from atmospheric boundary layer turbulence, cold pools, or convective structures) influence fluxes farther away from the boundaries. We hypothesize that this may be a result of the atmosphere partially equilibrating to SST gradients. That is, further away from the SST front where water is warm (or cold), the atmosphere may have had ample time or opportunity to warm in response to warmer water (or, cool in response to colder water). However, near (within 10 km of) the front, the atmosphere does not appear to consistently equilibrate to SST gradients on either side, leading to stronger spatial flux gradients shown in Figure 3.6a.

Case 3: SWIFTs drifting across a temperature gradient

Near the start of leg 1 of ATOMIC, the SWIFTs were strategically deployed across an SST gradient and then drifted southwestward from 15 Jan 2020 08:00 UTC to 17 Jan 2020 08:00 UTC. We note that this is the same period of time as case 2 in Iyer et al. (2022). Satellite SST data (see section 5.1) confirm that the orientation of the gradient varied in space: a warm tongue of water (defined as SST >26.4°C) extended eastward from the west and encompassed the central area of the domain (Figure 3.7g). Air temperatures and wind speeds were usually similar (within 0.1°C and 0.5 ms^{-1}) whether water was warm or cold (Figure 3.7b), while average specific humidity was on average 0.5 $g\ kg^{-1}$ greater over cold water (Figure 3.7e). Wind directions in the area were consistently from the northeast.

As with the previous examples, COARE 3.6 simulations and sensitivity tests were used to compute heat fluxes and analyze spatial flux variations. Because humidity data are available from v4 SWIFTs, bulk latent heat and buoyancy fluxes were calculated in addition to sensible heat flux. Latent heat fluxes were on average 25 Wm^{-2} (14%) greater over warm water than cool water (Figure 3.8a,d,g) owing to large differences in air specific humidity (Figure 3.7e,f). However, sensible heat flux differences (0.6 Wm^{-2}; 6%) and upward buoyancy flux differences (2.4 Wm^{-2}; 10%) across the SST gradient were small. AV and OV sensitivity tests (Figure 3.8) suggest that flux variations are driven jointly by the atmosphere and ocean. For sensible heat flux, warmer air temperatures on the warm ocean side partially cancel out the ocean's

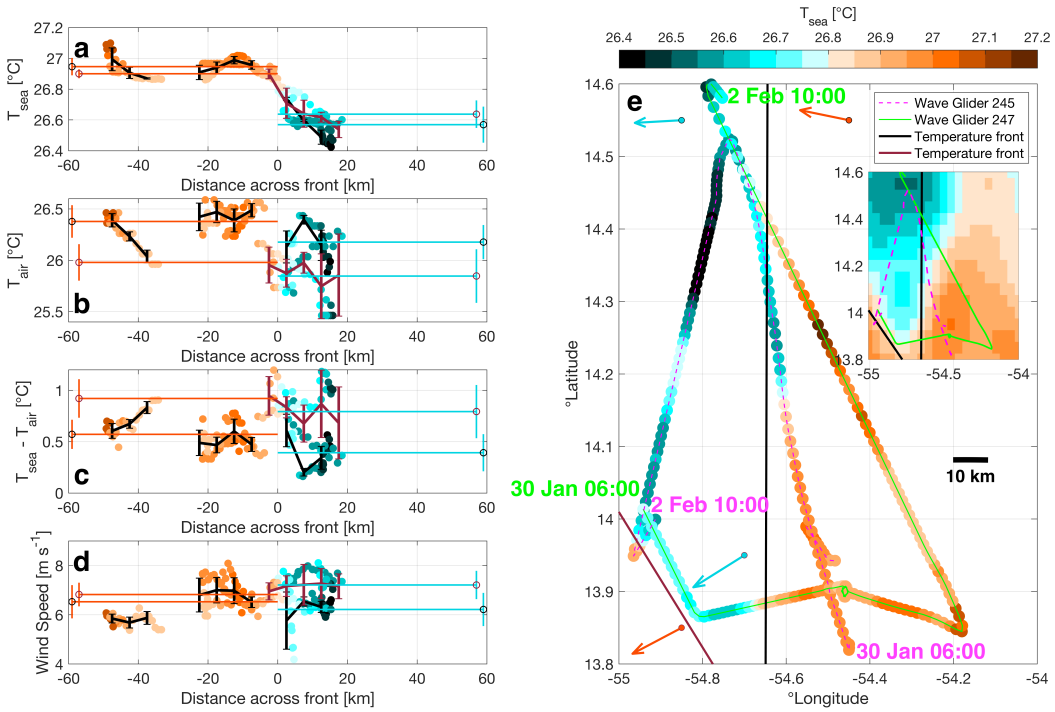

Figure 3.5: Same as Figure 3.3 for case study 2 (30 Jan to 2 Feb 2020). GHRSST-OSTIA satellite SST observations in Figure 3.5a are from 1 Feb 2020 and are offset by +0.4°C to match in situ observations. The red line denotes the position of the second (southwestern) SST front. Orange and blue quivers in the northern and southern part of the domain denote the average wind speed and direction on the warm and cold side of the eastern (black) and southwestern (red) front, respectively. Error bars and open circles in panels (a)-(d) represent binned-averages, mean, and standard deviation of the front of the same color in (e).

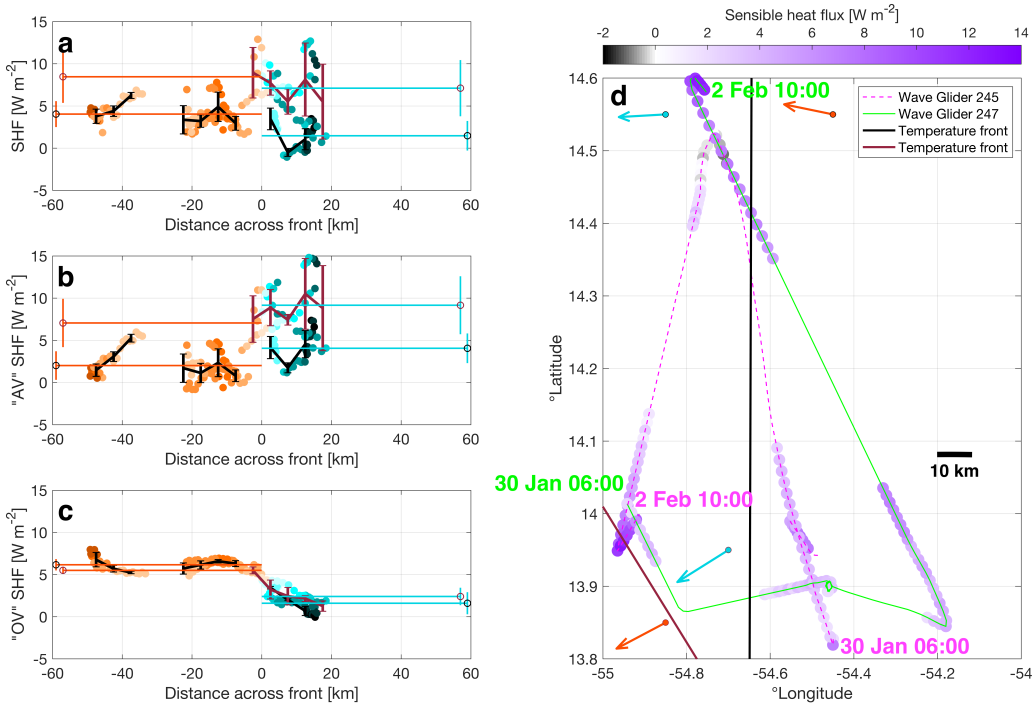

Figure 3.6: Same as Figure 3.4 for case study 2 (30 Jan to 2 Feb 2020). The red line denotes the position of the second (southwestern) SST front. Error bars and open circles in panels (a)-(c) represent binned-averages, mean, and standard deviation of the front of the same color in (d).

influence on air-sea temperature difference. For latent heat flux, higher SST (i.e., higher sea surface specific humidity) and lower air specific humidity on the warm ocean side led to the greater latent heat flux there.

While SST gradients were generally consistent throughout the two-day period of this SWIFT drift, atmospheric temporal variability also modulated gradients in air-sea fluxes. For instance, around midday on 15 January, air temperature and specific humidity increased faster on the cold ocean side than the warm side (Figure 3.7b,e), influencing the air-sea temperature and humidity differences on one side of the gradient and leading to enhanced spatial flux gradients across the SST front. We hypothesize that these variations are due to either turbulent fluctuations or small-scale convective structures. On 16 January, air temperature, wind speed, specific humidity, and air-sea flux variations likely result from an atmospheric cold pool: similar sudden drops in air temperature were observed by the NOAA Ship *Ronald H. Brown* which was on average 60 km away from the drifters (not shown).

3.4.3 Synthesis of all data

Spatial gradients in the ATOMIC region

Figure 3.1 and the presented case studies demonstrate that SST gradients were frequently observed during ATOMIC. This section presents statistical analysis of gradients. Spatial gradients of a field are denoted by Δ and are assessed by calculating differences between two SWIFT drifters at any given point in time. SST differences between any two drifters (ΔT_{sea}) varied between 0.03 - 0.73°C, with an average of 0.20°C and a standard deviation of 0.18°C. $\Delta T_{sea} > 0.3$°C for a total of 254 hours (54% of the total deployment time), and $\Delta T_{sea} > 0.5$°C for 140 hours (29% of the total time). These SST gradients occurred across distances of 10 to 100 km, consistent with submesoscale to mesoscale ocean features. SST gradients persisted for as long as several days (e.g., Figures 3.3,3.5,3.7).

Throughout ATOMIC, considering only drifter-pairs with $\Delta T_{sea} > 0.3$°C, air temperatures were, on average, 0.10°C higher over warmer water. In total, 62% of the SWIFTs

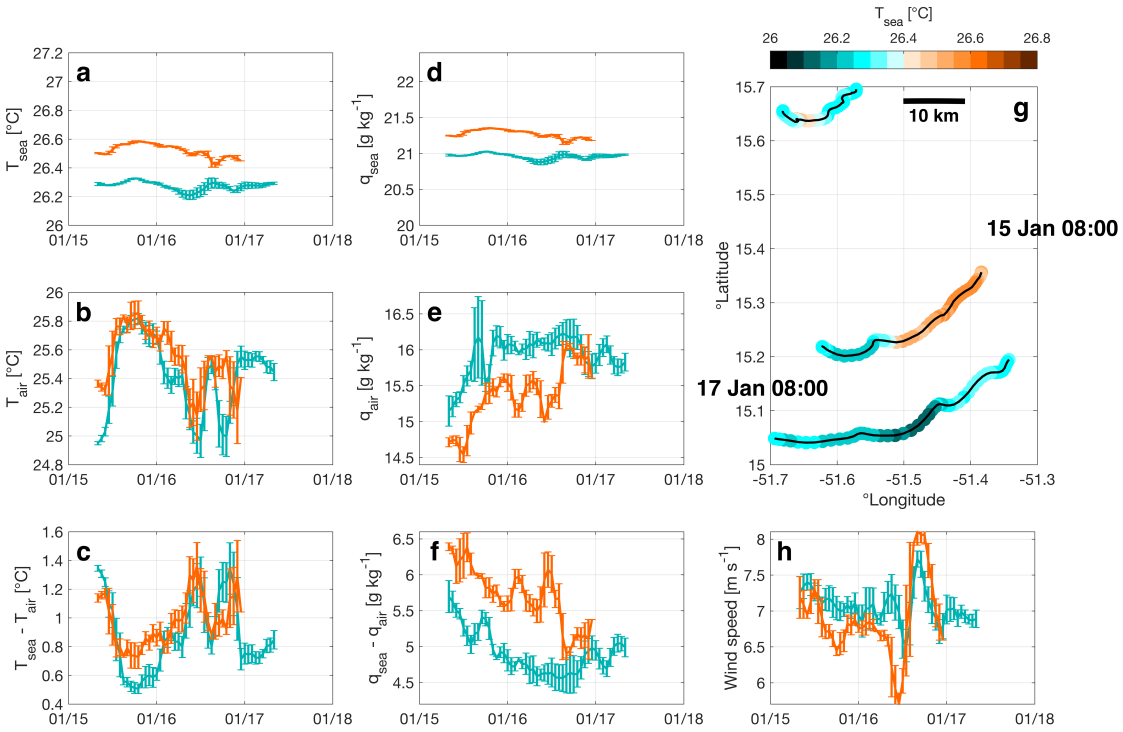

Figure 3.7: Time series of hourly average and standard deviation (error bars) of (a) SST, (b) 0.5 m air temperature, (c) sea minus air temperature, (d) ocean surface saturation specific humidity, (e) 0.5 m air specific humidity, (f) ocean minus air specific humidity, and (h) wind speed corrected to 10 m in areas with warm water (SST $>$ 26.4°C; orange) and cold water (SST $<$ 26.4°C; blue) observed by v4 SWIFTs from 15-17 Jan 2020. (g) Map of SST observed by v4 SWIFTs.

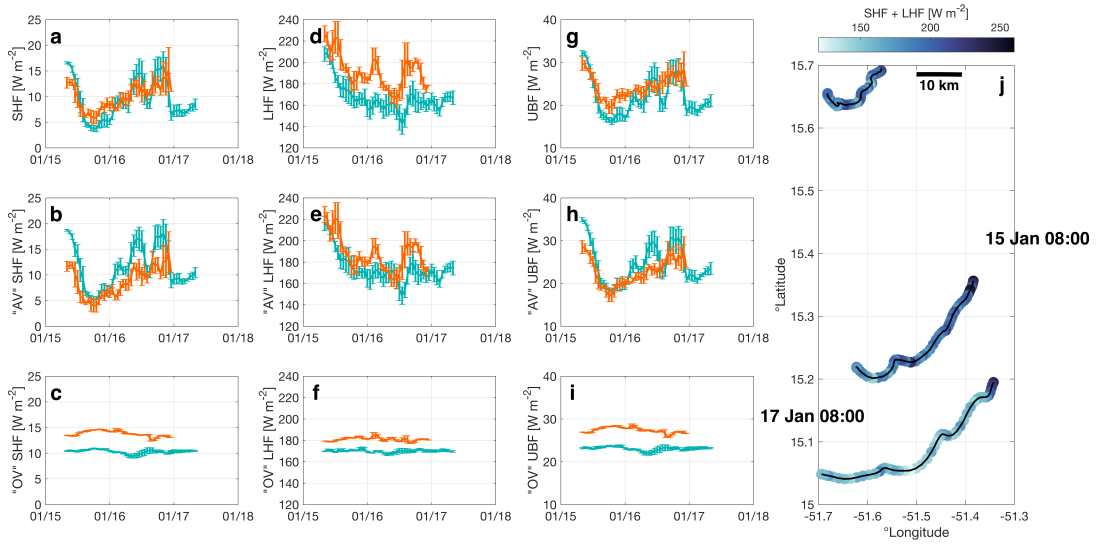

Figure 3.8: Time series of hourly average and standard deviation (error bars) of (a) sensible heat flux, (b) "atmosphere-variability-only" (AV) sensible heat flux, (c) "ocean-variability-only" (OV) sensible heat flux, (d) latent heat flux, (e) AV latent heat flux, (f) OV latent heat flux, (g) upward buoyancy flux, (h) AV upward buoyancy flux, and (i) OV upward buoyancy flux in areas with warm water (SST $>$ 26.4°C; orange) and cold water (SST $<$ 26.4°C; blue) observed by v4 SWIFTs from 15-17 Jan 2020. (j) Map of sensible plus latent heat flux observed by v4 SWIFTs.

on warm sides of strong SST gradients also measured warmer air temperature. Air specific humidity was also usually (65% of the time) higher on the warm side of strong gradients; the average difference was 0.14 $g\ kg^{-1}$. Wind speed differences were 0.4 ms^{-1} lower on average on the warm side of strong gradients, but were highly variable in both space and time and thus not consistently significantly lower on the warm side of gradients.

COARE sensitivity tests

Using the average relationships between observed variables presented above, we now test the sensitivity of COARE 3.6 for the hypothetical flux gradient caused by a given SST gradient alone. Assuming that air temperature and specific humidity variations are present across a strong 0.45°C ocean gradient (the average of observed ΔT_{sea} when $\Delta T_{sea} > 0.3$°C) and are equal to the average values stated in the previous section,, the sensible heat flux, latent heat flux, and upward buoyancy flux will vary across the gradient by 5.9 Wm^{-2} (65%), 17.7 Wm^{-2} (8%), and 7.2 Wm^{-2} (29%), respectively. These variations indicate that significant spatial flux gradients relative to mean values, especially for sensible heat flux, will typically occur across 10-100 km SST gradients in the tropical Atlantic trade wind region.

To assess the magnitude of typical flux gradients in the ATOMIC region (as opposed to the strong SST gradients described in the previous paragraph), we perform the same sensitivity tests using a 0.17°C SST gradient, the average difference observed between pairs of SWIFTs during ATOMIC. Incorporating average atmospheric gradients, the resulting sensible heat flux, latent heat flux, and upward buoyancy flux will increase on the warm side of the SST gradient by 2.6 Wm^{-2} (28%), 9.3 Wm^{-2} (4%), and 3.3 Wm^{-2} (13%), respectively. These flux gradients are weaker than the gradients expected when $\Delta T_{sea} > 0.3$°C, but still demonstrate that non-negligible variability would be expected in the ATOMIC region, even in the absence of a strong SST gradient. As seen in the case studies, significant variations in surface fluxes are driven by SST variations, even as atmospheric gradients tend to homogenize or eliminate those flux gradients.

Flux variations across persistent SST gradients

While the sensitivity analysis provides insight into the how fluxes varied across SST gradients on average, it does not address the fact that SST gradients were associated with differing spatial atmospheric patterns or that SST gradients were observed across a wide range of distances. To address these points, we identify three persistent SST gradients (Figure 3.9) observed during ATOMIC and perform a targeted analysis of the influence of individual parameters on air-sea fluxes from v4 SWIFT drifters on either side of gradients. The SST gradients shown here, which include the three case studies in section 4.2, collectively span 17 total days of observations and thus cover over 80% of the time during which SWIFTs were deployed. The spatial consistency between observations and daily satellite data suggests that these SST gradients are large-scale persistent features which are not associated with temporal variability. Further supporting this evidence of submesoscale to mesoscale ocean variability is the observation that drift tracks observed across SST gradients 2 and 3 indicate that surface currents on either side of the SST gradient were different, with more variable currents on the cold ocean side (Figure 3.9b,c). The differences (warm ocean side minus cold ocean side) in distance (spacing between drifters), fluxes of sensible heat, latent heat, and upward buoyancy (SHF, LHF, UBF), and their components of air specific humidity and temperature and air-sea differences of those quantities (q_{air}, T_{air}, $T_{sea} - T_{air}$, $q_{sea} - q_{air}$) are shown in Figure 3.10 and Figure 3.11. Figure 3.10 also shows the expected influence of these variations on sensible and latent heat flux as background contours. Figure 3.11 shows the correlation between sensible heat, latent heat, and upward buoyancy flux gradients as well as gradients of their components, with colors representing the distance between drifters.

First, it is important to note that the three large-scale SST gradients occupy different regions of the flux parameter space shown in Figure 3.10 and 3.11 and thus gradients are not generalizable in a composite sense: Gradient 3 (3 to 10 February; diamonds on Figures 3.10,3.11) was associated with high ΔT_{sea} and Δq_{air} (Figure 3.10a,d) and low ΔT_{air} (Figure 3.10a), while gradient 1 (14 to 18 January; circles on Figure 3.10,3.11) was associated with

moderate ΔT_{sea}, negative Δq_{air}, and high ΔT_{air} (Figure 3.10a) across the SST front (Figure 3.10d). Gradient 2 (31 January to 3 February; squares on Figure 3.10,3.11) exhibited a mix of characteristics from gradients 1 and 3.

Although atmospheric and oceanic parameters vary on a case-by-case basis, Figure 3.10 still provides quantitative insight into the impact that SST and atmospheric gradients are expected to have on gradients of air-sea fluxes in the Atlantic trade wind region during the boreal winter. SST gradients would be expected to drive sensible heat flux gradients of up to 5-10 Wm^{-2} (horizontal spread across contours in Figure 3.10a,b) and latent heat flux gradients (as sea surface specific humidity and SST are directly proportional) of up to 20 Wm^{-2} (horizontal spread across contours in Figure 3.10d,e). The combined contribution of SST, air temperature, wind speed, air humidity (including the air-sea differences) would be expected to result in sensible and latent heat flux gradients of over 10 and 50 Wm^{-2} (spread across contours in Figure 3.10c,f), respectively; that is, greater variability (spread across contours in Figure 3.10c,f) than from SST gradients alone.

Aggregating data from the three fronts, the spatial gradients of sensible heat, latent heat, and upward buoyancy fluxes were as high as 10, 50, and 10 Wm^{-2}, respectively (Figure 3.11). Average fluxes were 2.5, 15.6, and 3.7 Wm^{-2} higher on the warm ocean side of gradients, respectively. The strong correlation between ΔT_{sea} and ΔT_{air} and ΔSHF (Figure 3.11a,b) and even stronger correlation between $\Delta(T_{sea} - T_{air})$ and ΔSHF (Figure 3.11d) suggests that gradients in SST and air temperature modulate gradients in sensible heat flux, with a negligible contribution from wind speed (Figure 3.11c). Quantitatively, comparing the typical highest and lowest ΔSHF values across the range of observed SST and T_{air} (i.e., binned averages in Figure 3.11a,b), the SST and T_{air} contributions are individually up to approximately 5 Wm^{-2}.

ΔLHF, on the other hand, is highly variable across SST fronts, uncorrelated with Δq_{sea} (and therefore ΔT_{sea}; Figure 3.11e), strongly correlated with Δq_{air} (Figure 3.11f), and moderately correlated with ΔU_{10} (Figure 3.11g). This suggests that latent heat flux is strongly influenced by atmospheric gradients rather than SST gradients and is further supported by

the fact that the correlation between $\Delta(q_{sea} - q_{air})$ and ΔLHF (Figure 3.11h) is not any stronger than the correlation between Δq_{air} and ΔLHF (Figure 3.11f). Comparing the highest and lowest binned average ΔLHF values, q_{air} and U_{10} variations contribute up to 40 and 10 Wm^{-2}, respectively, to the latent heat flux. This contrasts from the expected flux contribution from SST in Figure 3.10 and the spread in OV sensitivity test fluxes in Figure 3.8: in short, while the previous analysis shows that SST has a small influence on latent heat flux gradients and is likely responsible for the positive average ΔLHF during ATOMIC, atmospheric humidity variations are much larger than SST variations and thus the atmosphere is the dominant driver of latent heat flux variations in the region at this time of year. These atmospheric gradients may result from several different processes including atmospheric turbulence, cold pools (Zuidema et al., 2012; de Szoeke et al., 2017), or small-scale tropical convective activity (Yokoi et al., 2014). While some of these features can persist over timescales of hours, we note that the observed atmospheric-driven spatial flux gradients generally only last for a very short time, because atmospheric motion (i.e., wind) quickly moves coherent structures in the lower atmosphere across SST gradients and out of the domain. Upward buoyancy fluxes are influenced by both sensible and latent heat fluxes. Thus, buoyancy flux gradients are driven by SST gradients to a lesser degree than sensible heat flux gradients but to a greater degree than that of latent heat flux gradients, as shown by the weaker positive correlation in Figure 3.11i. Despite the strong influence of specific humidity gradients on latent heat flux gradients, the influence of specific humidity gradients on buoyancy flux gradients is near zero (Figure 3.11k,l), likely masked by the strong influence of gradients in SST and air temperatures on ΔSHF (Figure 3.11m). Wind speed gradients have little effect on ΔUBF ($R = 0.07$, not shown).

Spatial scales of SST gradients

Overall, as would be intuitively expected, large ΔT_{sea}, ΔSHF, and ΔUBF primarily occur when drifters are spaced farther apart (i.e., blue points on Figure 3.11 are associated with larger values). While this may suggest that stronger SST and flux gradients typically occur

across larger distances, the presented spatial scales of variability are not comprehensively defined because SWIFTs observe individual points in space and do not resolve spatial variability between those points. For instance, SST variations observed tens of kilometers apart may be associated with a sharp smaller-scale front, such as the front observed with Wave Glider case study 2 (Figures 3.5,3.6). Regardless, it is clear that large differences are not observed when drifters are close together: SST gradients > 0.5°C were rarely observed when drifters were closer than 50 km apart.

On the other hand, ΔLHF (Figure 3.11e-h) was uncorrelated with the spacing between drifters. This first implies that air humidity gradients, the dominant driver of latent heat flux variability, often completely reversed the influence of higher q_{sea} (warmer SST) on increasing fluxes. Furthermore, this suggests that atmospheric gradients varied greatly across all spatial scales of SST gradients. That is, variations in air temperature, specific humidity, and wind speed, likely due to turbulent fluctuations in the atmosphere or small-scale atmospheric systems, were not consistently larger or smaller at specific spatial scales throughout the area on any scales under 100 km.

3.5 Discussion and Conclusions

Significant submesoscale spatial SST variability was present during ATOMIC despite this being a rather quiescent area of the open ocean away from strong mesoscale eddy activity in the boreal winter. This variability may be an eventual result of the cascade of North Brazil Current eddy kinetic energy to smaller scales. The presented case studies illustrate that gradual SST gradients with changes of up to 0.7°C over tens of kilometers (e.g., Figure 3.3) were observed in addition to sharp fronts with SST changes of up to 0.4°C over scales less than 10 km. In all cases, sensible heat and buoyancy fluxes were consistently elevated on warm sides of SST fronts. Figure 3.11 quantifies spatial variability in heat, moisture, and buoyancy fluxes across scales of 10 to 100 km. Sensible heat fluxes and upward buoyancy fluxes varied by up to 10 Wm^{-2} between drifters spaced 10-100 km apart, while latent heat flux differences between drifters were as high as 50 Wm^{-2}. The average flux differences

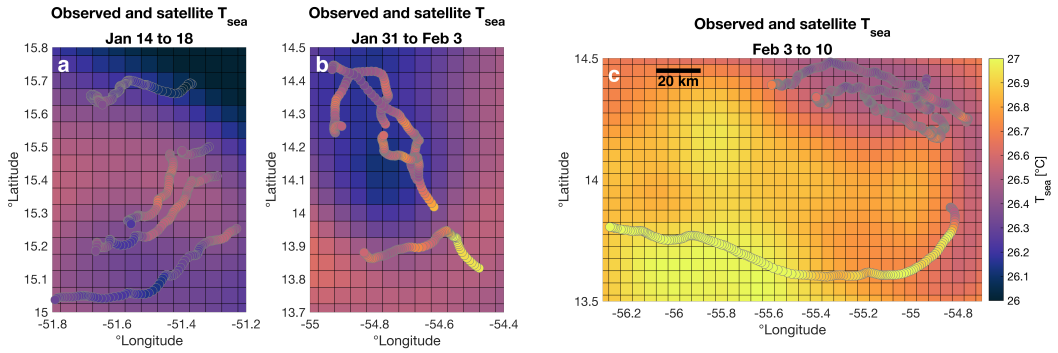

Figure 3.9: Observed SST plotted on a background of GHRSST-OSTIA satellite SST taken midway through each a time period during which a persistent SST gradient was observed on (a) 14-18 Jan 2020, (b) 31 Jan - 2 Feb 2020, and (c) 3-10 Feb 2020.

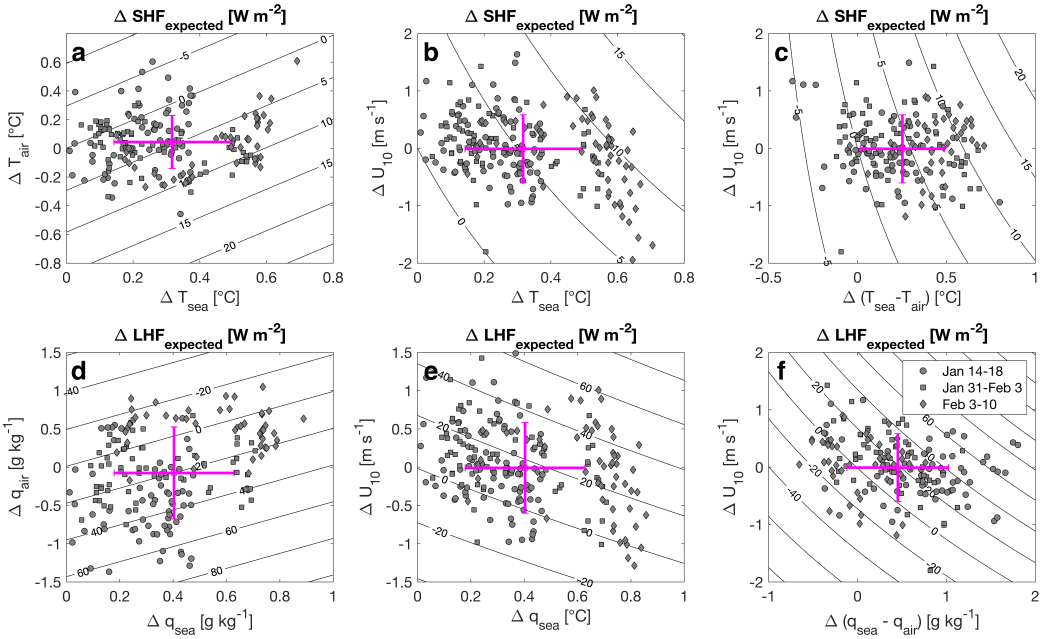

Figure 3.10: Change in ocean parameters, atmospheric parameters, and air-sea differences across three persistent gradients during ATOMIC. Contour lines show expected change in (a,b,c) sensible heat flux or (d,e,f) latent heat flux based on values on the x- and y-axes assuming average conditions observed during ATOMIC. Marker shapes indicate gradient number (circle: gradient 2, Jan 14-18; square: gradient 3, Jan 31-Feb 1; diamond: gradient 3 Feb 3-10). Pink error bars denote mean and standard deviations of changes across all of the three time periods.

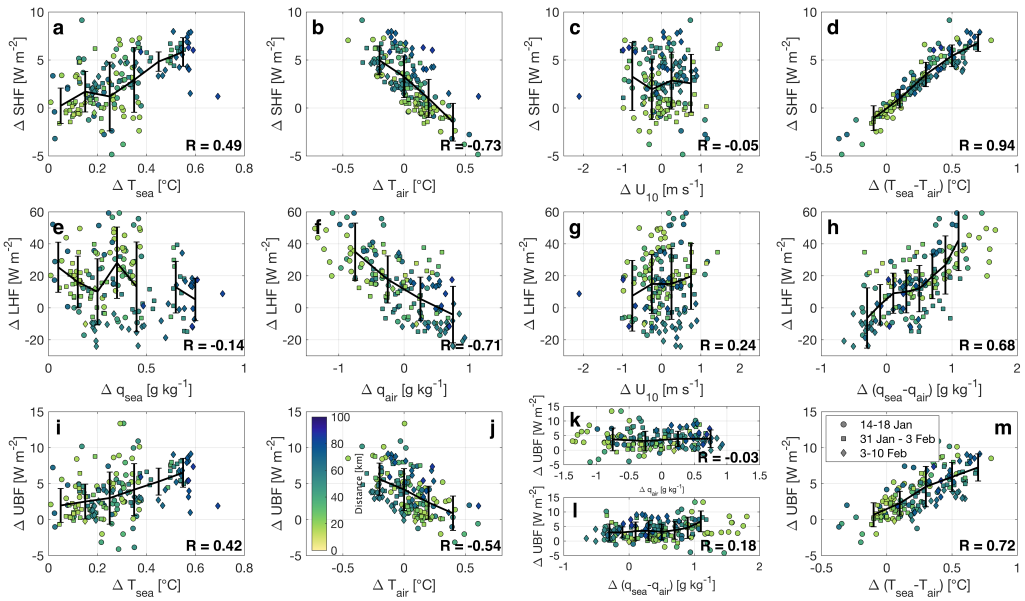

Figure 3.11: Change in (a,i) SST, (e) sea surface saturation specific humidity, (b,h) air temperature, (f,k) air specific humidity, (c,g) wind speed, (d,m) air-sea temperature difference, or (h,l) air-sea humidity difference vs. change in air-sea (a,b,c,d) sensible heat, (e,f,g,h) latent heat, and (i,j,k,l,m) upward buoyancy flux across three persistent gradients during ATOMIC. Marker colors denote distance between plotted observations and marker shapes indicate gradient number (circle: gradient 2, Jan 14-18; square: gradient 3, Jan 31-Feb 1; diamond: gradient 3 Feb 3-10). Black error bars denote average and standard deviations of observations within data binned by the property denoted on the x-axis. "R" values shown on the bottom right of represent linear correlation coefficients of property (x-axis) vs. flux (y-axis) for each panel.

across these spatial scales (mean distance of 44 km) were 2.5 Wm^{-2} (sensible heat), 15.6 Wm^{-2} (latent heat), and 3.7 Wm^{-2} (upward buoyancy). Average sensible heat, latent heat, and upward buoyancy fluxes observed in the ATOMIC region were approximately 5 Wm^{-2}, 157 Wm^{-2}, and 16 Wm^{-2}, respectively. So, the observed differences across 10-100 km correspond to a maximum variation of roughly 200%, 30%, and 60%, respectively, of observed fluxes during ATOMIC. Average flux variations across 10-100 km were roughly 50%, 10%, and 25%, respectively. Larger proportional changes of sensible heat flux across SST gradients, compared to latent heat flux, have previously been observed in an area of stronger SST variability (Shao et al., 2019). SST gradients drive a significant portion of the sensible heat flux variability, up to 5 Wm^{-2} (Figure 3.11). Air temperature variations also significantly contribute to sensible heat flux variations. The effect of SST on latent heat flux variability is masked by the strong impact of humidity variations on latent heat flux (Figure 3.11). Wind speed variability only has a small influence on spatial latent heat flux variability, and a negligible influence on variations of sensible heat or upward buoyancy fluxes. Unlike SST gradients, atmospheric gradients in temperature, humidity, and wind speed result from a combination of turbulent fluctuations as well as fronts, atmospheric convective systems, and cold pools and exist on short spatiotemporal scales. These findings are significant because the spatial scales of variability observed here (10-100 km) are small compared to most global models and some satellite products. Lower resolution models and satellite products would not resolve the observed variability in SST, air temperature, air humidity, and therefore fluxes in the tropical Atlantic trade wind region due to small spatial scale (i.e., sub-footprint-scale or sub-grid-scale) gradients.

3.5.1 Comparisons with a composite satellite product

To gain insight into the potential uncertainty or error associated with lower resolution products in the presence of small-scale SST, atmospheric, and flux gradients, we make comparisons between bulk fluxes estimated from the v4 SWIFT observations using COARE 3.6 and fluxes estimated using observed atmospheric observations and SST observations

from GHRSST-OSTIA, which have been shown to be consistent with observed SST during ATOMIC on the satellite grid scale with only a small varying bias < 0.2 °C (Wick et al., 2022). Results from the current analysis are shown in Figure 3.12. Figure 3.12a, b, and c show OV fluxes from SWIFT observations from 15 January 08:00 UTC to 17 January 08:00 UTC; i.e., the same as shown in Figure 3.8c,f,i. Figure 3.12d, e, and f show fluxes calculated using COARE 3.6 with regionally-averaged SWIFT atmospheric observations and interpolated satellite SST observed on 15-17 January as inputs. Figure 3.12g compares SST observed by the SWIFTs and the satellite product.

Qualitatively, the SWIFT and satellite SST show the same spatial trends: both show evidence of a central warm tongue with areas of relatively colder water to the north and south. However, comparisons of the histogram plots demonstrate that the SWIFT observations were associated with significantly stronger SST gradients and flux differences across the SST gradient than the satellite product resolves. Sensible heat fluxes estimated from the SWIFT observations differed, on average, by 3.7 Wm^{-2} between relatively warm (SST > 26.4°C) and cold (SST < 26.4°C) water. This difference was only 1.7 Wm^{-2} when estimated from interpolated satellite SST instead of observed SWIFT SST (Figure 3.12a,d). Similarly, latent heat fluxes and upward buoyancy fluxes differed, on average, by 11.7 Wm^{-2} and 4.6 Wm^{-2} in the SWIFT observations but only 5.7 Wm^{-2} and 2.2 Wm^{-2} when using satellite SST (Figure 3.12b,c,e,f). Because the SST gradient was persistent for a longer period of time (2 days) than the temporal resolution of the satellite observations (daily), this discrepancy is likely because the satellite spatial resolution is too coarse rather than unresolved temporal variability. In short, in this case, satellite observations resolve the general pattern of variability associated with this SST gradient but do not resolve its magnitude or sharpness. The result is that the satellite SST observations lead to underestimation in spatial flux differences across the SST front by over 50% compared to the SWIFT observations. While there was a significant difference in observed flux gradients derived from the satellite and SWIFT observations, average fluxes throughout the domain were very similar for both cases and thus satellite SST observations are likely sufficient for analyzing larger-scale variations in this region.

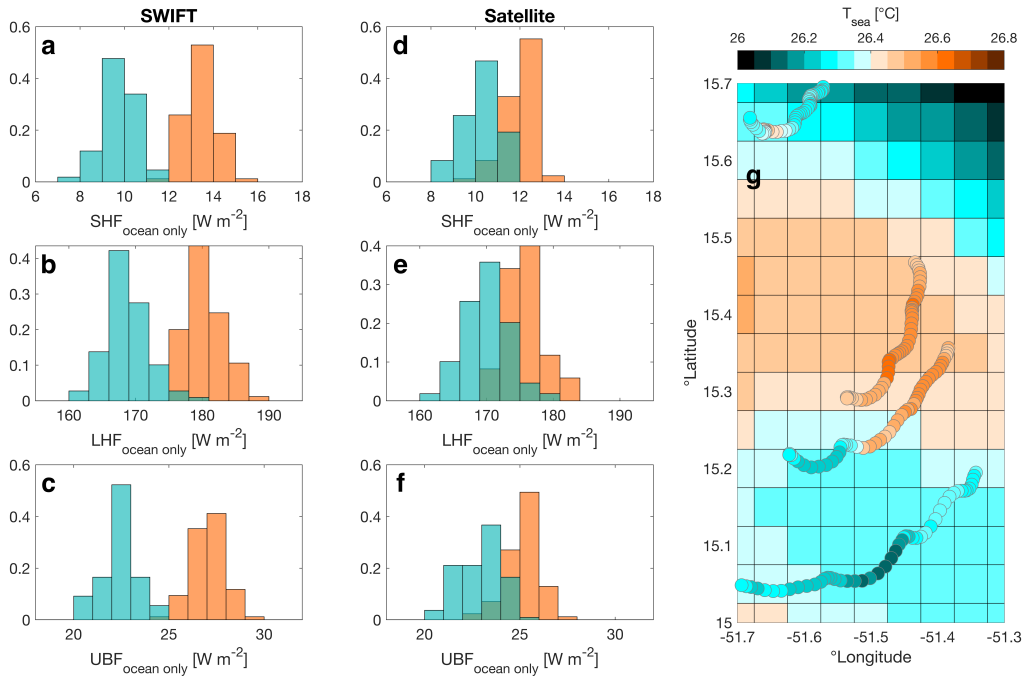

Figure 3.12: Histograms of "ocean variability only" (OV) (a) sensible heat flux, (b) latent heat flux, and (c) upward buoyancy flux in areas with warm SST ($>$ 26.4°C; orange bars) and cold SST ($<$ 26.4°C; blue bars) observed by v4 SWIFTs from 15-17 Jan 2020. (d-f) are the same as (a-c), except using interpolated GHRSST OSTIA Level 4 satellite SST instead of SWIFT observations as inputs into COARE to calculate fluxes. (g) Map of observed SWIFT SST (15-17 Jan 2020) and GHRSST OSTIA Level 4 satellite SST (16 Jan 2020).

Comparisons between SWIFT observations from case study 3 and the widely-used 1° by 1° OAFlux (Yu and Weller, 2007; Yu, 2019) sensible and latent heat fluxes from 16 January also yielded similar results: approximately 70% of the observed spatial sensible plus latent heat flux variability was not resolved by OAFlux estimates (not shown). This analysis suggests that when submesoscale SST gradients are not resolved in these tropical trade wind conditions, the spatial variations of air-sea fluxes across those scales will also be underestimated.

3.5.2 Summary

SST variability as high as 0.7°C across scales of 10 to 100 km was commonly observed at the ATOMIC study site in the boreal winter trade wind conditions of the northwestern tropical Atlantic, despite the fact that this region is not associated with strong mesoscale ocean activity and significant river outflow is not observed at this time of year. SST gradients were associated with air-sea flux variability of tens of Wm^{-2} on the same spatial scales. Across SST gradients, sensible heat fluxes varied by up to 200% (10 Wm^{-2}), while latent heat and upward buoyancy fluxes varied by up to 30% (50 Wm^{-2}) and 60% (10 Wm^{-2}), respectively. Sensible heat and upward buoyancy flux gradients vary primarily depending on the strength and relative sign of the gradients in SST and air temperature. The case study analysis demonstrates that SST gradients were sometimes the primary contributor to systematic spatial gradients in air-sea sensible heat fluxes, more so than wind speed or air temperature. In other words, SST gradients were often strong enough and persistent enough to sustain spatial sensible heat flux gradients despite atmospheric effects to eliminate these gradients. On the other hand, air humidity variability was a much stronger driver of latent heat flux gradients than SST; i.e., the influence of humidity variability often counteracted and sometimes reversed the influence of SST (q_{sea}) on latent heat flux. As a result, spatial variability in latent heat fluxes was uncorrelated with SST. Spatial variations in wind speed were not strongly correlated with spatial variations in fluxes during this field campaign.

Comparisons with a satellite SST product show that the sharpness and magnitude of SST and air-sea flux differences on scales of tens of kilometers are likely underestimated with microwave satellite observations or coarse resolution models. This finding highlights the importance of using high resolution ($<$ 10 km) ocean and atmospheric measurements in air-sea flux studies and models in regions where ocean submesoscale variability exists. Calculating fluxes from lower resolution remote sensing observations will not capture small-scale gradients in fluxes or their components such as those highlighted in these case studies. Thus, lower resolution satellite and model products will likely not resolve the aggregate

influence of small-scale features on larger-scale air-sea fluxes, weather, ocean dynamics, or climate. Spatial gradients in fluxes and their thermodynamic components were significant in the northwestern tropical Atlantic trade wind region even though SST fronts are relatively less common and weaker here compared to other regions (Mauzole, 2022). These results may be representative of other tropical trade wind regions, which cover a significant portion of the earth. The spatial variability of air-sea fluxes is likely larger or may behave differently in areas with stronger SST fronts and/or different atmospheric patterns, such as coastal regions, across tropical instability waves, near strong boundary currents, and at higher latitudes.

CONCLUSION

This dissertation provides insight into the physical processes which govern the spatial and temporal variability of small-scale air-sea interaction in the tropics, an important but often unresolved component of the global climate system. The first chapter investigates the link in the global water cycle between small-scale precipitation and near-surface salinity, while the second and third chapters consider the influence of small-scale ocean variability on air-sea heat, momentum, and buoyancy fluxes. In combination, these studies explore the dominant components air-sea interaction in two distinct regimes of the tropical ocean.

The first study examined the link between precipitation and near-surface salinity in the eastern Pacific ITCZ. While previous studies have shown that salinity following rainfall is related to the wind speed and rain rate, Chapter 1 provides a more comprehensive analysis of the factors that control freshening following tropical rainfall by considering different atmospheric rain modes and preexisting upper ocean stratification. An idealized 1-dimensional model analysis demonstrated that the patterns of convective and stratiform rainfall within rain events and the presence of preexisting stratification can significantly influence the persistence of salinity anomalies following rain, with the influence of preexisting stratification on the salinity response to rain being much stronger than the type of rainfall. The mechanism by which this occurs is stratification itself: stratification, whether preexisting or generated by intense convective rain, inhibits turbulence and downward mixing thereby confining freshwater to a layer close to the surface (Figure C). These findings suggest that more comprehensive predictions of the salinity response to rainfall may be necessary, as rain rate and wind speed alone do not necessarily accurately predict the salinity response to rain. This is particularly important in the tropics, where multiple modes of rainfall occur and preexisting stratification is frequent.

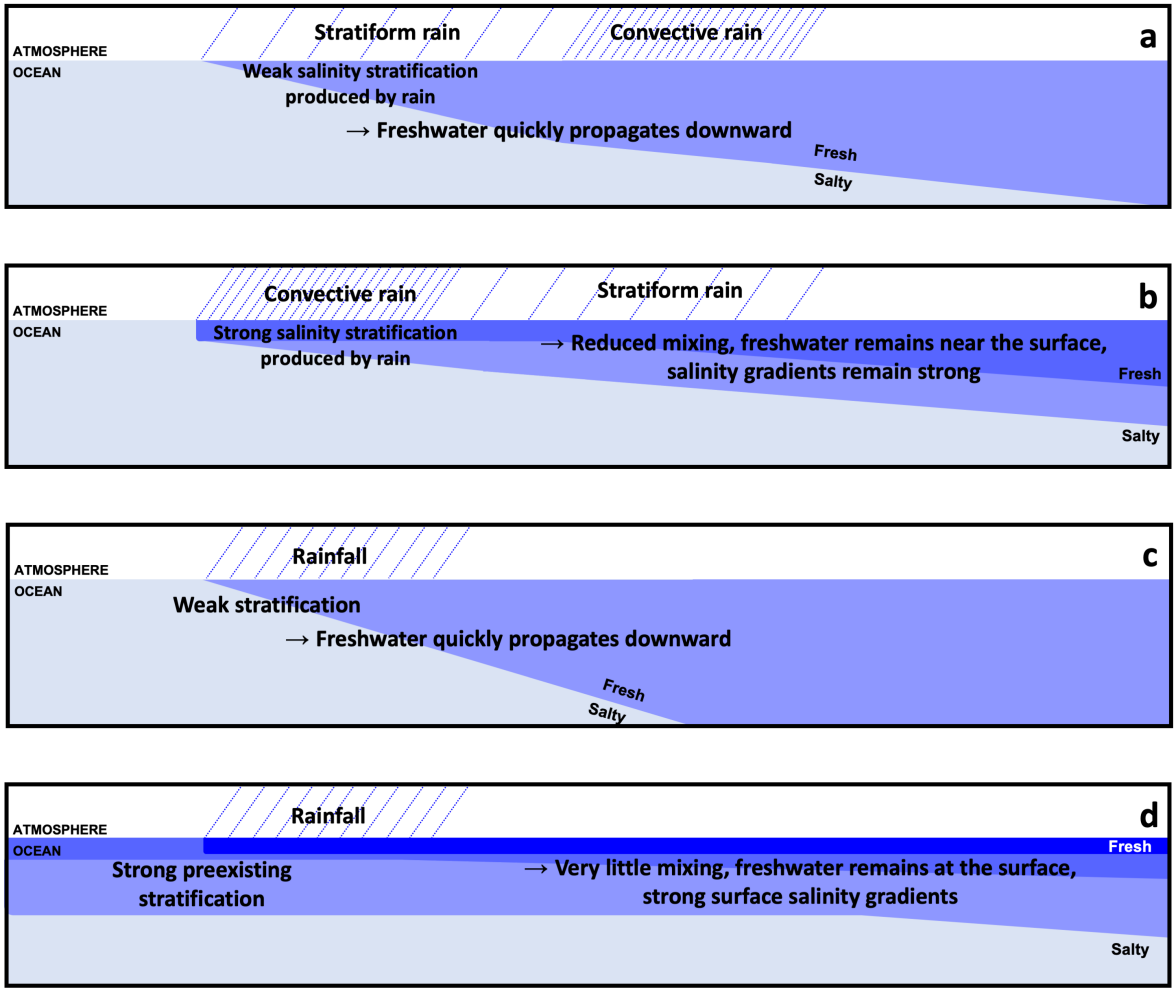

Figure C: Schematics representing the mixed layer salinity structure following (a) convective with leading stratiform rain, (b) convective with trailing stratiform rain, (c) rain on a well-mixed ocean, and (d) rain on an ocean with preexisting stratification.

The second study investigated the influence of wave-current interactions on wave slope and momentum flux in the northwestern tropical Atlantic trade wind region, a region of moderate submesoscale activity away from the coast and strong boundary currents. A comparison of wave slope and momentum flux derived from wave spectral observations across different surface current speeds and directions demonstrated that wave slope and momentum flux are elevated when currents and waves are in opposition, but decreased when currents and waves are in the same direction due to a combination of changes to the current-relative wind speed and wave-current interactions. While this has been shown in localized energetic environments with strong current gradients, it has not been observed in the open ocean away from such features and thus may influence air-sea interaction throughout larger regions of the world ocean. Comparisons between the observed momentum flux under varying current conditions and bulk fluxes from the COARE algorithm, which incorporates the change in the current-relative wind speed but not wave-current interactions, suggests that wave-current interactions modify momentum flux by at least up to 6% in the open ocean in a region of relatively constant winds. This value, which is likely much larger in areas of stronger current gradients, is a significant contribution and suggests that presently-used wave and air-sea flux parameterizations may have significant uncertainty in both areas of strong current gradients and in the open ocean.

The final study explored the variability of bulk air-sea heat, moisture, and buoyancy fluxes across submesoscale SST gradients in the northwestern tropical Atlantic. Using a unique suite of SWIFT and Wave Glider observations, spatial flux gradients were estimated across identified SST gradients on scales of tens of kilometers or smaller. Sensible heat and buoyancy fluxes were strongly driven by ocean variability, while latent heat fluxes were instead primarily driven by high-frequency atmospheric variability. No significant wind response was observed across SST gradients, although air temperatures were generally warmer on the warm side of SST gradients implying that the atmosphere equilibrates to SST gradients to some degree. Overall, these findings demonstrate that ocean gradients have a non-negligible influence on the small-scale spatial variability of air-sea fluxes and show the

importance of resolving small-scale features in global-scale applications. Satellite observations underrepresent the observed variability in the Atlantic trade wind region, which suggests that lower-resolution satellite products and models may have uncertainty resulting from the collective influence of small-scale SST gradients on air-sea fluxes.

As a whole, these findings motivate several future research avenues. First, the improved resolution in satellite observations is necessary to understand the importance of small-scale air-sea interaction in the context of the larger scale. Chapter 1 demonstrates that high-resolution observations of rain and near-surface stratification would be needed to accurately predict how freshwater mixes into the upper ocean following rainfall and, in-turn, fully understand this link in the global water cycle. Chapters 2 and 3 demonstrate that surface current and SST variability on scales of tens of kilometers can influence air-sea fluxes on those same scales. Current global models and satellites typically resolve larger mesoscale features (scales of around 100 km), but do not fully resolve smaller-scale variability. If the resolution of satellite sea surface salinity, SST and rain observations was improved to around 10 km, this would capture many intense convective rain cells present in the ITCZ as well as the majority of the prominent ocean features present in the trade winds. Ultimately, higher resolution global-scale observations would make it possible to incorporate small-scale variability into models and quantify the influence of these features on larger and global-scale dynamics and climate.

The findings of this dissertation also motivate research on the mesoscale processes that bridge small and larger-scale dynamics in order to characterize air-sea interaction on scales too large to typically observe in situ but too small to be incorporated into many global models. One such approach would be additional field efforts to deploy additional in situ platforms including surface moorings, drifters, and autonomous profilers. Deploying surface moorings spaced between 5 and 50 km apart would allow for the resolution of ocean and atmospheric variability on a range of scales and make it possible to characterize the typical observed variability on these scales. This could be done in both areas of strong current and sea surface temperature variability as well as areas not generally associated with this vari-

ability such as the trade winds. Additional deployments of surface drifters and autonomous vehicles may also be useful for improved spatial coverage. Such an effort could provide the basis for a multi-scale analysis and build upon the work presented in this dissertation. Furthermore, this would complement improved higher-resolution satellite observations with additional observations in the atmosphere and at deeper depths. A different approach would be intensive 3-dimensional regional coupled modeling efforts focused on understanding the interplay between atmospheric and ocean variability on scales of tens of kilometers.

Finally, improvements to small-scale and 1-D models are necessary to comprehensively understand small-scale air-sea interaction. Chapter 2 demonstrates that wave-current interactions, a process not incorporated into the COARE parameterizations or most models, can significantly influence momentum flux even in the open ocean away from strong gradients. The continued development of fully-coupled wave-atmosphere-ocean models that incorporate wave-current interactions would allow for additional composite analyses to be performed that comprehensively quantify the collective impact of these small-scale processes on submesoscale and mesoscale air-sea interaction and atmospheric dynamics.

BIBLIOGRAPHY

Agrawal, Y. C., Terray, E. A., Donelan, M. A., Hwang, P. A., Williams III, A. J., Drennan, W. M., Kahma, K. K., and Kitaigorodskii, S. A. (1992). Enhanced dissipation of kinetic energy beneath surface waves. *Nature*, 359(6392):219. https://doi.org/10.1038/359219a0.

Akan, Ç., McWilliams, J. C., Moghimi, S., and Özkan-Haller, H. T. (2018). Frontal dynamics at the edge of the Columbia River plume. *Ocean Modelling*, 122:1–12. https://doi.org/10.1016/j.ocemod.2017.12.001.

Akan, Ç., Moghimi, S., Özkan-Haller, H. T., Osborne, J., and Kurapov, A. (2017). On the dynamics of the mouth of the Columbia River: Results from a three-dimensional fully coupled wave-current interaction model. *Journal of Geophysical Research: Oceans*, 122(7):5218–5236. https://doi.org/10.1002/2016JC012307.

Anderson, J. E. and Riser, S. C. (2014). Near-surface variability of temperature and salinity in the near-tropical ocean: Observations from profiling floats. *Journal of Geophysical Research: Oceans*, 119(11):7433–7448. https://doi.org/10.1002/2014JC010112.

Ardhuin, F., Chapron, B., and Elfouhaily, T. (2004). Waves and the air–sea momentum budget: Implications for ocean circulation modeling. *Journal of Physical Oceanography*, 34(7):1741–1755. https://doi.org/10.1175/1520-0485(2004)034¡1741:WATAMB¿2.0.CO;2.

Ardhuin, F., Gille, S. T., Menemenlis, D., Rocha, C. B., Rascle, N., Chapron, B., Gula, J., and Molemaker, J. (2017). Small-scale open ocean currents have large effects on wind wave heights. *Journal of Geophysical Research: Oceans*, 122(6):4500–4517. https://doi.org/10.1002/2016JC012413.

Asher, W., Karle, L., Higgins, B., Farley, P., Monahan, E., and Leifer, I. (1996). The

influence of bubble plumes on air-seawater gas transfer velocities. *Journal of Geophysical Research: Oceans*, 101(C5):12027–12041. https://doi.org/10.1029/96JC00121.

Asher, W. E., Jessup, A. T., and Clark, D. (2014). Stable near-surface ocean salinity stratifications due to evaporation observed during STRASSE. *Journal of Geophysical Research: Oceans*, 119(5):3219–3233. https://doi.org/10.1002/2014JC009808.

Banihashemi, S. and Kirby, J. T. (2019). Approximation of wave action conservation in vertically sheared mean flows. *Ocean Modelling*, 143:101460. https://doi.org/10.1016/j.ocemod.2019.101460.

Banihashemi, S., Kirby, J. T., and Dong, Z. (2017). Approximation of wave action flux velocity in strongly sheared mean flows. *Ocean Modelling*, 116:33–47. https://doi.org/10.1016/j.ocemod.2017.06.002.

Banner, M. L. (1990). Equilibrium spectra of wind waves. *Journal of Physical Oceanography*, 20(7):966–984. https://doi.org/10.1175/1520-0485(1990)020¡0966:ESOWW¿2.0.CO;2.

Banner, M. L., Gemmrich, J. R., and Farmer, D. M. (2002). Multiscale measurements of ocean wave breaking probability. *Journal of physical oceanography*, 32(12):3364–3375. https://doi.org/10.1175/1520-0485(2002)032¡3364:MMOOWB¿2.0.CO;2.

Banner, M. L. and Morison, R. P. (2010). Refined source terms in wind wave models with explicit wave breaking prediction. Part I: Model framework and validation against field data. *Ocean Modelling*, 33(1-2):177–189. https://doi.org/10.1016/j.ocemod.2010.01.002.

Bingham, F. M., Li, Z., Katsura, S., and Sprintall, J. (2020). Barrier layers in a high-resolution model in the eastern tropical Pacific. *Journal of Geophysical Research: Oceans*, 125(12):e2020JC016643. https://doi.org/10.1029/2020JC016643.

Bishop, S. P., Small, R. J., Bryan, F. O., and Tomas, R. A. (2017). Scale dependence of midlatitude air–sea interaction. *Journal of Climate*, 30(20):8207–8221. https://doi.org/10.1175/JCLI-D-17-0159.1.

Boutin, J., Chao, Y., Asher, W., Delcroix, T., Drucker, R., Drushka, K., Kolodziejczyk, N., Lee, T., Reul, N., Reverdin, G., et al. (2016). Satellite and in situ salinity: Understanding near-surface stratification and subfootprint variability. *Bulletin of the American Meteorological Society*, 97(8):1391–1407. https://doi.org/10.1002/2014JC010070.

Boutin, J., Martin, N., Reverdin, G., Morisset, S., Yin, X., Centurioni, L., and Reul, N. (2014). Sea surface salinity under rain cells: SMOS satellite and in situ drifters observations. *Journal of Geophysical Research: Oceans*, 119(8):5533–5545.

Boutin, J., Martin, N., Reverdin, G., Yin, X., and Gaillard, F. (2013). Sea surface freshening inferred from SMOS and ARGO salinity: impact of rain. *Ocean Science*, 9(1). https://doi.org/10.5194/os-9-183-2013.

Boyer, T. P., Levitus, S., Antonov, J. I., Locarnini, R. A., and Garcia, H. E. (2005). Linear trends in salinity for the world ocean, 1955–1998. *Geophysical Research Letters*, 32(1). https://doi.org/10.1029/2004GL021791.

Brainerd, K. and Gregg, M. (1993). Diurnal restratification and turbulence in the oceanic surface mixed layer: 1. Observations. *Journal of Geophysical Research: Oceans*, 98(C12):22645–22656. https://doi.org/10.1029/93JC02297.

Branch, R. A., Horner-Devine, A. R., Akan, C., Chickadel, C. C., Farquharson, G., Hudson, A., Talke, S. A., Thomson, J., and Jessup, A. T. (2018). Airborne LiDAR measurements and model simulations of tides, waves, and surface slope at the mouth of the Columbia River. *IEEE Transactions on Geoscience and Remote Sensing*, 56(12):7038–7048. https://doi.org/10.1109/TGRS.2018.2847561.

Bryan, F. O., Tomas, R., Dennis, J. M., Chelton, D. B., Loeb, N. G., and McClean, J. L. (2010). Frontal scale air–sea interaction in high-resolution coupled climate models. *Journal of Climate*, 23(23):6277–6291. https://doi.org/10.1175/2010JCLI3665.1.

Burchard, H. and Bolding, K. (2001). Comparative analysis of four second-moment turbulence closure models for the oceanic mixed layer. *Journal of Physical Oceanography*, 31(8):1943–1968. https://doi.org/10.1175/1520-0485(2001)031¡1943:CAOFSM¿2.0.CO;2.

Burchard, H., Bolding, K., and Villarreal, M. R. (1999). *GOTM, a general ocean turbulence model: theory, implementation and test cases*. Space Applications Institute.

Businger, J. and Shaw, W. (1984). The response of the marine boundary layer to mesoscale variations in sea-surface temperature. *Dynamics of Atmospheres and Oceans*, 8(3-4):267–281. https://doi.org/10.1016/0377-0265(84)90012-5.

Callaghan, A. H., Ward, B., and Vialard, J. (2014). Influence of surface forcing on near-surface and mixing layer turbulence in the tropical Indian Ocean. *Deep Sea Research Part I: Oceanographic Research Papers*, 94:107–123. https://doi.org/10.1016/j.dsr.2014.08.009.

Campana, J., Terrill, E. J., and De Paolo, T. (2016). The development of an inversion technique to extract vertical current profiles from X-band radar observations. *Journal of Atmospheric and Oceanic Technology*, 33(9):2015–2028. https://doi.org/10.1175/JTECH-D-15-0145.1.

Capet, X., McWilliams, J. C., Molemaker, M. J., and Shchepetkin, A. F. (2008). Mesoscale to submesoscale transition in the california current system. part i: Flow structure, eddy flux, and observational tests. *Journal of physical oceanography*, 38(1):29–43. https://doi.org/10.1175/2007JPO3671.1.

Chawla, A. and Kirby, J. T. (2002). Monochromatic and random wave breaking at blocking points. *Journal of Geophysical Research: Oceans*, 107(C7):4–1. https://doi.org/10.1029/2001JC001042.

Chelton, D. B., Esbensen, S. K., Schlax, M. G., Thum, N., Freilich, M. H., Wentz, F. J., Gentemann, C. L., McPhaden, M. J., and Schopf, P. S. (2001). Observations of coupling between surface wind stress and sea surface temperature in the eastern

tropical Pacific. *Journal of Climate*, 14(7):1479–1498. https://doi.org/10.1175/1520-0442(2001)014¡1479:OOCBSW¿2.0.CO;2.

Chelton, D. B., Schlax, M. G., Freilich, M. H., and Milliff, R. F. (2004). Satellite measurements reveal persistent small-scale features in ocean winds. *Science*, 303(5660):978–983. https://doi.org/10.1126/science.1091901.

Chelton, D. B. and Xie, S.-P. (2010). Coupled ocean-atmosphere interaction at oceanic mesoscales. *Oceanography*, 23(4):52–69. https://doi.org/10.5670/oceanog.2010.05.

Chen, H. and Zou, Q. (2018). Characteristics of wave breaking and blocking by spatially varying opposing currents. *Journal of Geophysical Research: Oceans*, 123(5):3761–3785. https://doi.org/10.1029/2017JC013440.

Chiu, L. S., Chang, A. T., and Janowiak, J. (1993). Comparison of monthly rain rates derived from GPI and SSM/I using probability distribution functions. *Journal of Applied Meteorology*, 32(2):323–334. https://doi.org/10.1175/1520-0450(1993)032¡0323:COMRRD¿2.0.CO;2.

Choi, W. (2009). Nonlinear surface waves interacting with a linear shear current. *Mathematics and Computers in Simulation*, 80(1):29–36. https://doi.org/10.1016/j.matcom.2009.06.021.

Clayson, C., Edson, J., Paget, A., Graham, R., and Greenwood, B. (2019). Effects of rainfall on the atmosphere and ocean during SPURS-2. *Oceanography*, 32(2):86–97. https://doi.org/10.5670/oceanog.2019.216.

Coles, V. J., Brooks, M. T., Hopkins, J., Stukel, M. R., Yager, P. L., and Hood, R. R. (2013). The pathways and properties of the Amazon River Plume in the tropical North Atlantic Ocean. *Journal of Geophysical Research: Oceans*, 118(12):6894–6913. https://doi.org/10.1002/2013JC008981.

Collins, C., Potter, H., Lund, B., Tamura, H., and Graber, H. C. (2018). Directional wave spectra observed during intense tropical cyclones. *Journal of Geophysical Research: Oceans*, 123(2):773–793. https://doi.org/10.1002/2017JC012943.

Craig, P. D. and Banner, M. L. (1994). Modeling wave-enhanced turbulence in the ocean surface layer. *Journal of Physical Oceanography*, 24(12):2546–2559. https://doi.org/10.1175/1520-0485(1994)024¡2546:MWETIT¿2.0.CO;2.

de Szoeke, S. P., Skyllingstad, E. D., Zuidema, P., and Chandra, A. S. (2017). Cold pools and their influence on the tropical marine boundary layer. *Journal of the Atmospheric Sciences*, 74(4):1149–1168. https://doi.org/10.1175/JAS-D-16-0264.1.

Dellaripa, E. M. R. and Maloney, E. D. (2015). Analysis of mjo wind-flux feedbacks in the indian ocean using rama buoy observations. *Journal of the Meteorological Society of Japan. Ser. II*, 93:1–20. https://doi.org/10.2151/jmsj.2015-021.

DeMott, C. A., Benedict, J. J., Klingaman, N. P., Woolnough, S. J., and Randall, D. A. (2016). Diagnosing ocean feedbacks to the mjo: Sst-modulated surface fluxes and the moist static energy budget. *Journal of Geophysical Research: Atmospheres*, 121(14):8350–8373. https://doi.org/10.1002/2016JD025098.

Drucker, R. and Riser, S. C. (2014). Validation of Aquarius sea surface salinity with Argo: Analysis of error due to depth of measurement and vertical salinity stratification. *Journal of Geophysical Research: Oceans*, 119(7):4626–4637. https://doi.org/10.1002/2014JC010045.

Drushka, K., Asher, W. E., Jessup, A. T., Thompson, E. J., Iyer, S., and Clark, D. (2019). Capturing fresh layers with the surface salinity profiler. *Oceanography*, 32(2):76–85. https://doi.org/10.5670/oceanog.2019.215.

Drushka, K., Asher, W. E., Ward, B., and Walesby, K. (2016). Understanding the formation

and evolution of rain-formed fresh lenses at the ocean surface. *Journal of Geophysical Research: Oceans*, 121(4):2673–2689. https://doi.org/10.1002/2015JC011527.

Durack, P. J. (2015). Ocean salinity and the global water cycle. *Oceanography*, 28(1):20–31.

Durack, P. J., Wijffels, S. E., and Matear, R. J. (2012). Ocean salinities reveal strong global water cycle intensification during 1950 to 2000. *Science*, 336(6080):455–458. https://doi.org/10.1126/science.1212222.

Ebuchi, N. and Hanawa, K. (2000). Mesoscale eddies observed by TOLEX-ADCP and TOPEX/POSEIDON altimeter in the Kuroshio recirculation region south of Japan. *Journal of Oceanography*, 56(1):43–57. https://doi.org/10.1023/A:1011110507628.

Edson, J. B., Jampana, V., Weller, R. A., Bigorre, S. P., Plueddemann, A. J., Fairall, C. W., Miller, S. D., Mahrt, L., Vickers, D., and Hersbach, H. (2013). On the exchange of momentum over the open ocean. *Journal of Physical Oceanography*, 43(8):1589–1610. https://doi.org/10.1175/JPO-D-12-0173.1.

Ellingsen, S. Å. and Li, Y. (2017). Approximate dispersion relations for waves on arbitrary shear flows. *Journal of Geophysical Research: Oceans*, 122(12):9889–9905. https://doi.org/10.1002/2017JC012994.

Fairall, C. W., Bradley, E. F., Hare, J., Grachev, A. A., and Edson, J. B. (2003). Bulk parameterization of air–sea fluxes: Updates and verification for the COARE algorithm. *Journal of Climate*, 16(4):571–591. https://doi.org/10.1175/1520-0442(2003)016¡0571:BPOASF¿2.0.CO;2.

Fairall, C. W., Bradley, E. F., Rogers, D. P., Edson, J. B., and Young, G. S. (1996). Bulk parameterization of air-sea fluxes for tropical ocean-global atmosphere coupled-ocean atmosphere response experiment. *Journal of Geophysical Research: Oceans*, 101(C2):3747–3764. https://doi.org/10.1029/95JC03205.

Farrar, J. (2020). SPURS-2 Central mooring CTD, surface flux and meteorological data for the E. Tropical Pacific field campaign. Ver. 1.0. PO.DAAC, CA, USA.

Farrar, J. T. and Plueddemann, A. J. (2019). On the factors driving upper-ocean salinity variability at the western edge of the Eastern Pacific Fresh Pool. *Oceanography*, 32(2):30–39. https://doi.org/10.5670/ oceanog.2019.209.

Ffield, A. (2005). North Brazil current rings viewed by TRMM Microwave Imager SST and the influence of the Amazon Plume. *Deep Sea Research Part I: Oceanographic Research Papers*, 52(1):137–160. https://doi.org/10.1016/j.dsr.2004.05.013.

Fisher, A. W., Sanford, L. P., Scully, M. E., and Suttles, S. E. (2017). Surface wave effects on the translation of wind stress across the air–sea interface in a fetch-limited, coastal embayment. *Journal of Physical Oceanography*, 47(8):1921–1939. https://doi.org/10.1175/JPO-D-16-0146.1.

Fratantoni, D. M. and Glickson, D. A. (2002). North Brazil Current ring generation and evolution observed with SeaWiFS. *Journal of Physical Oceanography*, 32(3):1058–1074. https://doi.org/10.1175/1520-0485(2002)032¡1058:NBCRGA¿2.0.CO;2.

Fratantoni, D. M. and Richardson, P. L. (2006). The evolution and demise of North Brazil Current rings. *Journal of Physical Oceanography*, 36(7):1241–1264. https://doi.org/10.1175/JPO2907.1.

Friehe, C., Shaw, W., Rogers, D., Davidson, K., Large, W., Stage, S., Crescenti, G., Khalsa, S., Greenhut, G., and Li, F. (1991). Air-sea fluxes and surface layer turbulence around a sea surface temperature front. *Journal of Geophysical Research: Oceans*, 96(C5):8593–8609. https://doi.org/10.1029/90JC02062.

Gao, Y., Klingaman, N. P., DeMott, C. A., and Hsu, P.-C. (2019). Diagnosing ocean feedbacks to the bsiso: Sst-modulated surface fluxes and the moist static

energy budget. *Journal of Geophysical Research: Atmospheres*, 124(1):146–170. https://doi.org/10.1029/2018JD029303.

Gaube, P., Chelton, D. B., Samelson, R. M., Schlax, M. G., and O'Neill, L. W. (2015). Satellite observations of mesoscale eddy-induced Ekman pumping. *Journal of Physical Oceanography*, 45(1):104–132. https://doi.org/10.1175/JPO-D-14-0032.1.

Gemmrich, J. and Garrett, C. (2012). The signature of inertial and tidal currents in offshore wave records. *Journal of Physical Oceanography*, 42(6):1051–1056. https://doi.org/10.1175/JPO-D-12-043.1.

Gemmrich, J. and Pawlowicz, R. (2020). Wind Waves in the Strait of Georgia. *Atmosphere-Ocean*, 58(2):79–97. https://doi.org/10.1080/07055900.2020.1735989.

Haus, B. K. (2007). Surface current effects on the fetch-limited growth of wave energy. *Journal of Geophysical Research: Oceans*, 112(C3). https://doi.org/10.1029/2006JC003924.

Hayes, S., McPhaden, M., and Wallace, J. (1989). The influence of sea-surface temperature on surface wind in the eastern equatorial pacific: Weekly to monthly variability. *Journal of Climate*, 2(12):1500–1506. https://doi.org/10.1175/1520-0442(1989)002¡1500:TIOSST¿2.0.CO;2.

Hegermiller, C. A., Warner, J. C., Olabarrieta, M., and Sherwood, C. R. (2019). Wave–Current Interaction between Hurricane Matthew Wave Fields and the Gulf Stream. *Journal of Physical Oceanography*, 49(11):2883–2900. https://doi.org/10.1175/JPO-D-19-0124.1.

Herrera, J., González, J., and Varela, R. (2019). Measuring a lagrangian drifter's slip with an onboard adcp. *MethodsX*, 6:1336–1342. https://doi.org/10.1016/j.mex.2019.05.032.

Hine, R., Willcox, S., Hine, G., and Richardson, T. (2009). The wave glider: A wave-powered autonomous marine vehicle. In *OCEANS 2009*, pages 1–6. IEEE. https://doi.org/10.23919/OCEANS.2009.5422129.

Holthuijsen, L. and Tolman, H. (1991). Effects of the Gulf Stream on ocean waves. *Journal of Geophysical Research: Oceans*, 96(C7):12755–12771. https://doi.org/10.1029/91JC00901.

Houze Jr, R. A. (1997). Stratiform precipitation in regions of convection: A meteorological paradox? *Bulletin of the American Meteorological Society*, 78(10):2179–2196. https://doi.org/10.1175/1520-0477(1997)078¡2179:SPIROC¿2.0.CO;2.

Houze Jr, R. A. (2004). Mesoscale convective systems. *Reviews of Geophysics*, 42(4). https://doi.org/10.1029/2004RG000150.

Iyer, S. and Drushka, K. (2021a). The influence of preexisting stratification and tropical rain modes on the mixed layer salinity response to rainfall. *Journal of Geophysical Research: Oceans*, 126(10):e2021JC017574. https://doi.org/10.1029/2021JC017574.

Iyer, S. and Drushka, K. (2021b). Turbulence within rain-formed fresh lenses during the SPURS-2 experiment. *Journal of Physical Oceanography*. https://doi.org/10.1175/JPO-D-20-0303.1.

Iyer, S., Drushka, K., and Rainville, L. (2021). Estimating turbulent kinetic energy dissipation rate using microstructure data from the ship-towed Surface Salinity Profiler. *Journal of Atmospheric and Oceanic Technology*, 38(1):77–89. https://doi.org/10.1175/JTECH-D-20-0002.1.

Iyer, S., Thomson, J., Thompson, E., and Drushka, K. (2022). Variations in wave slope and momentum flux from wave-current interactions in the tropical trade winds. *Journal of Geophysical Research: Oceans*, 127(3):e2021JC018003. https://doi.org/10.1029/2021JC018003.

Jacob, M. M., Jones, W. L., Santos-Garcia, A., Drushka, K., Asher, W. E., and Scavuzzo, C. M. (2019). Salinity Rain Impact Model (RIM) for SMAP. *IEEE Journal of Selected Topics in Applied Earth Observations and Remote Sensing*, 12(6):1679–1687. https://doi.org/10.1109/JSTARS.2019.2907275.

Janssen, P. A. (1989). Wave-induced stress and the drag of air flow over sea waves. *Journal of Physical Oceanography*, 19(6):745–754. https://doi.org/10.1175/1520-0485(1989)019¡0745:WISATD¿2.0.CO;2.

Jeffery, C., Robinson, I., and Woolf, D. (2010). Tuning a physically-based model of the air–sea gas transfer velocity. *Ocean Modelling*, 31(1-2):28–35. https://doi.org/10.1016/j.ocemod.2009.09.001.

Johnson, R. H., Ciesielski, P. E., and Cotturone, J. A. (2001). Multiscale variability of the atmospheric mixed layer over the western pacific warm pool. *Journal of the Atmospheric Sciences*, 58(18):2729–2750. https://doi.org/10.1175/1520-0469(2001)058¡2729:MVOTAM¿2.0.CO;2.

Juszko, B.-A., Marsden, R. F., and Waddell, S. R. (1995). Wind stress from wave slopes using Phillips equilibrium theory. *Journal of Physical Oceanography*, 25(2):185–203. https://doi.org/10.1175/1520-0485(1995)025¡0185:WSFWSU¿2.0.CO;2.

Kastner, S. E., Horner-Devine, A. R., and Thomson, J. (2018). The influence of wind and waves on spreading and mixing in the Fraser River plume. *Journal of Geophysical Research: Oceans*, 123(9):6818–6840. https://doi.org/10.1029/2018JC013765.

Katsura, S. and Sprintall, J. (2020). Seasonality and formation of barrier layers and associated temperature inversions in the Eastern Tropical North Pacific. *Journal of Physical Oceanography*, 50(3):791–808. https://doi.org/10.1175/JPO-D-19-0194.1.

Katsura, S., Sprintall, J., and Bingham, F. (2021). Upper Ocean Stratification in the Eastern Pacific during the SPURS-2 Field Campaign. *Journal of Geophysical Research: Oceans*, page e2020JC016591. https://doi.org/10.1029/2020JC016591.

Keeling, R. F. (1993). On the role of large bubbles in air-sea gas exchange and supersaturation in the ocean. *Journal of Marine Research*, 51(2):237–271. https://doi.org/10.1357/0022240933223800.

Kelly, K. A., Small, R. J., Samelson, R., Qiu, B., Joyce, T. M., Kwon, Y.-O., and Cronin, M. F. (2010). Western boundary currents and frontal air–sea interaction: Gulf stream and kuroshio extension. *Journal of Climate*, 23(21):5644–5667. https://doi.org/10.1175/2010JCLI3346.1.

Kim, S. Y. (2010). Observations of submesoscale eddies using high-frequency radar-derived kinematic and dynamic quantities. *Continental Shelf Research*, 30(15):1639–1655. https://doi.org/10.1016/j.csr.2010.06.011.

Kirby, J. T. and Chen, T.-M. (1989). Surface waves on vertically sheared flows: approximate dispersion relations. *Journal of Geophysical Research: Oceans*, 94(C1):1013–1027. https://doi.org/10.1029/JC094iC01p01013.

Kitaigorodskii, S. (1983). On the theory of the equilibrium range in the spectrum of wind-generated gravity waves. *Journal of Physical Oceanography*, 13(5):816–827. https://doi.org/10.1175/1520-0485(1983)013¡0816:OTTOTE¿2.0.CO;2.

Kudryavtsev, V., Yurovskaya, M., Chapron, B., Collard, F., and Donlon, C. (2017). Sun glitter imagery of surface waves. part 2: Waves transformation on ocean currents. *Journal of Geophysical Research: Oceans*, 122(2):1384–1399. https://doi.org/10.1002/2016JC012426.

Kummerow, C. (1998). Beamfilling errors in passive microwave rainfall retrievals. *Journal of Applied Meteorology*, 37(4):356–370. https://doi.org/10.1175/1520-0450(1998)037¡0356:BEIPMR¿2.0.CO;2.

Kwon, Y.-O., Alexander, M. A., Bond, N. A., Frankignoul, C., Nakamura, H., Qiu, B., and Thompson, L. A. (2010). Role of the gulf stream and kuroshio–oyashio systems in large-scale atmosphere–ocean interaction: A review. *Journal of Climate*, 23(12):3249–3281. https://doi.org/10.1175/2010JCLI3343.1.

Lambaerts, J., Lapeyre, G., Plougonven, R., and Klein, P. (2013). Atmospheric response

to sea surface temperature mesoscale structures. *Journal of Geophysical Research: Atmospheres*, 118(17):9611–9621. https://doi.org/10.1002/jgrd.50769.

Large, W. and Pond, S. (1981). Open ocean momentum flux measurements in moderate to strong winds. *Journal of Physical Oceanography*, 11(3):324–336. https://doi.org/10.1175/1520-0485(1981)011¡0324:OOMFMI¿2.0.CO;2.

Laurindo, L. C., Small, R. J., Thompson, L., Siqueira, L., Bryan, F. O., Chang, P., Danabasoglu, G., Kamenkovich, I. V., Kirtman, B. P., Wang, H., et al. (2022). Role of ocean and atmosphere variability in scale-dependent thermodynamic air-sea interactions. *Journal of Geophysical Research: Oceans*, page e2021JC018340. https://doi.org/10.1029/2021JC018340.

Laxague, N. J., Özgökmen, T. M., Haus, B. K., Novelli, G., Shcherbina, A., Sutherland, P., Guigand, C. M., Lund, B., Mehta, S., Alday, M., et al. (2018). Observations of near-surface current shear help describe oceanic oil and plastic transport. *Geophysical Research Letters*, 45(1):245–249. https://doi.org/10.1002/2017GL075891.

Lee, T. (2016). Consistency of Aquarius sea surface salinity with Argo products on various spatial and temporal scales. *Geophysical Research Letters*, 43(8):3857–3864. https://doi.org/10.1002/2016GL068822.

Lenain, L. and Melville, W. K. (2017). Measurements of the directional spectrum across the equilibrium saturation ranges of wind-generated surface waves. *Journal of Physical Oceanography*, 47(8):2123–2138. https://doi.org/10.1175/JPO-D-17-0017.1.

Lindzen, R. S. and Nigam, S. (1987). On the role of sea surface temperature gradients in forcing low-level winds and convergence in the tropics. *Journal of Atmospheric Sciences*, 44(17):2418–2436. https://doi.org/10.1175/1520-0469(1987)044¡2418:OTROSS¿2.0.CO;2.

Lygre, A. and Krogstad, H. E. (1986). Maximum entropy estimation of the directional

distribution in ocean wave spectra. *Journal of Physical Oceanography*, 16(12):2052–2060. https://doi.org/10.1175/1520-0485(1986)016¡2052:MEEOTD¿2.0.CO;2.

Mauzole, Y. (2022). Objective delineation of persistent sst fronts based on global satellite observations. *Remote Sensing of Environment*, 269:112798. https://doi.org/10.1016/j.rse.2021.112798.

McWilliams, J. C. (2016). Submesoscale currents in the ocean. *Proceedings of the Royal Society A: Mathematical, Physical and Engineering Sciences*, 472(2189):20160117. https://doi.org/10.1098/rspa.2016.0117.

McWilliams, J. C. (2018). Surface wave effects on submesoscale fronts and filaments. *Journal of Fluid Mechanics*, 843:479. https://doi.org/10.1017/jfm.2018.158.

Mellor, G. L. (1989). Retrospect on oceanic boundary layer modeling and second moment closure. In *Parameterization of Small-scale Processes. Proceedings of the Aha Hulikoa Hawaiian Winter Workshop, Honolulu, University of Hawaii at Manoa*, pages 251–271.

Melville, W. K. (1996). The role of surface-wave breaking in air-sea interaction. *Annual review of fluid mechanics*, 28(1):279–321. https://doi.org/10.1146/annurev.fl.28.010196.001431.

Minobe, S., Kuwano-Yoshida, A., Komori, N., Xie, S.-P., and Small, R. J. (2008). Influence of the gulf stream on the troposphere. *Nature*, 452(7184):206–209. https://doi.org/10.1038/nature06690.

Moghimi, S., Özkan-Haller, H. T., Akan, Ç., and Jurisa, J. T. (2019). Mechanistic analysis of the wave-current interaction in the plume region of a partially mixed tidal inlet. *Ocean Modelling*, 134:110–126. https://doi.org/10.1016/j.ocemod.2018.12.003.

Molinari, R. L., Spillane, M., Brooks, I., Atwood, D., and Duckett, C. (1981). Surface currents in the Caribbean Sea as deduced from Lagrangian observations. *Journal of Geophysical Research: Oceans*, 86(C7):6537–6542. https://doi.org/10.1029/JC086iC07p06537.

Moulin, A. J., Moum, J. N., and Shroyer, E. L. (2018). Evolution of turbulence in the diurnal warm layer. *Journal of Physical Oceanography*, 48(2):383–396. https://doi.org/10.1175/JPO-D-17-0170.1.

Niiler, P. P. and Paduan, J. D. (1995). Wind-driven motions in the northeast pacific as measured by lagrangian drifters. *Journal of Physical Oceanography*, 25(11):2819–2830. https://doi.org/10.1175/1520-0485(1995)025¡2819:WDMITN¿2.0.CO;2.

O'Neill, L. W., Chelton, D. B., Esbensen, S. K., and Wentz, F. J. (2005). High-resolution satellite measurements of the atmospheric boundary layer response to sst variations along the agulhas return current. *Journal of Climate*, 18(14):2706–2723. https://doi.org/10.1175/JCLI3415.1.

Parker, M. D. and Johnson, R. H. (2000). Organizational modes of midlatitude mesoscale convective systems. *Monthly weather review*, 128(10):3413–3436. https://doi.org/10.1175/1520-0493(2001)129¡3413:OMOMMC¿2.0.CO;2.

Paulson, C. and Simpson, J. (1981). The temperature difference across the cool skin of the ocean. *Journal of Geophysical Research: Oceans*, 86(C11):11044–11054. https://doi.org/10.1029/JC086iC11p11044.

Phillips, O. (1984). On the response of short ocean wave components at a fixed wavenumber to ocean current variations. *Journal of Physical Oceanography*, 14(9):1425–1433. https://doi.org/10.1175/1520-0485(1984)014¡1425:OTROSO¿2.0.CO;2.

Phillips, O. (1985). Spectral and statistical properties of the equilibrium range in wind-generated gravity waves. *Journal of Fluid Mechanics*, 156:505–531. https://doi.org/10.1017/S0022112085002221.

Pierce, D. W., Gleckler, P. J., Barnett, T. P., Santer, B. D., and Durack, P. J. (2012). The fingerprint of human-induced changes in the ocean's salinity and temperature fields. *Geophysical Research Letters*, 39(21). https://doi.org/10.1029/2012GL053389.

Pimentel, S., Haines, K., and Nichols, N. (2008). Modeling the diurnal variability of sea surface temperatures. *Journal of Geophysical Research: Oceans*, 113(C11). https://doi.org/10.1029/2007JC004607.

Pincus, R., Fairall, C. W., Bailey, A., Chen, H., Chuang, P. Y., de Boer, G., Feingold, G., Henze, D., Kalen, Q. T., Kazil, J., et al. (2021). Observations from the NOAA P-3 aircraft during ATOMIC. *Earth System Science Data*, 13(7):3281–3296. https://doi.org/10.5194/essd-2021-11.

Plant, W. J. (1982). A relationship between wind stress and wave slope. *Journal of Geophysical Research: Oceans*, 87(C3):1961–1967. https://doi.org/10.1029/JC087iC03p01961.

Portilla, J., Ocampo-Torres, F. J., and Monbaliu, J. (2009). Spectral partitioning and identification of wind sea and swell. *Journal of atmospheric and oceanic technology*, 26(1):107–122. https://doi.org/10.1175/2008JTECHO609.1.

Poulain, P.-M., Bussani, A., Gerin, R., Jungwirth, R., Mauri, E., Menna, M., and Notarstefano, G. (2013). Mediterranean surface currents measured with drifters: From basin to subinertial scales. *Oceanography*, 26(1):38–47. https://doi.org/10.5670/oceanog.2013.03.

Quilfen, Y. and Chapron, B. (2019). Ocean surface wave-current signatures from satellite altimeter measurements. *Geophysical Research Letters*, 46(1):253–261. https://doi.org/10.1029/2018GL081029.

Quilfen, Y., Yurovskaya, M., Chapron, B., and Ardhuin, F. (2018). Storm waves focusing and steepening in the Agulhas current: Satellite observations and modeling. *Remote Sensing of Environment*, 216:561–571. https://doi.org/10.1016/j.rse.2018.07.020.

Quinn, P. K., Thompson, E. J., Coffman, D. J., Baidar, S., Bariteau, L., Bates, T. S., Bigorre, S., Brewer, A., de Boer, G., de Szoeke, S. P., et al. (2021). Measurements from the RV Ronald H. Brown and related platforms as part of the Atlantic Tradewind Ocean-

Atmosphere Mesoscale Interaction Campaign (ATOMIC). *Earth System Science Data*, 13(4):1759–1790. https://doi.org/10.5194/essd-13-1759-2021.

Rapizo, H., Durrant, T. H., and Babanin, A. V. (2018). An assessment of the impact of surface currents on wave modeling in the Southern Ocean. *Ocean Dynamics*, 68(8):939–955. https://doi.org/10.1007/s10236-018-1171-7.

Rascle, N., Chapron, B., Ponte, A., Ardhuin, F., and Klein, P. (2014). Surface roughness imaging of currents shows divergence and strain in the wind direction. *Journal of Physical Oceanography*, 44(8):2153–2163. https://doi.org/10.1175/JPO-D-13-0278.1.

Rascle, N., Molemaker, J., Marié, L., Nouguier, F., Chapron, B., Lund, B., and Mouche, A. (2017). Intense deformation field at oceanic front inferred from directional sea surface roughness observations. *Geophysical Research Letters*, 44(11):5599–5608. https://doi.org/10.1002/2017GL073473.

Redelsperger, J.-L., Bouin, M.-N., Pianezze, J., Garnier, V., and Marié, L. (2019). Impact of a sharp, small-scale SST front on the marine atmospheric boundary layer on the Iroise Sea: Analysis from a hectometric simulation. *Quarterly Journal of the Royal Meteorological Society*, 145(725):3692–3714. https://doi.org/10.1002/qj.3650.

Reul, N., Fournier, S., Boutin, J., Hernandez, O., Maes, C., Chapron, B., Alory, G., Quilfen, Y., Tenerelli, J., Morisset, S., et al. (2014). Sea surface salinity observations from space with the SMOS satellite: A new means to monitor the marine branch of the water cycle. *Surveys in Geophysics*, 35(3):681–722. http://dx.doi.org/10.1007/s10712-013-9244-0.

Reverdin, G., Olivier, L., Foltz, G., Speich, S., Karstensen, J., Horstmann, J., Zhang, D., Laxenaire, R., Carton, X., Branger, H., et al. (2021). Formation and evolution of a freshwater plume in the northwestern tropical Atlantic in February 2020. *Journal of Geophysical Research: Oceans*, 126(4):e2020JC016981. https://doi.org/10.1029/2020JC016981.

Reverdin, G., Supply, A., Drushka, K., Thompson, E., Asher, W., and Lourenço, A. (2020). Intense and small freshwater pools from rainfall investigated during SPURS-2 on november 9 2017 in the eastern tropical Pacific. *Journal of Geophysical Research: Oceans*, page e2019JC015558. https://doi.org/10.1029/2019JC015558.

Rickenbach, T. M. and Rutledge, S. A. (1998). Convection in TOGA COARE: Horizontal scale, morphology, and rainfall production. *Journal of the Atmospheric Sciences*, 55(17):2715–2729. https://doi.org/10.1175/1520-0469(1998)055¡2715:CITCHS¿2.0.CO;2.

Romero, L., Hypolite, D., and McWilliams, J. C. (2020). Submesoscale current effects on surface waves. *Ocean Modelling*, 153:101662. https://doi.org/10.1016/j.ocemod.2020.101662.

Romero, L., Hypolite, D., and McWilliams, J. C. (2021). Representing wave effects on currents. *Ocean Modelling*, page 101873. https://doi.org/10.1016/j.ocemod.2021.101873.

Romero, L., Lenain, L., and Melville, W. K. (2017). Observations of surface wave–current interaction. *Journal of Physical Oceanography*, 47(3):615–632. https://doi.org/10.1175/JPO-D-16-0108.1.

Rutledge, S. A., Chandrasekar, V., Fuchs, B., George, J., Junyent, F., Kennedy, P., and Dolan, B. (2019). Deployment of the SEA-POL C-band Polarimetric Radar to SPURS-2. *Oceanography*, 32(2):50–57. https://doi.org/10.5670/oceanog.2019.212.

Samelson, R., O'Neill, L., Chelton, D., Skyllingstad, E., Barbour, P., and Durski, S. (2020). Surface stress and atmospheric boundary layer response to mesoscale sst structure in coupled simulations of the northern california current system. *Monthly Weather Review*, 148(1):259–287. https://doi.org/10.1175/MWR-D-19-0200.1.

Samelson, R., Skyllingstad, E., Chelton, D., Esbensen, S., O'Neill, L., and Thum, N. (2006). On the coupling of wind stress and sea surface temperature. *Journal of Climate*, 19(8):1557–1566. https://doi.org/10.1175/JCLI3682.1.

Santos-Garcia, A., Jacob, M. M., Jones, W. L., Asher, W. E., Hejazin, Y., Ebrahimi, H., and Rabolli, M. (2014). Investigation of rain effects on Aquarius sea surface salinity measurements. *Journal of Geophysical Research: Oceans*, 119(11):7605–7624. https://doi.org/10.1002/2014JC010137.

Schumacher, R. S. and Johnson, R. H. (2005). Organization and environmental properties of extreme-rain-producing mesoscale convective systems. *Monthly weather review*, 133(4):961–976. https://doi.org/10.1175/MWR2899.1.

Schwendeman, M. and Thomson, J. (2015). Observations of whitecap coverage and the relation to wind stress, wave slope, and turbulent dissipation. *Journal of Geophysical Research: Oceans*, 120(12):8346–8363. https://doi.org/10.1002/2015JC011196.

Sengupta, D., Bharath Raj, G., Ravichandran, M., Sree Lekha, J., and Papa, F. (2016). Near-surface salinity and stratification in the north bay of bengal from moored observations. *Geophysical Research Letters*, 43(9):4448–4456. https://doi.org/10.1002/2016GL068339.

Seo, H. (2017). Distinct influence of air–sea interactions mediated by mesoscale sea surface temperature and surface current in the arabian sea. *Journal of Climate*, 30(20):8061–8080. https://doi.org/10.1175/JCLI-D-16-0834.1.

Seo, H., Jochum, M., Murtugudde, R., and Miller, A. J. (2006). Effect of ocean mesoscale variability on the mean state of tropical atlantic climate. *Geophysical research letters*, 33(9). https://doi.org/10.1029/2005GL025651.

Seo, H., Jochum, M., Murtugudde, R., Miller, A. J., and Roads, J. O. (2007). Feedback of tropical instability-wave-induced atmospheric variability onto the ocean. *Journal of Climate*, 20(23):5842–5855. https://doi.org/10.1175/JCLI4330.1.

Shao, M., Ortiz-Suslow, D. G., Haus, B. K., Lund, B., Williams, N. J., Özgökmen, T. M., Laxague, N. J., Horstmann, J., and Klymak, J. M. (2019). The variability of winds

and fluxes observed near submesoscale fronts. *Journal of Geophysical Research: Oceans*, 124(11):7756–7780. https://doi.org/10.1029/2019JC015236.

Shinoda, T., Hendon, H. H., and Glick, J. (1998). Intraseasonal variability of surface fluxes and sea surface temperature in the tropical western pacific and indian oceans. *Journal of climate*, 11(7):1685–1702. https://doi.org/10.1175/1520-0442(1998)011¡1685:IVOSFA¿2.0.CO;2.

Small, R., deSzoeke, S. P., Xie, S., O'neill, L., Seo, H., Song, Q., Cornillon, P., Spall, M., and Minobe, S. (2008). Air–sea interaction over ocean fronts and eddies. *Dynamics of Atmospheres and Oceans*, 45(3-4):274–319. https://doi.org/10.1016/j.dynatmoce.2008.01.001.

Small, R. J., Bacmeister, J., Bailey, D., Baker, A., Bishop, S., Bryan, F., Caron, J., Dennis, J., Gent, P., Hsu, H.-m., et al. (2014). A new synoptic scale resolving global climate simulation using the community earth system model. *Journal of Advances in Modeling Earth Systems*, 6(4):1065–1094. https://doi.org/10.1002/2014MS000363.

Small, R. J., Bryan, F. O., Bishop, S. P., and Tomas, R. A. (2019). Air–sea turbulent heat fluxes in climate models and observational analyses: What drives their variability? *Journal of Climate*, 32(8):2397–2421. https://doi.org/10.1175/JCLI-D-18-0576.1.

Smit, P. B. and Janssen, T. T. (2019). Swell propagation through submesoscale turbulence. *Journal of Physical Oceanography*, 49(10):2615–2630. https://doi.org/10.1175/JPO-D-18-0250.1.

Smith, S. D. (1980). Wind stress and heat flux over the ocean in gale force winds. *Journal of Physical Oceanography*, 10(5):709–726. https://doi.org/10.1175/1520-0485(1980)010¡0709:WSAHFO¿2.0.CO;2.

Smyth, W., Zavialov, P., and Moum, J. (1997). Decay of turbulence in the upper ocean following sudden isolation from surface forcing. *Journal of physical oceanography*, 27(5):810–822. https://doi.org/10.1175/1520-0485(1997)027¡0810:DOTITU¿2.0.CO;2.

Soloviev, A. V., Matt, S., and Fujimura, A. (2015). Three-dimensional dynamics of freshwater lenses in the ocean's near-surface layer. *Oceanography*, 28(1):142–149. https://doi.org/10.5670/oceanog.2015.14.

Sprintall, J. (2019). Upper-ocean salinity stratification during SPURS-2. *Oceanography*, 32(2):40–41. https://doi.org/10.5670/oceanog.2019.210.

Stevens, B., Bony, S., Farrell, D., Ament, F., Blyth, A., Fairall, C., Karstensen, J., Quinn, P. K., Speich, S., Acquistapace, C., et al. (2021). EUREC^{4}A. *Earth System Science Data Discussions*, pages 1–78. https://doi.org/10.5194/essd-2021-18.

Stips, A., Burchard, H., Bolding, K., and Eifler, W. (2002). Modelling of convective turbulence with a two-equation k-epsilon turbulence closure scheme. *Ocean Dynamics*, 52(4):153–168. https://doi.org/10.1007/s10236-002-0019-2.

Strobach, E., Klein, P., Molod, A., Fahad, A. A., Trayanov, A., Menemenlis, D., and Torres, H. (2022). Local air-sea interactions at ocean mesoscale and submesoscale in a western boundary current. *Geophysical Research Letters*, page e2021GL097003. https://doi.org/10.1029/2021GL097003.

Stull, R. B. (1988). *An introduction to boundary layer meteorology*, volume 13. Springer Science & Business Media.

Su, Z., Wang, J., Klein, P., Thompson, A. F., and Menemenlis, D. (2018). Ocean submesoscales as a key component of the global heat budget. *Nature communications*, 9(1):1–8. https://doi.org/10.1038/s41467-018-02983-w.

Sullivan, P. P., McWilliams, J. C., Weil, J. C., Patton, E. G., and Fernando, H. J. (2020). Marine boundary layers above heterogeneous sst: Across-front winds. *Journal of the Atmospheric Sciences*, 77(12):4251–4275. https://doi.org/10.1175/JAS-D-20-0062.1.

Sullivan, P. P., McWilliams, J. C., Weil, J. C., Patton, E. G., and Fernando, H. J. (2021). Marine boundary layers above heterogeneous sst: Alongfront winds. *Journal of the Atmospheric Sciences*, 78(10):3297–3315. https://doi.org/10.1175/JAS-D-21-0072.1.

Sun, Q., Miao, C., Duan, Q., Ashouri, H., Sorooshian, S., and Hsu, K.-L. (2018). A review of global precipitation data sets: Data sources, estimation, and intercomparisons. *Reviews of Geophysics*, 56(1):79–107. https://doi.org/10.1002/2017RG000574.

Supply, A., Boutin, J., Vergely, J.-L., Martin, N., Hasson, A., Reverdin, G., Mallet, C., and Viltard, N. (2018). Precipitation estimates from SMOS sea-surface salinity. *Quarterly Journal of the Royal Meteorological Society*, 144:103–119. https://doi.org/10.1002/qj.3110.

Sutherland, G., Marié, L., Reverdin, G., Christensen, K. H., Broström, G., and Ward, B. (2016). Enhanced turbulence associated with the diurnal jet in the ocean surface boundary layer. *Journal of Physical Oceanography*, 46(10):3051–3067. https://doi.org/10.1175/JPO-D-15-0172.1.

Suzuki, N., Fox-Kemper, B., Hamlington, P. E., and Van Roekel, L. P. (2016). Surface waves affect frontogenesis. *Journal of Geophysical Research: Oceans*, 121(5):3597–3624. https://doi.org/10.1002/2015JC011563.

Sweet, W., Fett, R., Kerling, J., and La Violette, P. (1981). Air-sea interaction effects in the lower troposphere across the north wall of the gulf stream. *Monthly Weather Review*, 109(5):1042–1052. https://doi.org/10.1175/1520-0493(1981)109¡1042:ASIEIT¿2.0.CO;2.

Tan, J., Petersen, W. A., Kirstetter, P.-E., and Tian, Y. (2017). Performance of IMERG as a function of spatiotemporal scale. *Journal of hydrometeorology*, 18(2):307–319. https://doi.org/10.1175/JHM-D-16-0174.1.

Tang, C., Perrie, W., Jenkins, A., DeTracey, B., Hu, Y., Toulany, B., and Smith, P. (2007). Observation and modeling of surface currents on the Grand Banks: A study of the

wave effects on surface currents. *Journal of Geophysical Research: Oceans*, 112(C10). https://doi.org/10.1029/2006JC004028.

ten Doeschate, A., Sutherland, G., Bellenger, H., Landwehr, S., Esters, L., and Ward, B. (2019). Upper ocean response to rain observed from a vertical profiler. *Journal of Geophysical Research: Oceans*, 124(6):3664–3681. https://doi.org/10.1029/2018JC014060.

Terray, E. A., Donelan, M., Agrawal, Y., Drennan, W. M., Kahma, K., Williams, A. J., Hwang, P., and Kitaigorodskii, S. (1996). Estimates of kinetic energy dissipation under breaking waves. *Journal of Physical Oceanography*, 26(5):792–807. https://doi.org/10.1175/1520-0485(1996)026¡0792:EOKEDU¿2.0.CO;2.

Thompson, E., Fairall, C., Pezoa, S., and Bariteau, L. (2021). ATOMIC ship navigation, meteorology, seawater, fluxes: Near-surface meteorology, air-sea fluxes, surface ocean waves, and near surface ocean parameters (temperature, salinity, currents) and primary dataset of ship location and navigation estimated from in-situ and remote sensing instruments aboard NOAA Ship Ronald H. Brown in the North Atlantic Ocean, near Barbados: Atlantic Tradewind Ocean-Atmosphere Mesoscale Interaction Campaign 2020-01-09 to 2020-02-12 (NCEI Accession 0225427). NOAA National Centers for Environmental Information. Dataset. Accessed 17 June 2021.

Thompson, E. J., Asher, W. E., Jessup, A. T., and Drushka, K. (2019a). High-resolution rain maps from an x-band marine radar and their use in understanding ocean freshening. *Oceanography*, 32(2):58–65. https://doi.org/10.5670/oceanog.2019.213.

Thompson, E. J., Moum, J. N., Fairall, C. W., and Rutledge, S. A. (2019b). Wind limits on rain layers and diurnal warm layers. *Journal of Geophysical Research: Oceans*, 124(2):897–924. https://doi.org/10.1029/2018JC014130.

Thompson, E. J., Rutledge, S. A., Dolan, B., and Thurai, M. (2015). Drop size distributions and radar observations of convective and stratiform rain over the equatorial In-

dian and west Pacific Oceans. *Journal of the Atmospheric Sciences*, 72(11):4091–4125. https://doi.org/10.1175/JAS-D-14-0206.1.

Thomson, J. (2012). Wave breaking dissipation observed with "SWIFT" drifters. *Journal of Atmospheric and Oceanic Technology*, 29(12):1866–1882. https://doi.org/10.1175/JTECH-D-12-00018.1.

Thomson, J., D'Asaro, E., Cronin, M., Rogers, W., Harcourt, R., and Shcherbina, A. (2013). Waves and the equilibrium range at ocean weather station p. *Journal of Geophysical Research: Oceans*, 118(11):5951–5962. https://doi.org/10.1002/2013JC008837.

Thomson, J., Girton, J. B., Jha, R., and Trapani, A. (2018). Measurements of directional wave spectra and wind stress from a wave glider autonomous surface vehicle. *Journal of Atmospheric and Oceanic Technology*, 35(2):347–363. https://doi.org/10.1175/JTECH-D-17-0091.1.

Thomson, J., Horner-Devine, A. R., Zippel, S., Rusch, C., and Geyer, W. (2014). Wave breaking turbulence at the offshore front of the Columbia River plume. *Geophysical Research Letters*, 41(24):8987–8993. https://doi.org/10.1002/2014GL062274.

Thomson, J., Moulton, M., de Klerk, A., Talbert, J., Guerra, M., Kastner, S., Smith, M., Schwendeman, M., Zippel, S., and Nylund, S. (2019). A new version of the SWIFT platform for waves, currents, and turbulence in the ocean surface layer. In *2019 IEEE/OES Twelfth Current, Waves and Turbulence Measurement (CWTM)*, pages 1–7. IEEE. https://doi.org/10.1109/CWTM43797.2019.8955299.

Thomson, J., Thompson, E., Iyer, S., Drushka, K., and de Klerk, A. (2021). ATOMIC SWIFT drifters: Near-surface meteorology, air-sea fluxes, surface ocean waves, and near-surface ocean properties (turbulent dissipation rate, currents, temperature, salinity) estimated from in-situ and remote sensing instruments aboard six SWIFT drifters (Surface Wave Instrument Float with Tracking) launched and recovered for two different deploy-

ments from NOAA Ship Ronald H. Brown in the North Atlantic Ocean, near Barbados: Atlantic Tradewind Ocean-Atmosphere Mesoscale Interaction Campaign 2020-01-14 to 2020-02-11 (NCEI Accession 0225279). NOAA National Centers for Environmental Information. Dataset. Accessed 4 June 2021.

Thum, N., Esbensen, S. K., Chelton, D. B., and McPhaden, M. J. (2002). Air–sea heat exchange along the northern sea surface temperature front in the eastern tropical pacific. *Journal of climate*, 15(23):3361–3378. https://doi.org/10.1175/1520-0442(2002)015¡3361:ASHEAT¿2.0.CO;2.

Tokay, A. and Short, D. A. (1996). Evidence from tropical raindrop spectra of the origin of rain from stratiform versus convective clouds. *Journal of applied meteorology*, 35(3):355–371.

Tokay, A., Short, D. A., Williams, C. R., Ecklund, W. L., and Gage, K. S. (1999). Tropical rainfall associated with convective and stratiform clouds: Intercomparison of disdrometer and profiler measurements. *Journal of Applied Meteorology*, 38(3):302–320. https://doi.org/10.1175/1520-0450(1999)038¡0302:TRAWCA¿2.0.CO;2.

UK Met Office (2005). OSTIA L4 SST Analysis. Ver. 2.0. PO.DAAC, CA, USA. Dataset. Accessed 12 November 2021.

Umlauf, L. and Burchard, H. (2003). A generic length-scale equation for geophysical turbulence models. *Journal of Marine Research*, 61(2):235–265. https://doi.org/10.1357/002224003322005087.

van Aken, H. M. (2002). Surface currents in the Bay of Biscay as observed with drifters between 1995 and 1999. *Deep Sea Research Part I: Oceanographic Research Papers*, 49(6):1071–1086. https://doi.org/10.1016/S0967-0637(02)00017-1.

van der Westhuysen, A. J. (2012). Spectral modeling of wave dissi-

pation on negative current gradients. *Coastal Engineering*, 68:17–30. https://doi.org/10.1016/j.coastaleng.2012.05.001.

Vincent, C. L., Thomson, J., Graber, H. C., and Collins III, C. O. (2019). Impact of swell on the wind-sea and resulting modulation of stress. *Progress in Oceanography*, 178:102164. https://doi.org/10.1016/j.pocean.2019.102164.

Voermans, J., Smit, P., Janssen, T., and Babanin, A. (2020). Estimating wind speed and direction using wave spectra. *Journal of Geophysical Research: Oceans*, 125(2):e2019JC015717. https://doi.org/10.1029/2019JC015717.

Walesby, K., Vialard, J., Minnett, P. J., Callaghan, A. H., and Ward, B. (2015). Observations indicative of rain-induced double diffusion in the ocean surface boundary layer. *Geophysical Research Letters*, 42(10):3963–3972. https://doi.org/10.1002/2015GL063506.

Wallace, J. M., Mitchell, T., and Deser, C. (1989). The influence of sea-surface temperature on surface wind in the eastern equatorial Pacific: Seasonal and interannual variability. *Journal of Climate*, 2(12):1492–1499. https://doi.org/10.1175/1520-0442(1989)002¡1492:TIOSST¿2.0.CO;2.

Wang, P. and Sheng, J. (2016). A comparative study of wave-current interactions over the eastern Canadian shelf under severe weather conditions using a coupled wave-circulation model. *Journal of Geophysical Research: Oceans*, 121(7):5252–5281. https://doi.org/10.1002/2016JC011758.

Webster, P. J. and Lukas, R. (1992). Toga coare: The coupled ocean–atmosphere response experiment. *Bulletin of the American Meteorological Society*, 73(9):1377–1416. https://doi.org/10.1175/1520-0477(1992)073¡1377:TCTCOR¿2.0.CO;2.

Wenegrat, J. and Arthur, R. (2018). Response of the atmospheric boundary layer to submesoscale sea surface temperature fronts. *Geophysical Research Letters*, 45(24):13–505. https://doi.org/10.1029/2018GL081034.

Wick, G. A., Jackson, D. L., and Castro, S. L. (2022). Assessing the ability of satellites to resolve spatial sea surface temperature variability – the northwest tropical atlantic ATOMIC region. *Remote Sensing of Environment*.

Wijesekera, H., Paulson, C., and Huyer, A. (1999). The effect of rainfall on the surface layer during a westerly wind burst in the western equatorial Pacific. *Journal of Physical Oceanography*, 29(4):612–632. https://doi.org/10.1175/1520-0485(1999)029¡0612:TEOROT¿2.0.CO;2.

Wilheit, T. T., Chang, A. T., and Chiu, L. S. (1991). Retrieval of monthly rainfall indices from microwave radiometric measurements using probability distribution functions. *Journal of Atmospheric and Oceanic Technology*, 8(1):118–136. https://doi.org/10.1175/1520-0426(1991)008¡0118:ROMRIF¿2.0.CO;2.

Xu, W. and Rutledge, S. A. (2014). Convective characteristics of the Madden–Julian oscillation over the central Indian Ocean observed by shipborne radar during DYNAMO. *Journal of the Atmospheric Sciences*, 71(8):2859–2877. https://doi.org/10.1175/JAS-D-13-0372.1.

Yokoi, S., Katsumata, M., and Yoneyama, K. (2014). Variability in surface meteorology and air-sea fluxes due to cumulus convective systems observed during cindy/dynamo. *Journal of Geophysical Research: Atmospheres*, 119(5):2064–2078. https://doi.org/10.1002/2013JD020621.

Yu, L. (2011). A global relationship between the ocean water cycle and near-surface salinity. *Journal of Geophysical Research: Oceans*, 116(C10). https://doi.org/10.1029/2010JC006937.

Yu, L. (2019). Global air–sea fluxes of heat, fresh water, and momentum: energy budget closure and unanswered questions. *Annual review of marine science*, 11:227–248. https://doi.org/10.1146/annurev-marine-010816-060704.

Yu, L. and Weller, R. A. (2007). Objectively analyzed air–sea heat fluxes for the global ice-free oceans (1981–2005). *Bulletin of the American Meteorological Society*, 88(4):527–540. https://doi.org/10.1175/BAMS-88-4-527.

Zhang, G. J. and Mcphaden, M. J. (1995). The relationship between sea surface temperature and latent heat flux in the equatorial pacific. *Journal of climate*, 8(3):589–605. https://doi.org/10.1175/1520-0442(1995)008¡0589:TRBSST¿2.0.CO;2.

Zippel, S. and Thomson, J. (2017). Surface wave breaking over sheared currents: Observations from the Mouth of the Columbia River. *Journal of Geophysical Research: Oceans*, 122(4):3311–3328. https://doi.org/10.1002/2016JC012498.

Zippel, S. F., Farrar, J. T., Zappa, C. J., Miller, U., Laurent, L. S., Ijichi, T., Weller, R. A., McRaven, L., Nylund, S., and Le Bel, D. (2021). Moored turbulence measurements using pulse-coherent doppler sonar. *Journal of Atmospheric and Oceanic Technology*. https://doi.org/10.1175/JTECH-D-21-0005.1.

Zuidema, P., Li, Z., Hill, R. J., Bariteau, L., Rilling, B., Fairall, C., Brewer, W. A., Albrecht, B., and Hare, J. (2012). On trade wind cumulus cold pools. *Journal of the Atmospheric Sciences*, 69(1):258–280. https://doi.org/10.1175/JAS-D-11-0143.1.